CHAPTER 9

Modeling of Electrostatically Gated Vertical Quantum Dots

J. Adamowski, S. Bednarek, B. Szafran

Faculty of Physics and Applied Computer Science, AGH University of Science and Technology, Kraków, Poland

CONTENTS

1. INTRODUCTION

Quantum dots (QDs) are solid-state nanostructures with sizes not exceeding 1 μm that can bind excess electrons in localized states with discrete energy levels [1]. The QD with the confined electrons can be treated as an artificial atom [2, 3]. Recently, the two types of QDs are the most frequently studied: these are the self-assembled QDs [1, 4, 5] and the electrostatically gated QDs [6, 7]. The self-assembled QDs [4, 5] are fabricated during the growth of semiconductor material strained by a lattice mismatch with a substrate. In this process, the strain between the deposited material and the substrate leads to the formation of islands of the self-assembled QDs. The potential confining the charge carriers in the self-assembled QDs results from the strain and the discontinuities of the conduction and valence band edge energies (i.e., band offsets).

The electrostatically gated QDs are fabricated from the semiconductor heterostructure, which consists of either quantum-well and quantum-barrier layers or a heterojunction with an inversion layer. In both the cases, the band offsets between conduction bands of the adjacent layers create the strong confinement of electrons in the vertical direction (i.e., the direction perpendicular to the interfaces between the layers). The vertical confinement leads to a creation of a quasi-two-dimensional electron system, which is further confined laterally. Moreover, the nanostructure contains electrodes to which external voltages are applied. The electrostatic field, created by the external voltages, entails the confinement of the electrons in the lateral directions (i.e., parallel to the planes of the layers). Depending on the location of the electrodes, we deal with the lateral or vertical electrostatic QDs. In the lateral QDs, all the electrodes are attached to the upper layer and the electrons are confined in the inversion layer or quantum-well layer located below the electrodes. In the vertical QDs, the electrodes are located vertically above and below the QD region (i.e., the tunneling current flows in the vertical direction). The vertical QDs are usually fabricated by etching a pillar from a planar heterostructure, which consists of the layers made of different semiconductor materials. In the electrostatically gated vertical QDs [6, 7], the total potential confining the electrons stems from both the band offsets and external voltages applied to the attached electrodes. The confinement potential is effectively tuned by the gate voltage. The gate electrode can be either the upper electrode in the form of a cap in the two-electrode nanodevice [6] or the ring-shaped electrode placed at the side of the pillar in the three-electrode nanodevice [7]. The QDs with the electrodes attached are also called *electrostatically defined*, or, simply, *electrostatic* QDs [8]. Another name used for these QDs is *gate controlled*, or *gated* QDs, because the gate electrode plays a crucial role in determining their electronic properties.

The electrostatically gated QDs are attracting much interest in both physics [9–13] and quantum engineering [14–18]. In the basic physical research, the QD is a unique laboratory for studying the few-electron systems. In the electrostatically gated QDs, the properties of the confined electrons are determined by the confinement potential that can be, to a large extent, modified by changing the external voltages. This leads to an opportunity of studying the few-electron systems with the tailored properties. A broad class of new interesting phenomena occurs when applying the external magnetic field to the QD-confined electron system [2, 19–26]. The gated QD is a very important nanoelectronic device because it is a prototype of a single-electron transistor [14–18, 27–30]. Possible applications of the single-electron transistors are expected to yield an extremely high speed of nanoelectronic devices at low power consumption. Another exciting field of future applications of electrostatic QDs is quantum computation [31–45]. The QDs can be used to represent quantum bits (qubits)

[31, 32, 36, 39, 45] and to perform a readout of qubits as well as and logic operations on the qubits, the so-called *logic gates* [31–33, 35, 38, 44].

The important role of the electrostatic QDs in both basic and applied physics resulted in an enormous increase in the number of papers devoted to the nanotechnology of QDs [16, 46–49] and the experimental [6, 7, 23–26, 50–59] and theoretical [2,60–88] studies of the electronic properties of QDs. These investigations have led to considerable progress in understanding the electronic properties of QDs [83–88]. For example, we know [88] how to modify the parameters of the nanostructure to obtain the QD-based nanodevices with the required characteristics.

In the experimental investigations of the electrostatic QDs, new spectroscopic techniques were invented. They include the single-electron capacitance spectroscopy [6] and the single-electron transport spectroscopy [7]. Both these techniques are based on the single-electron tunneling [89, 90] via the nanostructure and allow us to measure the discrete energy levels of the confined electrons with high precision. The application of these spectroscopic techniques led to several spectacular discoveries. In 1993, Ray Ashoori's MIT research group [6] observed the single-electron charging of QDs and the magnetic-field evolution of the electron energy levels. In 1996, the research teams of Seigo Tarucha from Nippon Telegraph and Telephone (Japan) and Leo Kouwenhoven from the Delft Technical University (the Netherlands), using the single-electron transport spectroscopy, discovered the shell filling in artificial atoms formed in vertical gated QDs [7]. Next, the same teams [23] succeeded in completing a stability diagram with Coulomb diamonds and found the phase transitions in few-electron artificial atoms in an external magnetic field. In 1997 the MIT group [91], using the capacitance spectroscopy, discovered a bunching of energy levels of the electrons confined in QDs by measuring the single-electron tunneling in the magnetic field. Other interesting results include a Kondo effect for QDs [92–96], a cotunneling of electrons through the QD [97], and a formation of a maximum-density droplet (MDD) and Wigner molecules [24] in QDs at high magnetic fields. The recent experimental studies of the gated QDs are focused on the experimental realization of qubits and quantum logic operations [58, 59].

These experimental discoveries require a proper theoretical interpretation. Several theoretical papers are devoted to the electrostatically gated QDs [13,83–88]. To describe the quantum states of electrons confined in the QD with the electrodes attached, we have to solve the Poisson-Schrödinger problem by a self-consistent method [84, 86]. Using this approach to the three-electrode QDs [7, 23], we succeeded in obtaining a quantitative description [84, 86, 98] of the shell filling [7], stability diagram [23], phase transitions in the magnetic field [24], and transport windows [23]. The application of the same self-consistent procedure to the two-electrode QDs [6] led to the quantitative description [88] of the single-electron capacitance experiments in the magnetic field. Moreover, it was shown [88] how to change the nanodevice parameters to obtain the designed shape of the potential confining the electrons. These studies [86, 88] resulted in a computer modeling of the electronic properties of the electrostatically gated QDs.

In this chapter, we discuss the fundamental physical properties of the electrostatically gated vertical QDs with two [6] and three [7] electrodes connected to the nanodevice. We present the theoretical methods [84, 86, 88, 98], elaborated in our research group, that describe basic electronic characteristics of these QDs. These methods also allow us to design the nanodevices with the required electronic properties and to predict new effects.

This chapter is organized as follows: Section 2 describes the structure of the two- and three-electrode QDs. Section 3 introduces the conditions of the single-electron tunneling and presents the fundamentals of the single-electron capacitance and single-electron transport spectroscopy. The self-consistent method to solution of the Poisson-Schrödinger problem is presented in Section 4, and the application of this method to a quantitative interpretation of the single-electron transport spectroscopy data is given in Section 5. Section 6 is devoted to a modeling of QD confinement potentials. Moreover, in Section 6, we demonstrate how to change the parameters of the nanodevice to obtain the required electronic characteristics of the QDs. In Section 7, we discuss the effect of the external magnetic field on the electronic properties of the QDs and the single-electron transport. The electron–electron

correlation effects are discussed in Section 8. Special attention is paid to a role of correlation in the quantitative description of the single-electron tunneling through the QDs. A theory of Wigner molecules is outlined in Section 9. A study of coupled QDs (artificial molecules) is presented in Section 10. A discussion of reliability of the theoretical methods, presented in previous sections, is provided in Section 11. In Section 12, we outline the applications of the electrostatically gated QDs to a construction of single-electron transistors and a quantum computing. Section 13, which contains conclusions and a summary, is followed by a glossary of the most important notions used in the chapter.

## 2. STRUCTURE OF NANODEVICES

We consider the two types of electrostatically gated vertical QDs, namely, the two-terminal (two-electrode) QDs studied by Ashoori et al. [6] and three-terminal (three-electrode) QDs studied by Tarucha et al. [7] and Kouwenhoven et al. [23]. The study of these two types of vertical gated QDs leads to very interesting physics and promising applications. The scanning electron micrographs of the three-terminal QDs with various shapes [12] are shown in Fig. 1. These QDs were fabricated [12] as pillars with circular, rectangular, and triangular bases. The lateral sizes of the pillars are ∼500 nm. In Fig. 1, we see the top electrode (drain) and the black metal ring (gate).

2.1. Two-Terminal Quantum Dots

The schematic of the two-terminal QD nanodevice of Ashoori et al. [6] is shown in Fig. 2. The nanodevice, studied in Ref. [6], has a planar structure and consists of the GaAs and AlGaAs layers. The substrate layer made of the heavily donor doped GaAs with 300 nm thickness forms the bottom electrode. On the substrate, the following layer sequence is grown: the 60-nm GaAs spacer, the 12.5-nm AlGaAs tunel barrier, the 17.5-nm GaAs quantum well, the 50-nm AlGaAs blocking barrier, and the 30-nm GaAs cylindrical cap. The blocking barrier consists of the two sublayers: the 15-nm lower sublayer is undoped and the 35-nm upper sublayer is doped with donors. In Ref. [55], this sublayer was homogeneously doped in its entire volume, while in Ref. [6] a δ dopping was used. The nanostructure was etched by plasma to produce a pillar of 30-nm height. Finally, the entire nanostructure was covered by the metal layer that formed the top gate electrode. The voltage applied between the gate and bottom electrode creates the inhomogeneous electrostatic field, which, in the region of the nanodevice located below the GaAs cap, generates the potential confining the electrons in the GaAs quantum well in the lateral directions (i.e., parallel to the interfaces). The vertical confinement, i.e., perpendicular to the interfaces, results from the conduction-band offsets at the GaAs/AlGaAs interfaces. The physical region of the QD is located within the GaAs quantum-well layer below the cap.

2.2. Three-Terminal Quantum Dots

The three-terminal QD studied by Tarucha et al. [7] and Kouwenhoven et al. [23] has the form of a pillar and is schematically depicted in Fig. 3. The scanning electron micrographs of the QD pillars with various shapes are shown in Fig. 1. Each pillar [7, 23] is fabricated
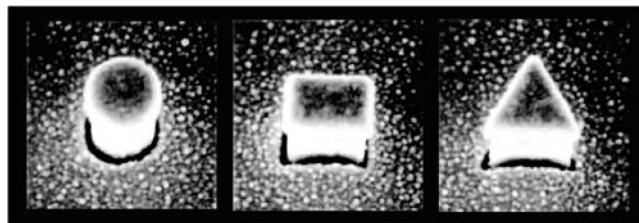
Figure 1. Scanning electron micrographs of QD pillars with various shapes. The pillars have widths ∼0.5 μm. Reprinted with permission from [12], L. P. Kouwenhoven et al., *Rep. Prog. Phys.* 64, 701 (2001). © 2001, IOP Publishing Ltd.
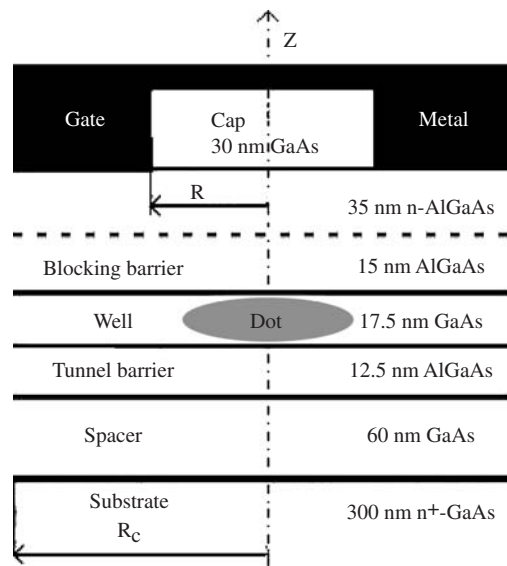
Figure 2. Schematic of the two-terminal nanodevice [6]. R is the radius of the GaAs cap, covered by the metal gate; R_c is the radius of the cylindrical surface, on which the boundary conditions are put for the Poisson equation [88]. From Ref. [88].

from the multilayer GaAs/AlGaAs/InGaAs heterostructure. The physical region of the QD is located within the 12-nm $In_{0.05}Ga_{0.95}As$ quantum-well layer. The two $Al_{0.22}Ga_{0.78}As$ barrier layers adhere to the quantum-well layer: the upper one is 9 nm thick and the lower one is 7.5 nm thick. This part of the pillar is surrounded by the ring-shaped Schottky gate. The sequences of the layers lying above the upper AlGaAs barrier and below the lower AlGaAs barrier are the same (Fig. 4). Each of them consists of the 3-nm GaAs spacer layer and the stepwise doped n-GaAs layers. There are four n-GaAs layers: the 70-nm GaAs layer with
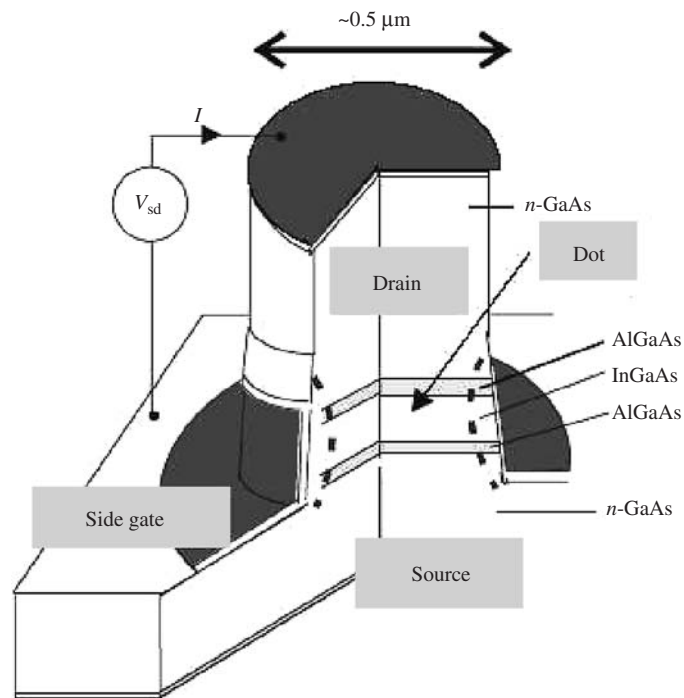
Figure 3. Schematic of the vertical three-terminal nanodevice. The QD is located in the InGaAs layer between the two AlGaAs tunnel barriers. Reprinted with permission from [12], L. P. Kouwenhoven et al., *Rep. Prog. Phys.* 64, 701 (2001). © 2001, IOP Publishing Ltd.

Figure 4. Schematic of the model [86] of the three-terminal nanodevice [7]. Given are the donor concentrations and layer thicknesses. Dotted line indicates the cross section of surface Σ with inner (outer) radius R (R_b) on which we put the boundary conditions for the Poisson equation. From [86].

donor concentration $N_D = 1 \times 10^{17}$ cm^{-3}, which adheres to the spacer, the 150-nm GaAs layer with $N_D = 1.4 \times 10^{17}$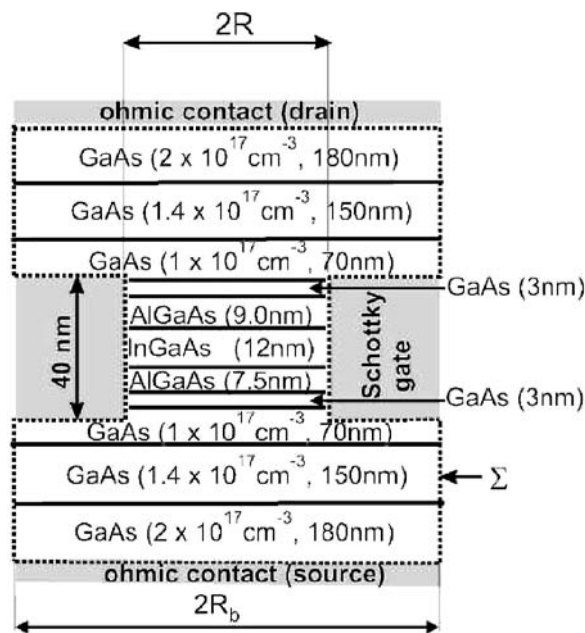 cm^{-3}, and the 180-nm GaAs layer with $N_D = 2.0 \times 10^{17}$ cm^{-3}, which is terminated by the heavily doped GaAs layer, with $N_D = 2.0 \times 10^{18}$ cm^{-3}. The terminating GaAs layers form the Ohmic contacts, i.e., the top (drain) and bottom (source) electrodes. The nanostructure was etched to form a pillar to a plane just below the lower (thinner) AlGaAs barrier.

Next we focus on the pillar with the cylindrical shape. We identify the z-axis with the cylinder axis, whereby $z = 0$ corresponds to the center of the InGaAs layer. Then, the nanodevice is asymmetric with respect to the $z = 0$ plane. The upper part of the nanodevice is the etched pillar and the lower part consists of the nonetched GaAs layers. However, the stability diagram measured in Ref. [23] shows an almost perfect symmetry against the drain-source voltage polarity. Therefore, the drain and source can be interchanged by using the voltage of the opposite polarity. This symmetry allowed us to apply in the calculations [84, 86] the model nanostructure (see Fig. 4), which was symmetric with respect to the inversion in the $z = 0$ plane. Nevertheless, the different thicknesses of the AlGaAs barrier layers were taken into account in calculations [84, 86]. The application of the nearly symmetric model nanostructure [84, 86] considerably simplifies the calculations.

3. SINGLE-ELECTRON TUNNELING SPECTROSCOPY

The energy levels of electrons confined in the QDs can be measured by either the infrared magnetoabsorption spectroscopy [99, 100] or the spectroscopy based on the single-electron tunneling [90]. In the magnetoabsorption, the transitions between discrete energy levels are observed in the infrared radiation [99, 100]. The single-electron tunneling spectroscopy exploits the sequential tunneling of electrons via the localized QD states. In the sequential tunneling process, the electrons tunnel one by one from the one lead attached to the QD and next, depending on the voltage drop in the nanodevice and the presence of either the blocking or tunnel barrier, can either jump back to the same lead or tunnel further to the another lead. In the first case, we can detect oscillations of the charge confined in the QD, which leads to the single-electron capacitance spectroscopy, and in the second case, we can measure a current through the QD, which leads to the single-electron transport spectroscopy.

Conditions for the electron energy measurements by either the method are similar and can be formulated with the help of electrochemical potentials [101].

3.1. Conditions of Single-Electron Tunneling

The conditions of the resonant single-electron tunneling via the QD are determined by the energy balance between electrochemical potentials of the electrons in the top and bottom electrodes and in the QD [101]. The electrochemical potential of the electrons in the electrode denoted by symbol α is defined as

$$\mu_\alpha = \mu_\alpha^0 - eV_\alpha, \tag{1}$$

where μ_α^0 is the chemical potential of electrons in electrode α, V_α is the voltage applied to electrode α, and e is the elementary charge ($e > 0$), that is, the electron charge $q_e = -e$. For the metal electrode at zero temperature and zero voltage, the chemical potential is identified with the Fermi energy, that is,

$$\mu_\alpha = F_\alpha . \tag{2}$$

If the heavily n-type doped semiconductor layer is adjacent to the metal surface, the Fermi energy equalizes with a donor energy level (E_D). For N electrons confined in the QD, the chemical potential is defined as the energy needed to increase the number of electrons by one, that is,

$$\mu_{QD}^0 \equiv \mu_{N+1} = E_{N+1} - E_N, \tag{3}$$

where E_N is the ground-state energy of the N-electron system confined in the QD.

The tunneling of the single electron from electrode α to the QD is energetically allowed if

$$\mu_\alpha \geq \mu_{N+1}. \tag{4}$$

If the sign of inequality (4) is opposite, the electron can jump back from the QD to electrode α. Inequality (4) determines the condition for the single-electron charging of the QD. In the capacitance spectroscopy measurements [6], a superposition of a dc voltage and a small-amplitude ac voltage is applied between the two electrodes (called *top* and *substrate contacts*, or *gate* and *back contacts*). For the dc gate voltages, for which chemical potential μ_{N+1} of the QD, becomes equal to the Fermi energy of the substrate, the small-amplitude ac voltage causes the tunneling of the $(N + 1)$th electron from the substrate through the tunnel barrier into the QD and back. Because of the presence of the AlGaAs blocking barrier, the electrons tunnel between the substrate (back) electrode and the QD, only, and do not reach the top (gate) electrode. In this process, the capacitance of the QD nanodevice rapidly increases. When measuring the differential capacitance as a function of the dc gate voltage, Ashoori et al. [6] observed the sharp peaks that correspond to the tunneling of the subsequent electrons through the barrier (see Fig. 5). The peaks of the differential capacitance are detected by a high-resolution capacitance bridge [6].

Let us consider the transport spectroscopy. In this case, condition (4) for the single-electron charging of the QD can be extended to the tunneling of the single electron from the one electrode (source) through the QD to the second electrode (drain) as follows:

$$\mu_s \geq \mu_{N+1} \geq \mu_d, \tag{5}$$

where μ_s (μ_d) is the electrochemical potential of the source (drain). The electrochemical potentials of the source and drain are determined by the voltages applied to the source (V_s) and drain (V_d) [see Eq. (1)]. In the three-electrode nanodevice [7], the voltage applied to the third (gate) electrode affects the confinement potential, which in turn changes the energy of the electrons confined in the QD (i.e., chemical potential μ_{N+1}). Therefore, the gate voltage has an indirect, but essential, influence on the electron tunneling. If the Fermi energies of the source and drain are equal (i.e., $F_s = F_d = F$), then, according to condition (5), the single-electron tunneling is determined by the drain-source voltage (bias voltage) $V_{ds} = V_d - V_s$.
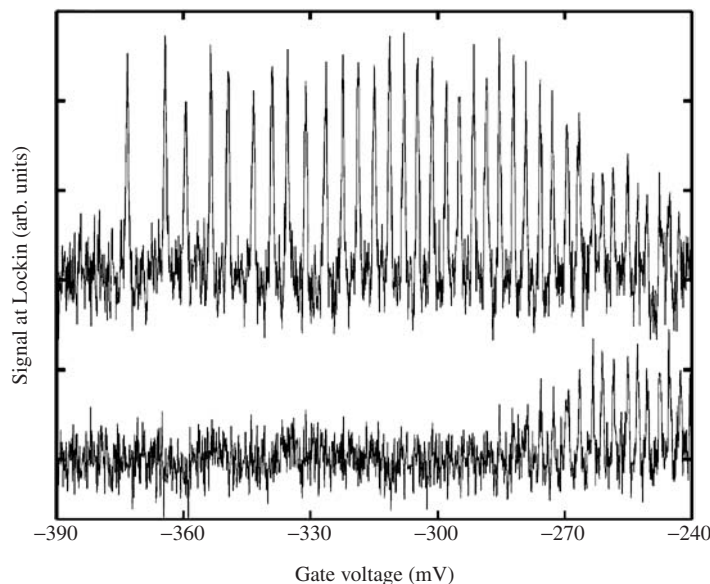
Figure 5. Capacitance of the sample containing the two-electrode QD as a function of the gate voltage. The first peak on the left represents the first electron entering the QD. Reprinted with permission from [22], R. C. Ashoori, *Nature* 379, 413 (1996). © 1996, Nature.

By applying the reverse bias (i.e., V_{ds} with opposite sign), we can reverse the inequality signs in condition (5) and obtain the tunneling of the electron from the drain to the source. This means that the notions of the source and drain are the matter of convention. One can equally well speak about the first and second electrodes, the left and right electrodes, the top and bottom electrodes. Because of the weak inequalities in condition (5), the electron can tunnel through the nanodevice even at nearly zero bias.

If condition (5) is satisfied, number N of electrons confined in the QD changes as follows:

$$N \to N + 1 \to N \to \cdots \tag{6}$$

and the single electron tunnels from the first electrode through the QD to the second electrode, known as opening up the transport window. If condition (5) is not fulfilled, the number of electrons confined in the QD remains constant, and we are dealing with the quantum Coulomb blockade [102] that results from the discreteness of energy levels of the electrons confined in the QD. In general, one observes [7] unequally spaced peaks of the tunneling current as a function of gate voltage for the source-drain voltage nearly equal to zero (see Fig. 6). If the number of electrons confined in the QD becomes large (i.e., larger than ∼100), the differences between the electron energy levels are very small and become equally spaced. Therefore, the peaks of the current are almost equally spaced on the gate voltage scale by $\Delta V_g = e/C$, where C is the capacitance of the QD nanodevice. The equal spacings between the tunneling-current peaks at $V_{ds} \simeq 0$ can be described with the help of the classical model of the Coulomb blockade [89].

3.2. Single-Electron Capacitance Spectroscopy

The single-electron capacitance spectroscopy technique was applied by Ashoori et al. [6] to the two-terminal vertical QDs. The experimental results obtained in Ref. [6] are shown in Fig. 5 in which each sharp peak corresponds to the tunneling of the subsequent electrons from the gate to the QD.

The same technique, applied in the external magnetic field, is allowed to trace the magnetic field evolution of energy levels for N electrons confined in the QD [6]. Figure 7 shows the results for $N = 1, \ldots, 10$. The bumps, visible on the plots for $N \geq 2$, correspond to the magnetic-field-induced transformations of the N-electron ground state (e.g., for $N = 2$, the
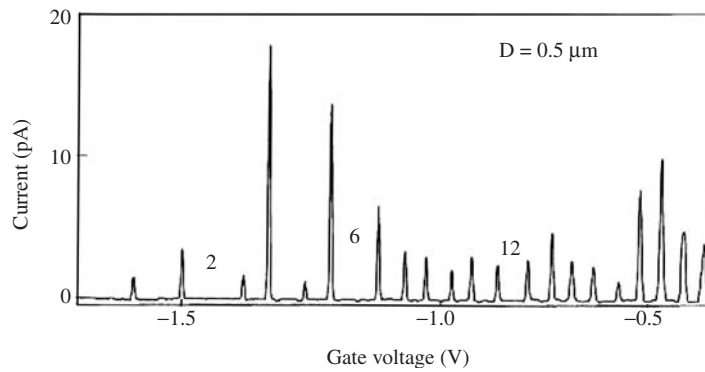
Figure 6. Source-drain current versus gate voltage at drain-source voltage $V_{ds} = 150\ \mu$V for the three-electrode QD with diameter $D = 0.5\ \mu$m. Reprinted with permission from [7], S. Tarucha et al., *Phys. Rev. Lett.* **77**, 3613 (1996). © 1996, The American Physical Society.

singlet-triplet transition is observed at $B \simeq 2$ T). The electron addition spectra for $N < 200$ exhibit a bunching [91] (i.e., the plots are grouped into the bunches comprising from two to six lines).

3.3. Single-Electron Transport Spectroscopy

The most spectacular results, obtained by the single-electron spectroscopy for the three-terminal QDs [7, 23, 24], are shown in Figs. 6, 8, 9, and 10. Figure 6 shows the source-drain current as a function of gate voltage measured [7] at small bias ($V_{ds} = 150\ \mu$V) and at
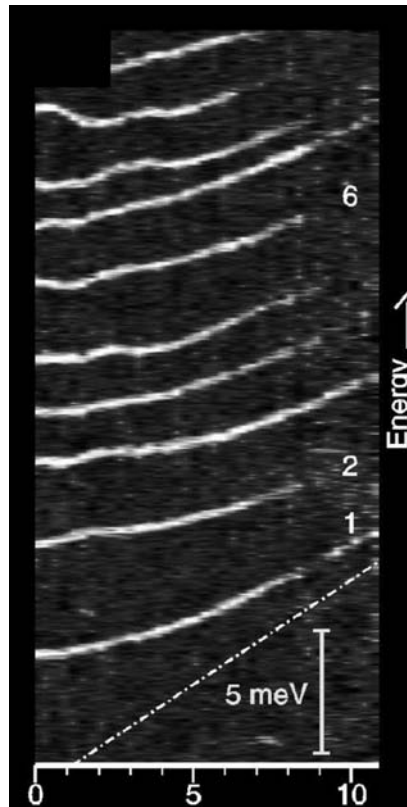
Figure 7. Single-electron capacitance spectroscopy data for the first 10 electrons in the QD as a function of magnetic field. The vertical bar represents an energy of 5 meV. The dashed line shows the energy of the lowest Landau level. Reprinted with permission from [22], R. C. Ashoori, *Nature* 379, 413 (1996). © 1996, Nature.

very low temperature ($T \simeq 50$ mK). Each current peak results from many sequential single-electron tunneling processes. The time interval between the tunneling events was estimated to vary from 1 ns to 100 ns [57]. For $V_g < -1.6$ V, the QD is empty. The first peak at $V_g \simeq -1.6$ V corresponds to the tunneling of the first electron via the QD. With the increasing gate voltage, the subsequent electrons are added to the QD. The relative distances between the peaks in Fig. 6 correspond to the filling of the subsequent shells of the artificial atom. The positions of these peaks can be qualitatively explained in the framework of the simple model of the QD with the 2D, cylindrically symmetric, confinement potential. According to this model, the larger separations observed between the second and third peaks, the sixth and seventh peaks, and the twelfth and thirteenth peaks correspond to the complete filling of the first, second, and third electronic shells of the the artificial atom, respectively. The slightly larger separations, observed [7] between the 4th and 5th peaks and the 9th and 10th peaks, result from the filling of the subsequent subshells according to Hund's rule for the cylindrically symmetric confinement potential. The magnetic-field evolution of the single-electron tunneling peaks was observed by Kouwenhoven et al. [23] (see Fig. 9). The kinks on the plots (marked by the full symbols in Fig. 9) result from the magnetic-field-induced ground-state transformations. The corresponding spin configurations are shown by the arrows in the squares (see Fig. 9).

In Fig. 6, the intervals of the gate voltage corresponding to zero source-drain current result from the Coulomb blockade. Then, the electrons confined in the QD prevent the flow of subsequent electrons. With the increasing source-drain voltage, the Coulomb blockade intervals shrink to zero. The corresponding experimental results [23] are shown in Fig. 8, which shows the so-called stability diagram, that is, the positions of the differential conductance peaks on the $V_{ds} - V_g$ plane. The white, diamond-shaped regions correspond to zero differential conductance (i.e., the Coulomb blockade). These Coulomb blockade regions are
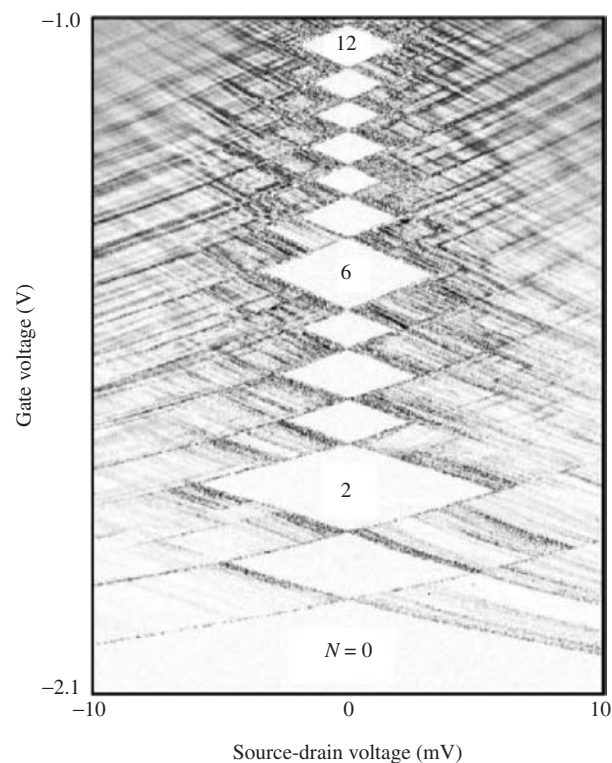
Figure 8. Differential conductance $\partial I/\partial V_{ds}$ plotted in gray scale on the $V_g - V_{ds}$ plane at $B = 0$. In the white diamond-shaped regions, $\partial I/\partial V_{ds} \simeq 0$ as a result of the Coulomb blockade. Number N of QD-confined electrons is fixed in each of the diamond regions. Reprinted with permission from [23], L. P. Kouwenhoven et al., *Science* 278, 1788 (1997). © 1997, AAAS.
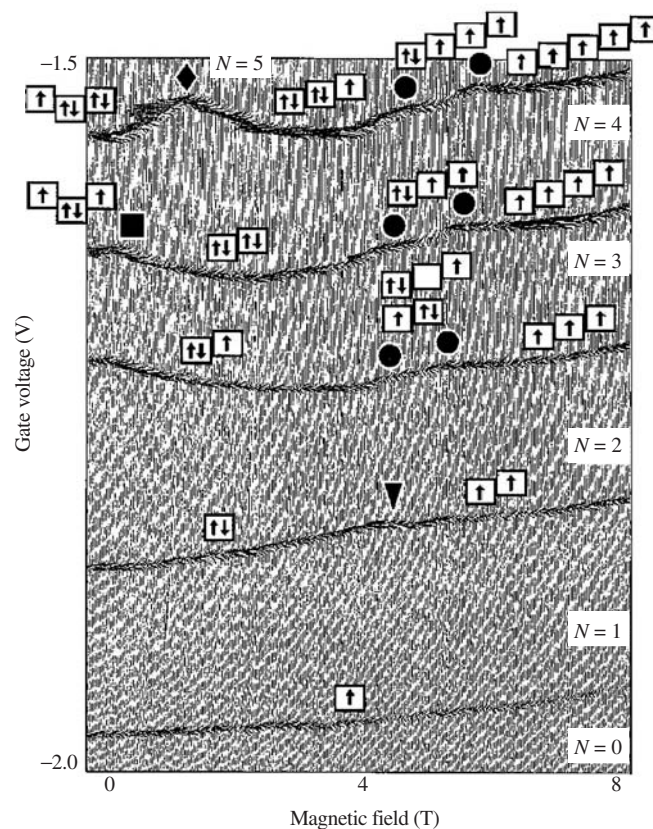
Figure 9. Source-drain current peaks as functions of gate voltage and magnetic field measured with small bias $V_{ds} = 0.1$ mV such that only ground states contributed to the current. The ground-state transitions are indicated by different symbols. Number N of QD-confined electrons is fixed between each of the two plots because of the Coulomb blockade. Reprinted with permission from [23], L. P. Kouwenhoven et al., *Science* 278, 1788 (1997). © 1997, AAAS.

also called the *Coulomb diamonds*. Number N of the QD confined electrons is fixed in each of the diamond regions [23].

The single-electron tunneling peaks at high magnetic fields were measured by Oosterkamp et al. [24] (see Fig. 10). If the magnetic field is sufficiently strong, the N-electron system becomes fully spin polarized and the electrons occupy the orbitals with the subsequent angular momenta. This state is called the *maximum-density droplet* (MDD) [103]. If the magnetic field increases further, the MDD decays and a Wigner molecule [104] is formed with an island-like electron density distribution. Both the formation and decay of the MDD are visible in Fig. 10 as abrupt steps marked by full and open circles. In the Wigner-molecule regime, the additional steps were observed (the dotted oval in Fig. 10). The authors [24] argued that at all these steps the electron charge distribution changes abruptly.

4. POISSON-SCHRÖDINGER PROBLEM

A theoretical description of the spectacular experimental discoveries of Ashoori et al. [6], Tarucha et al. [7], and Kouwenhowen et al. [23] was the subject of many theoretical papers [72–75, 84–88, 98]. In some of these papers, for example, in Refs. [72–75], the simple 2D model with the parabolic confinement potential was applied. Such an approach neglects a dependence of the confinement potential on the gate voltage and the QD-confined electrons and simplifies the three-dimensional (3D) problem to the 2D one. The 2D models suffer from the neglect of the third (z) dimension in which the transport of electrons occurs.

A reliable theory of the electrostatic QDs should derive the confinement potential from the first principles of electrostatics. This theory should allow us to take into account the dependence of the problem on all the relevant parameters of the nanodevice. Therefore, the
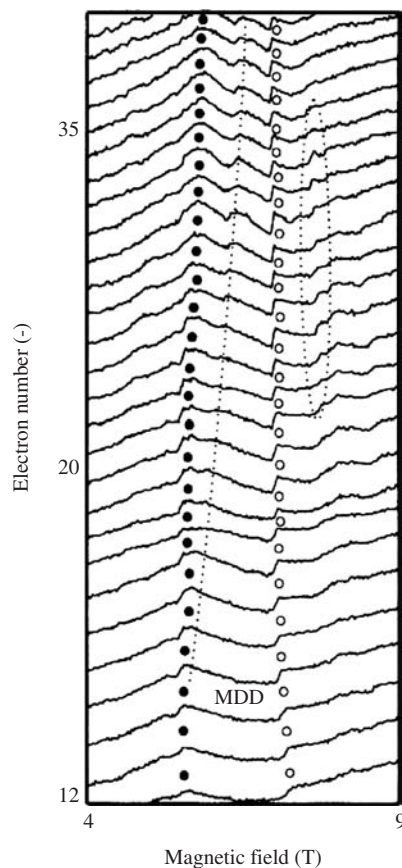
Figure 10. Gate voltage, corresponding to the current peaks of the single-electron tunneling at $V_{ds} = 100\ \mu$V versus magnetic field for different numbers of electrons given on the ordinate axis. The solid (open) dots mark the beginning (end) of the MDD stability region. The dotted oval corresponds to the abrupt changes of the charge distribution. Reprinted with permission from [24], T. H. Oosterkamp et al., *Phys. Rev. Lett.* 82, 2931 (1999). © 1999, The American Physical Society.

theory of the electronic properties of the QDs should be based on a self-consistent approach to a solution of the underlying Poisson-Schrödinger problem [83–88]. In this section, we present such a theory elaborated in our group [84, 86, 88].

4.1. Electrostatic Fields in QDs

Excess electrons are confined in the electrostatically gated QDs by external fields that stem from different sources. The vertical QD contains several layers made of different semiconducting materials. The discontinuities of the conduction bands, which occur at the interfaces, lead to potential jumps (band offsets) that form a potential-barrier/potential-well profile in the z direction. As a result, we obtain either a single or multiple quantum-well structure. Both in the two- and three-terminal vertical QDs [6, 7] the confinement in the vertical direction results from the band offsets. In the three-terminal QDs [7], the lateral confinement (i.e., the confinement in the x, y directions), results from the electrostatic field, which is created by the voltage applied between the gate and the source (drain) and by the ionized donors in n-type semiconductor layers. In the two-terminal QD [6], the nonuniform electrostatic field is created below the GaAs cap as a result of moving away the central part of the gate because of presence of the cap (see Fig. 2). This nonuniform field is a source of the lateral confinement. Therefore, in the electrostatically gated vertical QDs, the external fields acting on the electrons confined in the QD are of the band offset as well as electrostatic origin.

The additional complication of the problem occurs because the electrostatic fields are modified by the presence of the electrons in the QD. The electrostatic field, created by the

electrons confined in the QD, induces the additional charge on the leads and causes the additional ionization of the donors in the n-type doped semiconductor layers. These effects lead to a change of the total electrostatic field. The electrostatic field in the nanodevice modifies, in turn, the quantum states of the electrons confined in the QD. Therefore, the theory of the electronic properties of the electrostatic QDs requires self-consistency. Knowing the charge density of the ionized donors and external voltages applied to the leads (i.e., the boundary conditions), we can solve the Poisson equation and calculate the electrostatic potential from external sources. The band-offset contribution does not depend on the charges in the system and can be added to the electrostatic potential. The electrostatic potential depends on the charge density distribution in the QD, which is determined by the electron wave functions. These wave functions can be found by solving the Schrödinger equation. Therefore, we deal with the self-consistent Poisson-Schrödinger problem.

Let us consider the main steps of the self-consistent procedure. They are illustrated in block diagram (Fig. 11). The iterative procedure starts with the Coulomb potential of N electrons treated, in the first step, as a single point charge. The Poisson equation is solved by the finite-difference relaxation method for the electrostatic potential φ_1 in the nanodevice, which enables us to determine the distribution of the ionized donors in the n-GaAs layers. The calculated electrostatic potential is used as the external potential in the Schrödinger equation, which is solved by the unrestricted Hartree-Fock (UHF) method [86]. As an output of the Hartree-Fock approach, we obtain the one-electron wave functions and the ground-state energy E_N of the N-electron system confined in the QD. The knowledge of the one-electron wave functions enables us to calculate the density of the confined charge and the potential, φ_2, generated by this charge. Potential φ_2 is reintroduced via the outer iteration loop (labeled by i) into the boundary conditions for the Poisson equation on surface Σ. The iterations run until the convergence of the ground-state energy E_N is reached. The iteration procedure, depicted in Fig. 11, also contains the inner loop (labeled by n), in which the charge density of the ionized donors is calculated. The inner loop is terminated if the self-consistency of the confinement potential energy is reached. We note that the numerical steps
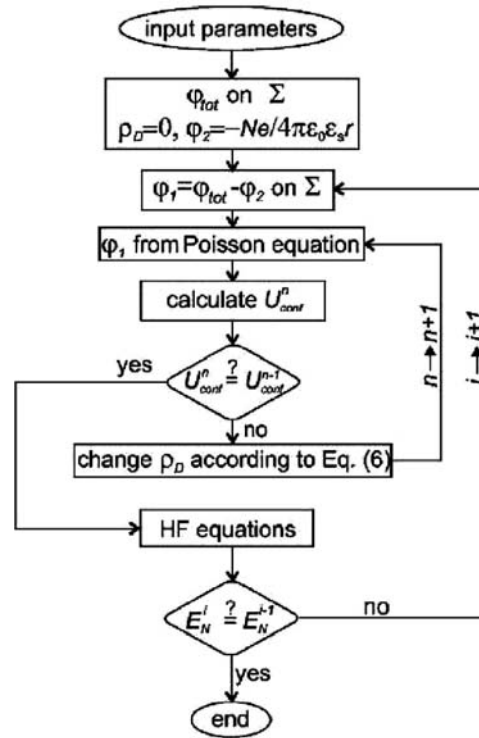
Figure 11. Block diagram of the self-consistent procedure for the solution of the Poisson and Hartree-Fock equations. $\varphi_{\text{tot}} = \Phi$ is the total electrostatic potential defined by Eq. (9). Equation (6) is equivalent to Eq. (13) in this chapter. A more detailed description is given in the text. From Ref. [86].

of the iterative procedure very well simulate the physical processes in the nanodevice, which last until the electron system achieves the stationary state.

Here the theoretical approach [84, 86] is presented in more detail. The potential energy of the electron confined in the QD is given by

$$U_{\text{conf}}(\mathbf{r}) = U_{\text{band}}(z) + U_{\text{elst}}(\mathbf{r}), \tag{7}$$

where $U_{\text{band}}(z)$ is the potential energy, which results from the band offsets (this is the single potential well/potential barrier in the two-terminal QD [6] and the double-barrier potential with the single-potential well in the three-terminal QD [7]), and $U_{\text{elst}}(\mathbf{r})$ is the potential energy of the electrostatic confinement

$$U_{\text{elst}}(\mathbf{r}) = -e\varphi_1(\mathbf{r}). \tag{8}$$

Electrostatic potential $\varphi_1(\mathbf{r})$ stems from all the charges in the nanodevice, excluding the charge confined in the QD. The main sources of the electrostatic field with potential $\varphi_1(\mathbf{r})$ are the ionized impurities and the charges on the leads. From the superposition principle, we obtain total potential $\Phi(\mathbf{r})$ of the net electrostatic field

$$\Phi(\mathbf{r}) = \varphi_1(\mathbf{r}) + \varphi_2(\mathbf{r}), \tag{9}$$

where $\varphi_2(\mathbf{r})$ is the potential of the electrostatic field created by the electrons confined in the QD.

Potential $\varphi_1(\mathbf{r})$ is the solution of the Poisson equation

$$\nabla^2 \varphi_1(\mathbf{r}) = -\frac{\varrho_D(\mathbf{r})}{\varepsilon_0 \varepsilon_s}, \tag{10}$$

where $\varrho_D(\mathbf{r})$ is the charge density of the ionized donors, ε_0 is the electric permittivity of vacuum, and ε_s is the relative static electric permittivity of the nanostructure. For layer nanostructures, ε_s changes across the interfaces; nevertheless, in the GaAs/AlGaAs–based nanostructures [6, 7] these changes are rather small. Therefore, in a fairly good approximation, ε_s was taken [86, 88] to be that of GaAs (i.e., $\varepsilon_s = 13.2$). In order to solve the Poisson equation, we have to put appropriate boundary conditions that include voltages applied to the leads. In the calculations [86, 88], the boundary conditions were imposed on the total potential $\Phi(\mathbf{r})$ and the boundary values of potential $\varphi_1(\mathbf{r})$ were calculated from Eq. (9).

Potential $\varphi_2(\mathbf{r})$, which stems from the QD confined electrons, can be approximated by the Hartree potential and is given by

$$\varphi_2(\mathbf{r}) = -\frac{\kappa e}{\varepsilon_s} \sum_{\nu=1}^{N} \int d^3 r' \frac{|\psi_\nu(\mathbf{r}')|^2}{|\mathbf{r} - \mathbf{r}'|}, \tag{11}$$

where $\kappa = 1/(4\pi\varepsilon_0)$ and $\psi_\nu(\mathbf{r})$ are the one-electron wave functions, which can be obtained from the Hartree-Fock method [86]. In Eq. (11), the sum runs over all the occupied one-electron states. The electrostatic field, created by the QD-confined electrons, which is described by potential (11), acts mainly on the remote charges in the n-GaAs layers; therefore, it is screened by the static electric permittivity ε_s.

In the two-terminal nanodevice of Ashoori et al. [6], the donors reside in the AlGaAs blocking barrier layer and in the n^+-GaAs substrate. All the donors in the barrier layer are ionized even at very low temperatures. For this layer, the charge density in Poisson equation (10) is simply calculated as $\varrho_D(\mathbf{r}) = -en_D$, where n_D is the donor concentration. The donors in the substrate are ionized by the electrostatic field. This process was treated [88] similarly as the ionization of donors in the three-terminal QD [7]. This ionization process is described next.

In the three-terminal nanodevice of Tarucha et al. [7], there are several n-GaAs layers with different donor concentrations. In equilibrium, the donor energy level (located ∼5 meV below the GaAs conduction band bottom) is aligned with the Fermi energy of the source and drain. Therefore, at the very low temperature, the donor ionization can only be caused

by the electrostatic field acting at the donor site. This leads to the following donor ionization condition: the donor center at position $\mathbf{r}$ becomes ionized if the potential energy of the electron in the total electrostatic field, that is,

$$U_{\text{tot}}(\mathbf{r}) = -e\Phi(\mathbf{r}), \tag{12}$$

is larger than the electrochemical potential of the adjacent reservoir (source or drain). Then, the electron goes over from the donor to the adjacent reservoir. If we take Fermi energy F as the reference energy and put $F = 0$, we obtain [86] the donor ionization condition in the form

$$\varrho_D(\mathbf{r}) = \begin{cases} -en_D(\mathbf{r}) & \text{if } U_{\text{tot}}(\mathbf{r}) > -eV_{s(d)}, \\ 0 & \text{otherwise}, \end{cases} \tag{13}$$

where $V_{s(d)}$ is the source (drain) voltage. Condition (13) allows us to determine the charge density in Poisson equation (10) in all the n-type layers in the three-terminal QDs [7] and in the substrate layer in the two-terminal QDs [6].

In the three-electrode QD [7], the electric-field-induced ionization of the donor occurs if the electron potential energy in the electrostatic field at the donor site is sufficiently large [see condition (13)]. Potential energy (12) depends on the confinement potential, which, in turn, depends on number N of QD-confined electrons. When considering the single-electron transport in the nanodevice [7], we deal with the problem of relaxation of the charges induced in the nanodevice during the single-electron tunneling via the QD. The theory in Ref. [86] is based on the assumption that the charge relaxation processes are slow. This means that during the tunneling of the $(N+1)$th electron the induced charges remain in the quantum states, which were adjusted to the state of N electrons confined in the QD. The slow relaxation leads to the following computational consequences: when determining the conditions of the tunneling of the $(N+1)$th electron through the QD, which consists of the N excess electrons we should calculate both the energies E_{N+1} and E_N—which define chemical potential μ_{N+1}—with the same confinement potential (i.e., which correspons to the presence of N electrons in the QD). Such an approach [86] leads to a good agreement with the experimental data [7, 23].

4.2. Boundary Conditions

Poisson problem (10) is uniquely formulated if the boundary conditions are set at a surface surrounding the integration domain. The boundary conditions should be imposed on total potential $\Phi(\mathbf{r})$ [Eq. (9)], which allows us to include all the charges in the nanodevice [86, 88]. The boundary values of potential $\varphi_1(\mathbf{r})$, needed to solve Poisson equation (10), are calculated from Eq. (9). For the electrostatic QDs, the boundary conditions at the surfaces of the electrodes are determined by the voltages applied to them. For the three-electrode QD [7] this leads to the following boundary conditions:

$$\Phi(\mathbf{r}_{\text{source}}) = V_s = 0, \tag{14}$$

at the inner surface of the source (for convenience we set the source potential equal to zero),

$$\Phi(\mathbf{r}_{\text{drain}}) = V_d \equiv V_{\text{ds}}, \tag{15}$$

at the inner surface of the drain, and

$$\Phi(\mathbf{r}_{\text{gate}}) = V_g - \phi_B/e, \tag{16}$$

where V_g is the gate voltage and ϕ_B is the height of the Schottky barrier at the semiconductor-metal interface. The Schottky barriers do not appear in the boundary conditions for the source and drain electrodes because they are made of the heavily doped n-GaAs, which form Ohmic contacts with the moderately doped n-GaAs adjacent layers.

To obtain the boundary conditions on the cylinder side, which is not covered by a metal, we assume that the electric field is parallel to the cylinder axis and solve the one-dimensional Poisson equation [86]. This assumption is exactly satisfied for the cylinder with the infinitely large radius. However, in the numerical calculations, we cannot use the infinite values. This problem was solved in Refs. [86, 88] by performing a series of calculations for different values of the radius of the cylinder, which limits the integration domain of the Poisson equation. For the purpose of the final calculation, we had chosen the cylinder radius value to be sufficiently large so that its further increase did not change the potential inside the QD. In the numerical practice, it is sufficient to choose the radius of the integration domain, which is three times larger than the radius of the cylindrical pillar in the nanodevice [6, 7]. The boundary conditions, calculated in such way for the two-electrode QD, are shown in Fig. 12.

4.3. Numerical Integration of the Poisson Equation

For the vertical QDs with the cylindrical symmetry [6, 7], Poisson equation (10) reduces to

$$\left(\frac{\partial^2}{\partial r^2} + \frac{1}{r} \frac{\partial}{\partial r} + \frac{\partial^2}{\partial z^2} \right) \varphi_1(r, z) = -\frac{\varrho_D(r, z)}{\varepsilon_0 \varepsilon_s}, \tag{17}$$

where r and z are the cylindrical coordinates. The cylindrical Poisson equation (17) was solved [86, 88] by the finite-difference relaxation method on the two-dimensional grid (r_i, z_j). The numerical solutions, that is, $\varphi_1(r_i, z_j)$, allow us to calculate the electrostatic confinement potential energy using formula (8).

Figure 13 shows the results for the two-electrode QD of Ashoori et al. [6], and Fig. 14 shows the results for the three-electrode QD of Tarucha et al. [7]. The lateral electrostatic confinement potential energy, displayed in Figs. 13 and 14, denotes quantity U_{elst} [Eq. (8)] calculated for z fixed inside the quantum-well layer and depicted as a function of radial coordinate r. In each figure, the Fermi energy, represented by the thick solid curve, shows the region of the QD occupied by the electrons. Figures 13 and 14 clearly show the effect of the charge confined in the QD on the electrostatic confinement potential energy. In both plots, we see the characteristic jumps of the potential energy. Each jump results from changing the number of QD-confined electrons by one. The results of Figs. 13 and 14 can
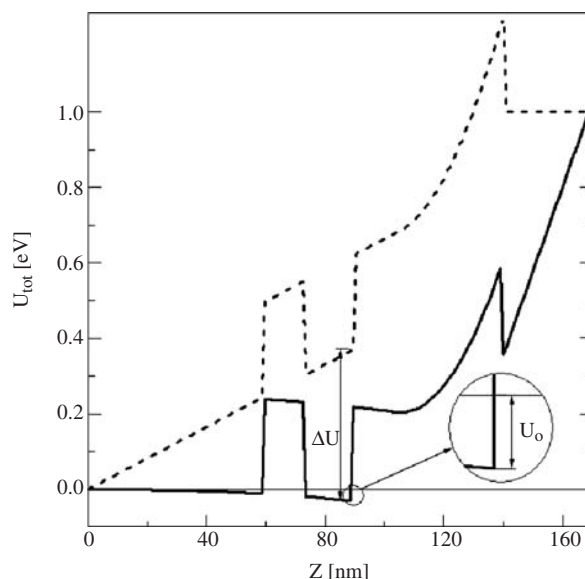
Figure 12. Boundary conditions put on total potential energy U_{tot} for $r = R_c$ (dashed curve) and potential energy U_{tot} calculated [88] along the cylinder axis (solid curve) as functions of vertical coordinate z for the two-terminal nanodevice [6]. U_0 and ΔU denote the vertical and lateral confinement potential-well depths, respectively. The thin horizontal line represents the Fermi energy. From Ref. [88].
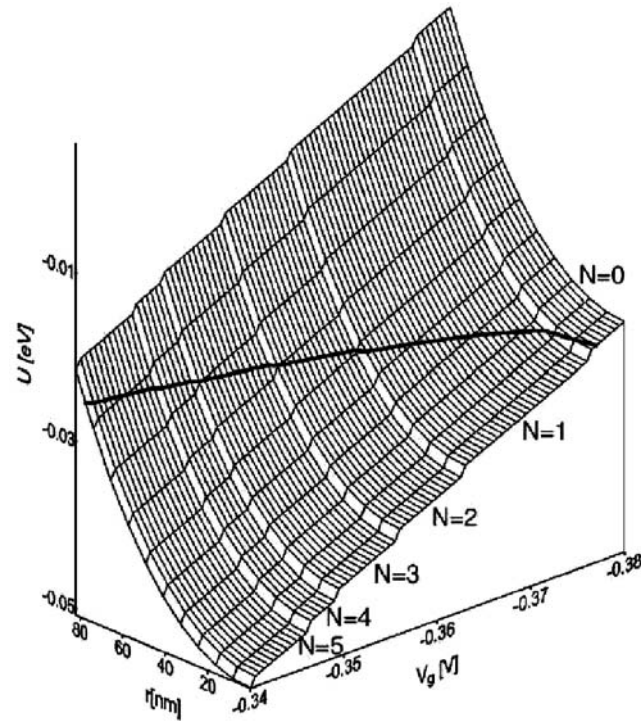
Figure 13. Lateral electrostatic confinement potential energy $U = U_{elst}$ of the electron in the two-electrode QD as a function of radial coordinate r, gate voltage V_g, and number N of QD confined electrons. The thick solid line corresponds to the Fermi energy. From Ref. [88].

be interpreted as follows: the increasing (negative) gate voltage leads to a lowering of the electron potential energy. This causes the binding of the subsequent electrons in the QD, which, in turn, leads to a further stepwise lowering of the electron potential energy. In both the two-terminal [6] and three-terminal [7] nanodevices, the dependencies of the electrostatic confinement potential energy on number N of the electrons confined in the QD are similar (see Figs. 13 and 14). The dependencies of the confinement potential on the gate voltage and radial coordinate do not exhibit such similarity. They will be discussed in Section 6.
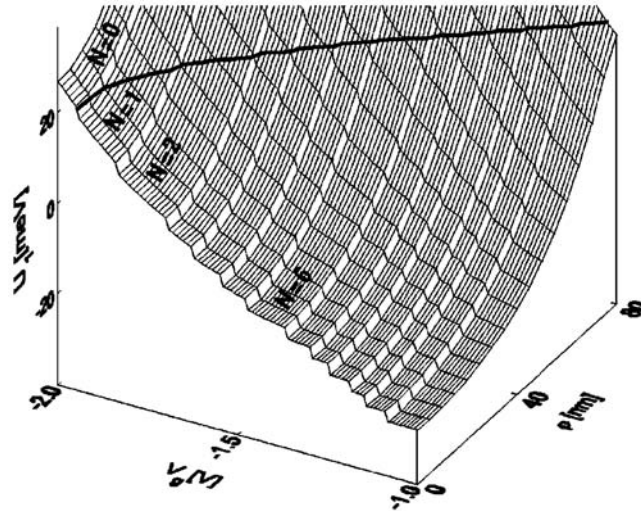
Figure 14. Lateral electrostatic potential energy $U_1 = U_{elst}$ of the electron in the three-electrode QD as a function of radial coordinate $\rho = r$, gate voltage V_g, and number N of QD confined electrons. The thick solid line represents the Fermi level. From Ref. [86].

4.4. Hartree-Fock Method

The quantum states of the electrons confined in the QD are the solutions of the eigenvalue problem with the N-electron Hamiltonian

$$H = \sum_{i=1}^{N}\left[h(\mathbf{r}_i) + \sum_{j>i}^{N}\frac{\kappa e^2}{\varepsilon_\infty r_{ij}}\right], \tag{18}$$

where

$$h(\mathbf{r}) = -\frac{\hbar^2}{2m_e}\nabla^2 + U_{\text{conf}}(\mathbf{r}) \tag{19}$$

is the one-electron Hamiltonian, m_e is the electron conduction band mass, $\mathbf{r}_i$ is the position of the ith electron, and $r_{ij} = |\mathbf{r}_i - \mathbf{r}_j|$ is the interelectron distance. The electron–electron repulsion, given by the second term in Eq. (18), is most effective for the electrons confined within the QD (i.e., it acts at small interelectron distances). The theory of the electron-LO-phonon coupling for the two-particle systems [105, 106] shows that the LO-phonon-induced screening can be neglected at small interelectron distances. Therefore, we screen this interaction by the high-frequency relative electric permittivity ε_∞.

The N-electron eigenequation with Hamiltonian (18) can be solved by the UHF method. A detailed description of the UHF method applied to the N-electron QD is given in Ref. [86]. When performing the UHF calculations, it is convenient to use the analytical form of the confinement potential. The different analytical forms of the confinement potential, fitted to the numerical solutions of the Poisson equation, are discussed in Section 6.

In the UHF calculations, the application of a Gaussian basis appears to be convenient. For the cylindrical QDs, the one-electron UHF wave functions

$$\psi_{ns}(\mathbf{r}) = \sum_{k_x k_y} c_{k_x k_y}^{ns} g_{k_x k_y}(\mathbf{r}) \tag{20}$$

are expanded in the Gaussian basis

$$g_{k_x k_y}(\mathbf{r}) = x^{k_x} y^{k_y} \exp[-\alpha(x^2 + y^2) - \beta z^2], \tag{21}$$

where $c_{k_x k_y}^{\text{ns}}$ are the linear variational parameters, α and β are the nonlinear variational parameters, n denotes the set of orbital quantum numbers, and s is the spin quantum number. Depending on number N of electrons and the total angular momentum of the system, different numbers of terms in expansion (20) were used [86].

5. QUANTUM COULOMB BLOCKADE

5.1. Theoretical Description of Single-Electron Tunneling

In the three-electrode nanodevice [7], a single electron can tunnel through the QD, which confines $(N-1)$ excess electrons, if the chemical potential of the resulting N-electron system falls within the interval determined by the the electrochemical potentials of the source and drain [condition (5)]. This interval is called a *transport window*. The width of the transport window depends on the external fields (i.e., bias voltage V_{ds} and gate voltage V_g). For voltages V_{ds} and V_g, for which single-electron transport condition (5) is not satisfied, the electron tunneling is blocked and we deal with the *Coulomb blockade* [12]. The classical model [89] of the Coulomb blockade is based on the charge quantization. According to this model [12], the charging energy equal to e^2/C is required to introduce the additional electron into the QD of capacitance C. This model leads to equally spaced tunneling current peaks, which are observed in large QDs as the so-called *Coulomb oscillations*. In the nanoscale regime, there appear quantum effects: the energy levels of the QD-confined electrons are discrete and are not equally spaced. Therefore, the charging energies are different for different numbers of electrons and the single-electron tunneling peaks exhibit unequal spacings [7]. This is a manifestation of the quantum nature of the Coulomb blockade [102].

In the three-terminal nanodevice [7], the source and drain electrodes are composed of the heavily doped n-GaAs layers and form the Ohmic contacts with the adjacent n-GaAs layers of the intermediate doping. The n-GaAs layers, close to the undoped GaAs spacer, are lightly doped with donors (see Fig. 4). Let us consider the single-electron tunneling through the quantum states of N electrons localized in the QD. In this process, the donors in the lightly doped n-GaAs layers, adjacent to the GaAs spacers, are the nearest located centers, which can give up or take on the electrons. These nearest donor centers mediate in the single-electron transport via the QD. Therefore, at low temperatures and zero bias, the electrochemical potential of the source and drain can be identified with the ground-state donor energy (E_D) in the n-GaAs layers. Even at the very low temperatures, the electrons are not frozen out in the donor states because of the considerable overlap between the weakly localized wave functions of the electrons bound to the donor centers in GaAs. Therefore, the small currents in the transport windows are carried via the overlapping donor wave functions.

According to condition (5), the single-electron transport can occur even if the bias voltage is negligibly small. For $V_{ds} = 0$, the common Fermi energy of the source and drain is taken as the reference energy and set equal to 0. Therefore, on the plot of chemical potential μ_N versus gate voltage drawn for $V_{ds} = 0$, the crossing point of μ_N with the abscissa determines the value of the gate voltage, which corresponds to the tunneling of the single electron via the QD. The results for the three-terminal QD are shown in Fig. 15. The theoretically predicted [86] positions of the single-electron tunneling current peaks very well agree with the experimental data [7], shown by the vertical lines in Fig. 15. The unequal spacings between the subsequent peaks result from the filling of the electronic shells in the artificial atoms. It can be seen from the upper panel of Fig. 15 that the distinctly larger separations between the second and third peaks and the sixth and seventh peaks correspond to the filling of the first and the second electronic shell, respectively. Moreover, the slightly larger distances between the fourth and fifth peaks and the ninth and tenth peaks correspond to the half-filled shells. These results can be treated as a quantitative proof that Hund's rule is satisfied for the artificial atoms [7].
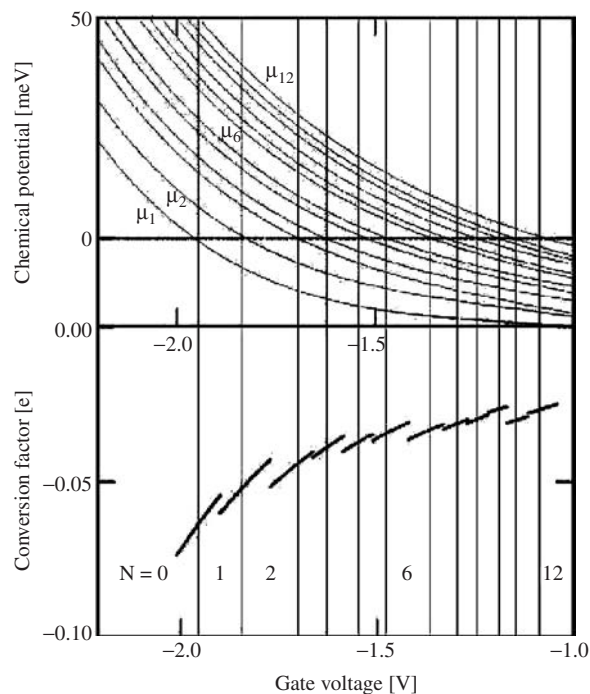
Figure 15. Chemical potential μ_N (upper panel) and conversion factor α_N for the three-electrode QD as functions of the gate voltage and number N of the QD confined electrons, calculated for $V_{ds} = 0$. The single electron can tunnel through the QD if $\mu_N = F = 0$. The measured positions of current peaks [7] are represented by the thin vertical lines. From Ref. [86].

The lower panel of Fig. 15 displays a gate voltage–to–energy conversion factor as a function of gate voltage. The conversion factor, defined as

$$\alpha_N(V_g) = \left. \frac{\partial \mu_N}{\partial V_g} \right|_{V_{ds}=0}, \tag{22}$$

enables us to convert the measured gate voltage into the energy of the electron quantum states. The conversion factor depends on number N of QD-confined electrons and the gate voltage. We note that the conversion factor for the three-terminal nanodevice [7] is a nonlinear function of the gate voltage. The calculated values of α_N change between $-0.07e$ and $-0.03e$ and show an overall agreement with the experimentally determined conversion factor [7, 23]. In particular, the absolute values of α_N decrease with N.

The single-electron tunneling in the two-electrode QD [6] takes place if condition (4) is satisfied. The chemical potential calculated for the artificial atoms, for which the electronic shells are closed (i.e., for $N = 2, 6, 12$, and 20), are depicted in Fig. 16. The positions of the crossing points of chemical potential μ_N with the Fermi energy agree very well with the experimental data [6].

Let us discuss a qualitative difference between the μ_N versus V_g dependencies for the two- and three-terminal nanodevices displayed in Figs. 16 and 15, respectively. For the two-electrode QD [6] the chemical potential is a perfectly linear function of the gate voltage (see Fig. 16). As opposite, for the three-terminal nanodevice of Tarucha et al. [7], the chemical potential is a highly nonlinear function of the gate voltage (see Fig. 15). In both nanodevices, the chemical potential is a decreasing function of V_g. The results of Fig. 16 also allow us to determine the conversion factor. It takes on the value of about $-0.5e$, which also results from the geometry of the nanostructure [6] (the same value can be estimated from the lever arm for the voltage drop). On the contrary, to the three-terminal nanodevice, the conversion factor for the two-terminal nanodevice is independent of the gate voltage. We also note that the absolute value of the conversion factor for the two-electrode QD [6] is by two orders of magnitude larger than that for the three-electrode QD [7]. These differences result from the different geometry of the three-terminal nanodevice [7], in particular, from the different location of the QD region relative to the electrodes.
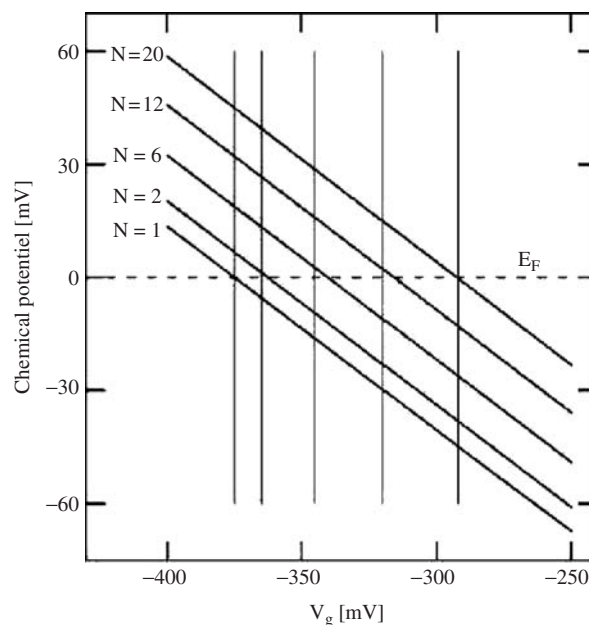
Figure 16. Chemical potential for the two-electrode QD as a function of gate voltage V_g and number N of electrons confined in the QD. The thin vertical lines mark the positions of the single-electron capacitance spectroscopy peaks [6]. The dashed horizontal line corresponds to the Fermi energy. From Ref. [88].

The results for the three-terminal nanodevice [7] at nonzero drain-source voltage are displayed on the stability diagram in Fig. 17. The shaded areas correspond to nonzero differential conductance measured by Kouwenhoven et al. [23]. The white diamond-shaped areas correspond to the Coulomb blockade (i.e., the vanishing differential conductance [23]). The solid curves show the calculated [86] boundaries between the gate and drain-source voltage regimes, which correspond to either zero or nonzero source-drain current. The curves with positive and negative slope are the plots of $\mu_{N+1} = \mu_s$ and $\mu_{N+1} = \mu_d$, respectively [see tunneling condition (5)]. All the solid curves were obtained under assumption of the tunneling through the corresponding ground state. The solid curves in Fig. 17 are in very good agreement with the experimental data [23]. The only exception is the tunneling condition, depicted by the solid curve for the eighth electron. However, it appeared that the calculations [86] performed under assumption of the tunneling through the first excited state of the eight-electron QD led to a better agreement with the experimental data [23] (see dashed curves in Fig. 17). Therefore, we tentatively interpreted the experimental data [23] for the eighth and ninth Coulomb diamonds (Fig. 17) assuming the single-electron tunneling through the first excited state of the eight-electron QD. The calculated [86] boundaries of the Coulomb blockade regimes, depicted by the solid and dashed curves in Fig. 17, very well agree with the measured [23] positions, sizes, and shapes of the Coulomb diamonds.

We note that the very good agreement with the experiment was obtained in Refs. [86, 88] with the use of the nominal values of the nanodevice parameters (i.e., composition, layer thicknesses, and donor concentrations). Only the radius of the cylindrical pillar in three-terminal QD [7] (the cap radius in the two-terminal QD [6]) was treated as a single adjusting parameter [86, 88]. This radius can not be measured with the appropriate precision but is merely estimated in the technological process from the radial size of the corresponding mask. This was the reason for treating the cylinder radius in the three-terminal nanodevice [7] and the cap radius in the two-terminal nanodevice [88] as the fitting parameters. Nevertheless, in either case, the fitted values of these radii were in a good agreement with the corresponding values estimated in the technological processes.
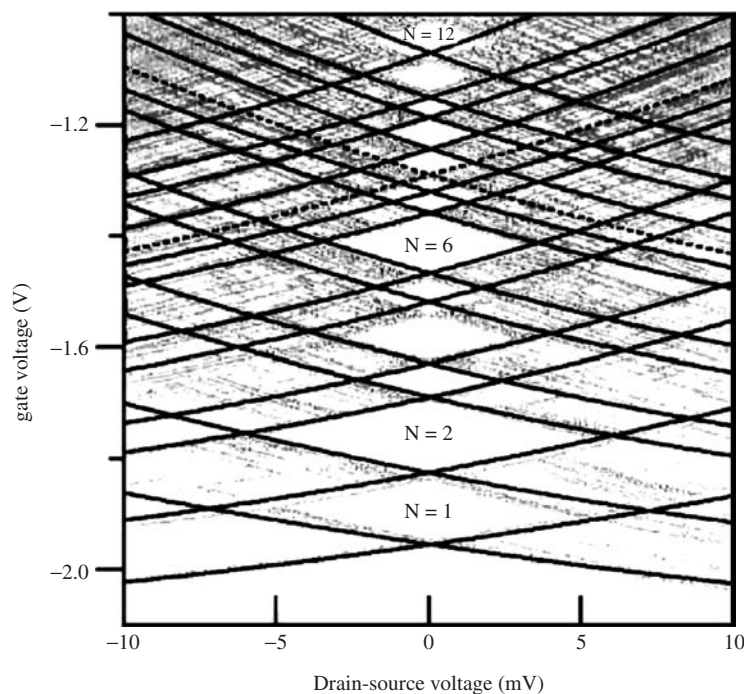

Figure 17. Stability diagram with Coulomb diamonds. The calculated [86] boundaries of the single-electron tunneling via the N-electron ground states (first excited state) are plotted with the solid (dashed) curves. The shaded areas represent the experimental data [23]. In the white diamond-shaped regions, the number N of the QD confined electrons is fixed. From Ref. [86].

5.2. Induced-Charge Density Distribution

The operation of nanodevices [6, 7] is strongly affected by the space charge distribution of the ionized donors. The ionized-donor charge density distribution is hardly accessible in experiments. However, it can be calculated in the framework of the self-consistent procedure by solving the Poisson-Schrödinger problem (see Section 4). In the two-electrode QD of Ashoori et al. [6] all the donors in the n-type doped AlGaAs barrier layer are ionized, and the corresponding charge density distribution is uniform [88].

The situation is much more complex in the n^+-GaAs substrate layer in the two-electrode QD [6] and in all the n-GaAa layers in the three-electrode QD of Tarucha et al. [7]. The ionized donor charge density distribution calculated [86] for the three-electrode QD is shown in Fig. 18(a)–18(d). The white, gray, and dark gray areas correspond to the charge density $\varrho_D = 0$, 1.0×10^{17}, and 1.4×10^{17} [e/cm^3]. The stepwise change of the ionized-donor charge density results from the stepwise changing donor concentration in the subsequent n-GaAs layers. Figure 18(a) and 18(b) show the results for $V_g = -1$ V and $V_g = -2$ V for the empty QD (i.e., for $N = 0$). In this case, the space charge is induced by the gate voltage only. The larger the absolute value of the gate voltage, the larger the range of the donor ionization. The effect of the electrons confined in the QD is shown in Fig. 18(c) and 18(d) for $N = 12$. The electrons confined in the QD induce the additional space charge in the central region of the nanodevice. Figure 18(a), 18(b), and 18(c) are plotted for $V_{ds} = 0$, which results in an approximate symmetry of the space charge density distribution against the inversion in the $z = 0$ plane. The slight asymmetry, caused by the small difference in the barrier widths, is visible in the figures. The application of the bias voltage entails the considerable asymmetry of the induced-charge distribution [see Fig. 18(d) for $V_{ds} = 50$ mV]. The results of calculations [86] show that the ionized donors should appear in only two n-GaAs layers in the three-electrode nanodevice of Tarucha et al. [7] [cf. Fig. 18(a)–18(d)].
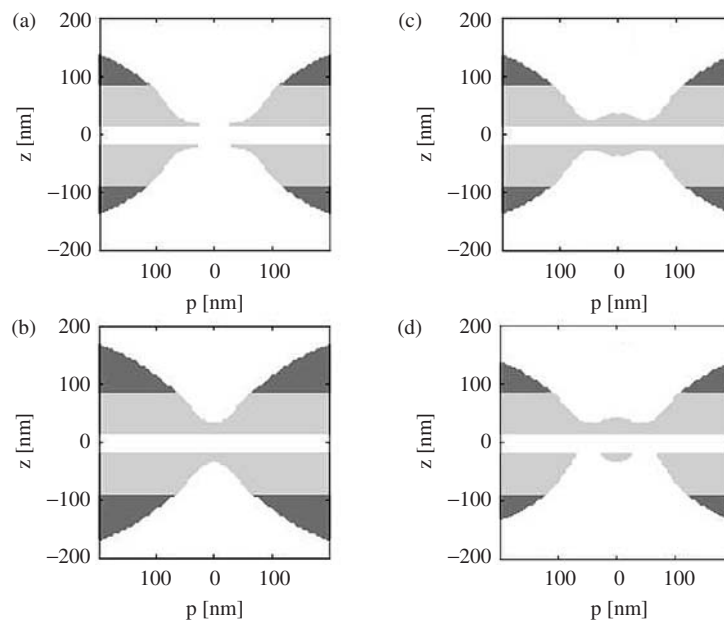
Figure 18. Charge density of the ionized donors in n-GaAs layers displayed in the vertical cross section of the three-terminal nanodevice [7] as a function of cylindrical coordinates $\rho = r$ and z. The white, gray, and dark gray areas correspond to charge density $\varrho_D = 0$, 1.0×10^{17}, and 1.4×10^{17} [e/cm^3], respectively. (a) $V_g = -1$ V, $V_{ds} = 0$, $N = 0$; (b) $V_g = -2$ V, $V_{ds} = 0$, $N = 0$; (c) $V_g = -1$ V, $V_{ds} = 0$, $N = 12$; (d) $V_g = -1$ V, $V_{ds} = 50$ mV, $N = 12$. From Ref. [86].

6. MODELING OF CONFINEMENT POTENTIALS

6.1. Three-Dimensional Profile of the Confinement Potential

The calculated [86, 88] 3D profile of the total confinement potential energy of the electron is shown in Fig. 19 for the two-terminal nanodevice [6] and in Fig. 20 for the three-terminal nanodevice [7]. Figures 19 and 20 show the total confinement potential energy of the electron calculated according to Eq. (7) (i.e., with the band-offset contributions included). In Fig. 19, the position of the Fermi energy marked by the thick solid curve, shows that in the two-terminal nanodevice [6] there are two regions in which the excess electrons can be localized. These are the QD regions and a part of the GaAs spacer close to the barrier layer. In the three-terminal nanodevice [7], the electrons can be confined in the lowest-energy part of the potential-well region between the two potential barriers. In this region of the nanodevice, the physical QD is formed.

6.2. Lateral Confinement

Let us consider the lateral confinement potential profile, that is, the dependence of the confinement potential on cylindrical radial coordinate r for z coordinate fixed inside the potential quantum well region. The lateral confinement potential energy is displayed in Figs. 13 and 21 for the two-electrode QD [6] and in Figs. 14 and 22 for the three-electrode QD [7]. It turns out that the dependence of the lateral component of the confinement potential on the gate voltage is different in both the nanodevices considered. In the two-terminal nanodevice [6], the curvature of the lateral confinement potential remains unchanged when changing the gate voltage. On the contrary, in the three-terminal nanodevice [7], the gate voltage strongly modifies the lateral confinement. In Figs. 21 and 22, we have also depicted the numerical solutions of the Poisson equation, the best analytical fits to these solutions, the parabolic fits, the electron charge density, and the Fermi energy. In both the QDs, the parabolic approximations are fairly good in that region of the QD, which corresponds to the electron energies below the Fermi level. The electrons are localized in this region of the QD and only slightly penetrate the nonparabolic region of the confinement potential. This partly justifies the commonly used parabolic approximation [72–75] of the confinement potential. However, the nonparabolic corrections do play a role in the single-electron tunneling [84]. A more detailed study [84, 86] of the electrostatic confinement potential in the central region of the three-terminal QD [7] shows that this potential can be very well approximated by the six-order polynomial of the form

$$\widetilde{\varphi}_1(r) = \sum_{m=0}^{3} v_m r^{2m}, \tag{23}$$
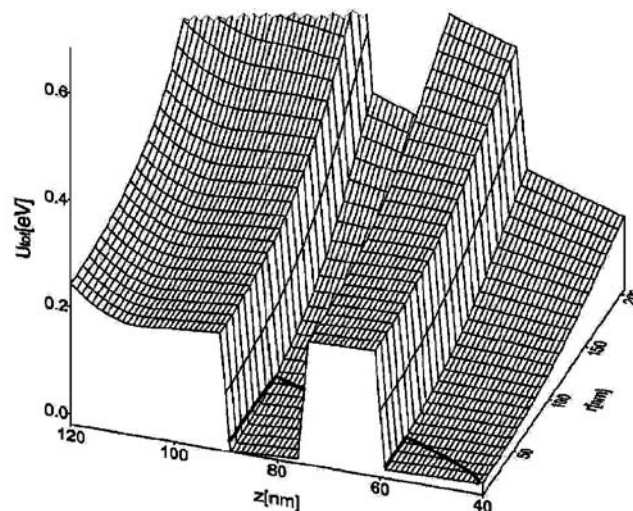
Figure 19. Total confinement potential energy $U_{\text{tot}} = U_{\text{conf}}$, Eq. (7), of the electron in the two-terminal nanodevice as a function of cylindrical coordinates r and z. The thick solid line corresponds to the Fermi energy. From Ref. [88].
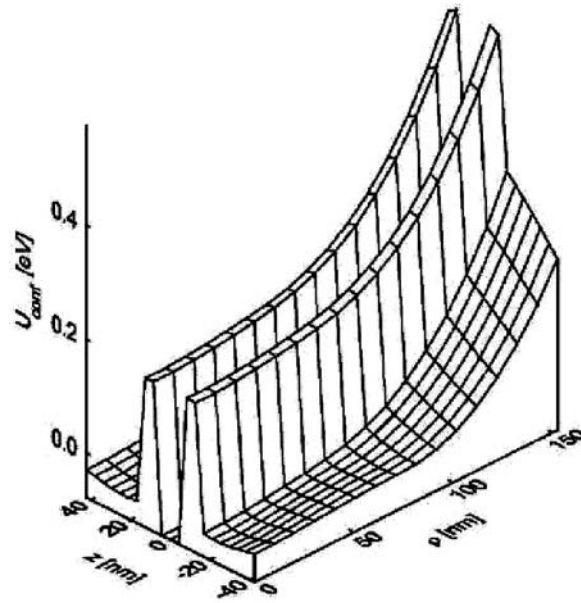
Figure 20. Total confinement potential energy U_{conf}, Eq. (7), of the electron as a function of cylindrical coordinates $\rho = r$ and z in the central region of the three-terminal nanodevice. From Ref. [86].

where coefficients v_0, v_1, and v_3 strongly depend on the gate voltage and the geometry of the nanodevice [86].

It is interesting to study the physical origin of the nearly parabolic shape of the confinement potential [86]. The results of this study [86] are shown in Fig. 23. Electrostatic potential φ_1 can be decomposed as follows:

$$\varphi_1 = \varphi_0 + \varphi_{resp}, \tag{24}$$
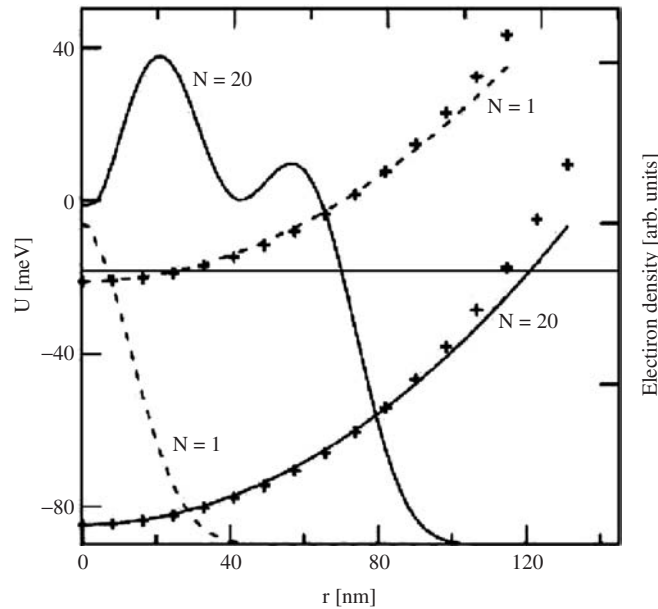
Figure 21. Lateral electrostatic confinement potential energy $U = U_{elst}$ (left scale) of the electron confined in the two-electrode QD as a function of radial coordinate r for z fixed inside the quantum-well layer for $N = 1$ and $N = 20$ electrons confined in the two-electrode QD [6]. Crosses represent the numerical solutions of the Poisson equation; solid and dashed lines display the parabolic fits. The corresponding electron-charge density (right scale) for $N = 1$ and $N = 20$ is plotted by solid and dashed curves. The thin horizontal line corresponds to the Fermi level. From Ref. [88].
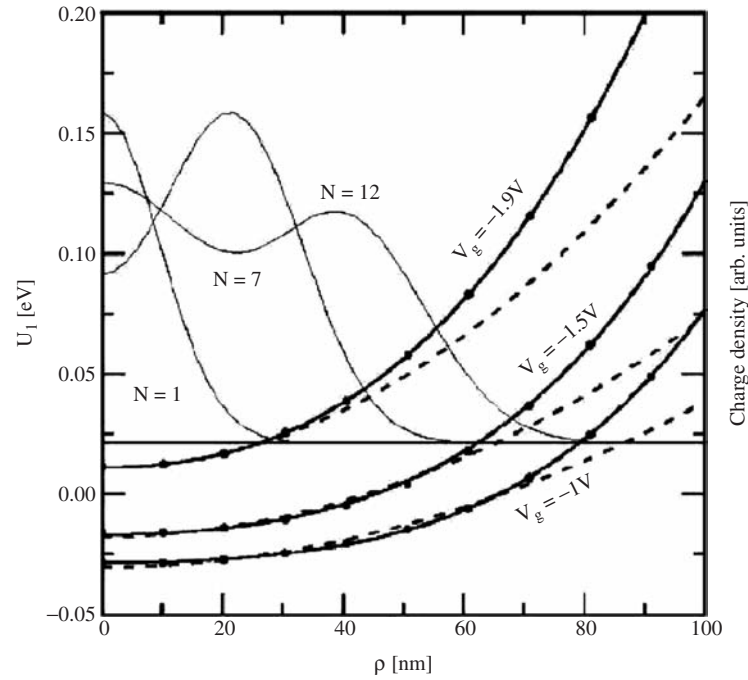
Figure 22. Lateral electrostatic confinement potential energy $U_1 = U_{elst}$ of the electron confined in three-electrode QD as a function of radial coordinate $\rho = r$ and gate voltage V_g for $V_{ds} = 0$ and $z = 0$. The dots represent the numerical solutions of the Poisson equation, solid curves represent sixth-order polynomials, fitted to these numerical solutions, and parabolic fits represent dashed curves. The thin solid curves show the charge density associated with N electrons confined in the QD. The QD confines $N = 1, 7,$ and 12 electrons for $V_g = -1.9$ V, -1.5 V, and -1 V, respectively. The solid horizontal line corresponds to the Fermi energy. From Ref. [86].
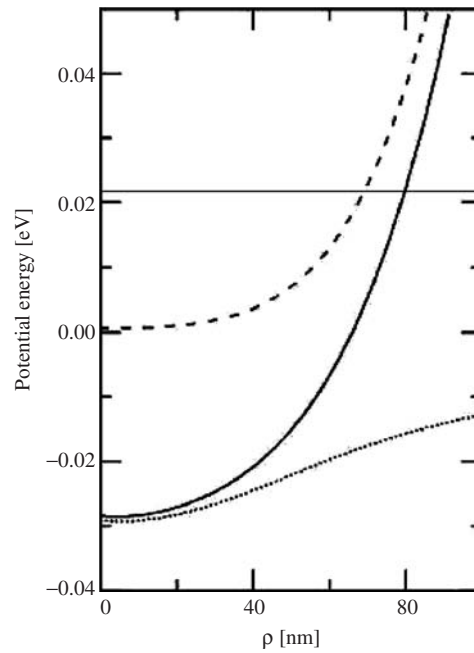
Figure 23. Total electron potential energy of the lateral confinement (solid curve) and its two components [Eq. (24)]: the potential energy of the empty QD ($-e\varphi_0$, dashed curve) and the potential energy ($-e\varphi_{resp}$, dotted curve) resulting from the response of the nanodevice to the presence of 12 electrons in the QD, as functions of radial coordinate $\rho = r$ for $z = 0$ in the three-terminal nanodevice. The thin dotted horizontal line corresponds to the Fermi energy. From Ref. [86].

where φ_0 is the potential created by the leads if no electrons are confined in the QD (the QD is empty) and φ_{resp} is the potential of the response of the nanodevice to the presence of N electrons within the QD. Potential φ_{resp} takes into account the screening of the electrostatic field created by the QD-confined electrons through the charges induced on the leads. Figure 23 displays the total electrostatic potential energy and its two components, which stem from potentials φ_0 and φ_{resp} [see Eq. (24)]. We note that both the components are strongly nonparabolic. According to Eq. (24), they sum up to the total electrostatic potential, which possesses the approximately parabolic shape. We conclude that the approximate parabolicity of the lateral confinement potential results from the superposition of the two nonparabolic potentials. Therefore, this is a nontrivial property of the confining potential.

The analytical formula for the confinement potential is very convenient when solving the Schrödinger equation for the confined few-electron system. For example, we used form (23) when solving the N-electron eigenproblem by the Hartree-Fock method [86]. Next, we discuss other useful analytical formulas for the shape of the lateral confinement potential. In Ref. [107], we introduced the power-exponential function, which allows us to model the shape of the lateral confinement potential in the entire nanodevice. According to this model [107], the lateral confinement potential energy has the shape

$$U(r) = -U_{0l} \exp[-(r/L)^p], \tag{25}$$

where U_{0l} is the depth of the lateral confinement potential energy, parameter L determines the lateral range of the confinement potential and can be treated as a measure of the lateral size of the QD, and power p ($p > 1$) is responsible for the steepness of the potential near the QD boundary. If p increases, starting from the value slightly exceeding 1, through $p = 2$ to the large values ($p \simeq 100$), function (25) models quasi-triangular, quasi-harmonic, and quasi-rectangular potentials (Fig. 24). The variety of the confinement potential shapes, obtained with power-exponential function (25), and the one-electron ground-state energy levels, calculated with the 3D spherically symmetric potential (25) are displayed in Fig. 24.
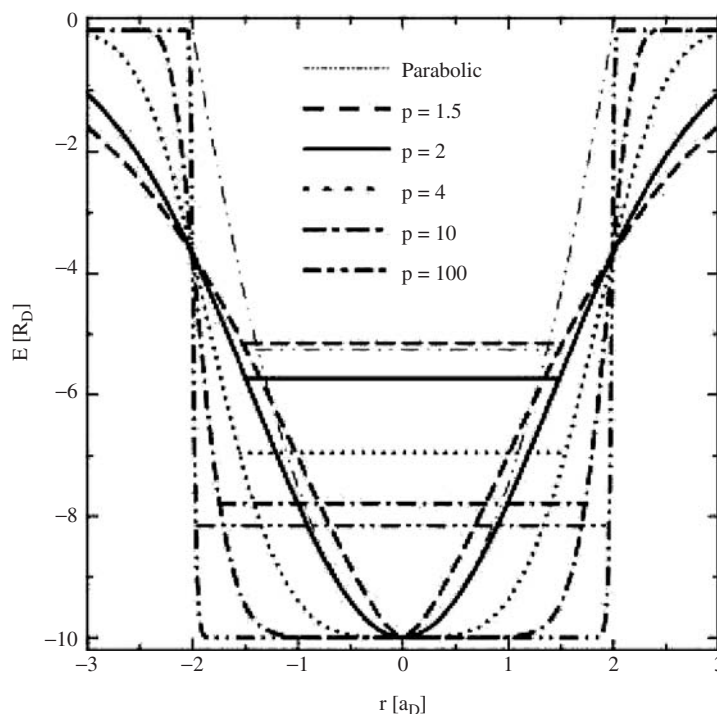
Figure 24. Power-exponential confinement potential for $L = 2\, a_D$, $U_{0l} = 10\, R_D$, and different values of p, and its parabolic approximation. a_D is the donor Bohr radius and R_D is the donor rydberg. The horizontal lines show the corresponding one-electron ground-state energy levels, calculated for the 3D spherically symmetric potential (25). From Ref. [107].

Model potential (25) can be generalized to the anisotropic form [107]

$$U(r, z) = -U_{0l} \exp[-(r/L)^p - (|z|/Z)^p], \tag{26}$$

where Z determines the range of the confinement in the vertical direction. The anisotropic confinement potential (26) can be applied to the modeling of the 3D confinement in both the electrostatic and self-assembled QDs. In particular, form (26) accounts for the different potential range in the lateral and vertical directions. We note that the modeling of the confinement potential, which is similar to that given by Eq. (25), can be obtained when using the model potential of the form [108]

$$U(r) = U_{0l}[(r/R)^p - 1]. \tag{27}$$

On the contrary, to power exponential (25), model potential (27) diverges for $r \to \infty$, that is, becomes unphysical at the boundary of the nanodevice.

The modeling of the confinement potential profile with the use of formula (25) was performed in Ref. [88] for the two-terminal QDs [6]. It appears [88] that by changing the cap radius R we can obtain the confinement potentials with different shapes. Figures 25(a)–25(d) display the lateral confinement potential energy calculated by the finite-difference numerical method from the Poisson equation and power-exponential function (25) fitted to these numerical solutions. In Fig. 25(a) and 25(d), the fitted parabolic functions are also plotted. Figure 25(a) shows the results obtained for the QD studied experimentally by Ashoori et al. [6] for the gate voltage at which the first electron is bound in the atomic-like state [88]. The results of Ref. [88] demonstrate that in the two-terminal QD of Ashoori et al. [6] the lateral confinement potential can be approximated by the parabola only near the center of the QD for the small cap radius. In the large region of the QD, the confinement potential strongly deviates from the parabolic form. Moreover, if the cap radius increases, the lateral confinement potential becomes strongly nonparabolic, that is, more flat near the center of
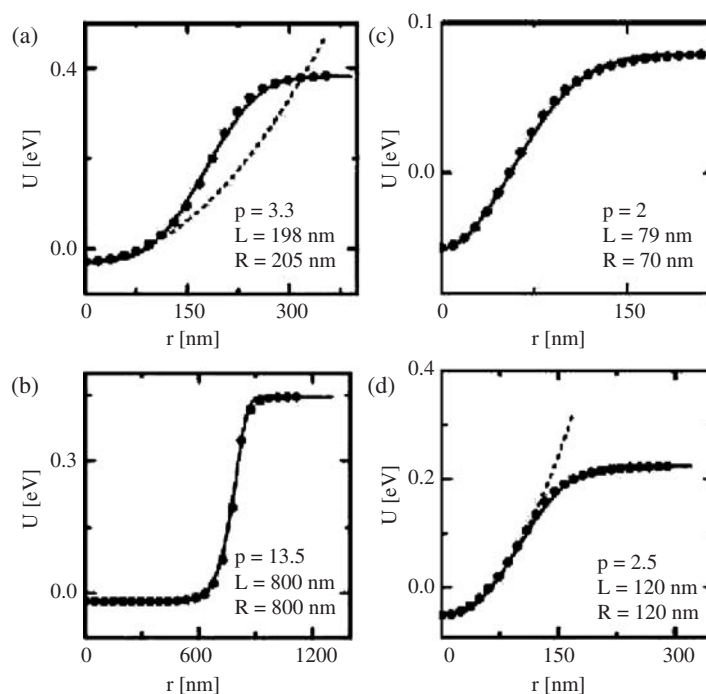
Figure 25. Lateral confinement potential energy U as a function of radial coordinate r for $z = z_0$ fixed within the quantum-well layer for the two-terminal nanodevice [6] with cap radius R. Dots represent the numerical solutions of the Poisson equation power-exponential function (25) with fitted parameters p and L, is shown by solid curves and fitted parabolic functions—dashed curves. (a) The results for the QD studied in Ref. [6], (b) flat-bottom steep-wall potential well, (c) Gaussian potential well, (d) the best parabolic fit over a large part of the QD. From Ref. [88].

the QD and more steep at the QD boundary. For sufficiently large R [see Fig. 25(b)], the confinement potential starts to resemble the rectangular potential well. This profile can be obtained by fitting potential (25) with large values of power p and range L. In real QDs [91], the flatness of the confinement potential causes that the electrons confined in the QD are sensitive to the fluctuating electric fields created by the randomly distributed impurities. As a result, the atomic-like energy levels of the QD-confined electrons are not well defined, which leads to the bunching of the energy levels observed [91] by the single-electron capacitance spectroscopy.

For small R [Fig. 25(c)] the confinement potential can be very well fitted over the entire nanodevice by the Gaussian potential well [109]. It is also possible to model the profile of the confinement to obtain the best parabolicity in the possibly large region of the QD. This nearly ideal parabolic shape is shown in Fig. 25(d).

In each of the QDs studied in Fig. 25(a)–25(d), the values of R and L are very close to each other. Since parameter L provides a direct measure of the physical size of the QD, the approximate equality $L \simeq R$ means that cap radius R itself yields an accurate estimate of the lateral spatial extension of the two-electrode QD [6].

6.3. Parabolic Confinement Potential

The results of Refs. [86, 88] show that in both the two- and three-terminal electrostatic QDs [6, 7] the lateral confinement potential can be quite well approximated by the harmonic oscillator potential. In particular, the parabolic approximation of the lateral confinement potential is applicable in the central part of the QD with a small radius. The possibility of application of the parabolic confinement is very convenient because, in this case, the electronic properties of the QD can be simply predicted.

The parabolic approximation of the lateral confinement potential energy has the form

$$\widetilde{U}(r) = U_0 + \frac{m_e \omega_0^2}{2} r^2, \tag{28}$$

where U_0 determines the position of the potential-well minimum (measured in the vertical direction [Fig. 12]), and confinement frequency ω_0 determines the shape of the confinement potential near the minimum. The quantum of the harmonic oscillator energy (i.e., $\hbar\omega_0$), is the energy of the lateral excitation and is usually called the *lateral confinement energy*. Quantities U_0 and ω_0 determine the electronic properties of the parabolic QD. The dependence of these quantities on the parameters of the two-terminal nanodevice was studied in Ref. [88]. Next, we present some of the results of Ref. [88].

Figure 26 shows the dependence of U_0 and $\hbar\omega_0$ on the gate voltage. In a good approximation, the confinement energy is constant when varying the gate voltage. Potential-well minimum U_0 decreases almost linearly with increasing V_g. Therefore, for the two-terminal QD [6], the gate voltage–to–energy conversion factor is nearly constant and equal to $\sim -0.5e$. The dependencies displayed in Fig. 26 for the two-terminal QD of Ashoori et al. [6] are qualitatively different from those obtained for the three-terminal QD of Tarucha et al. [7]. Because of its more complex geometry, the confinement energy in the three-terminal QD [7] is strongly dependent on the gate voltage and decreases from 6.7 meV to 5.4 meV if the number of the QD confined electrons increases from one to four. Moreover, in the three-terminal QD [7], position U_0 of the potential-well bottom is a nonlinear function of the gate voltage [86]. As a consequence, the conversion factor is strongly dependent on the gate voltage [86] (Fig. 15). In the two-terminal QD [6], the near independence of the conversion factor on the gate voltage results from its simple, plane capacitor–like structure [88]. It is visible on Fig. 26 that the increasing doping entails the downward shift of the linear functions $U_0(V_g)$.

The effect of the donor doping is shown in Fig. 27. In the donor concentration regime considered in Ref. [88], both the vertical potential-well minimum and lateral excitation energy are almost linear functions of the donor concentration. These linear dependencies can hardly be expected without performing the calculations.
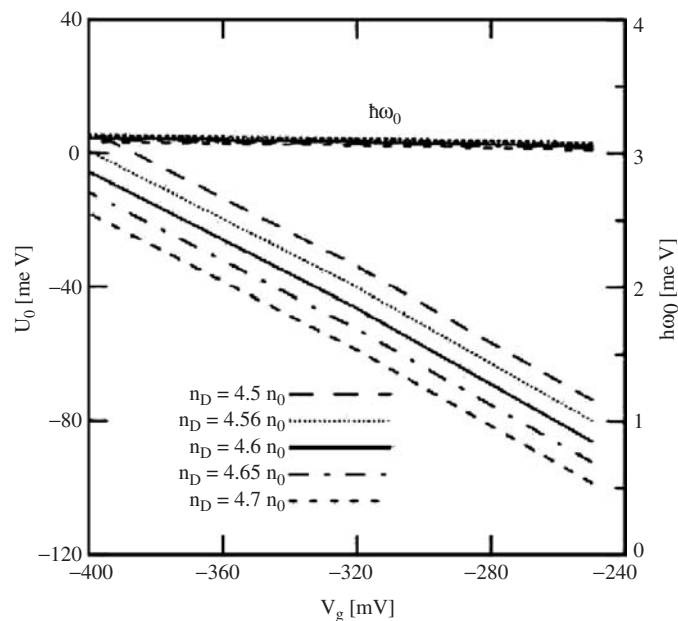
Figure 26. Minimal value U_0 (measured in the vertical direction) of electron confinement potential energy (left scale) and lateral excitation energy $\hbar\omega_0$ (right scale) as functions of gate voltage V_g for several donor concentrations n_D, where $n_0 = 10^{17}$ cm^{-3}, for the two-terminal nanodevice [6]. From Ref. [88].

Figure 28 displays the dependence of U_0 and $\hbar\omega_0$ on number N of the electrons confined in the two-terminal QD [6]. The dependence of the nanodevice parameters on the number of QD confined electrons for the two-terminal QDs [6] exhibits an essential qualitative difference in comparison to that for the three-terminal QDs [7]. In the QD of Tarucha et al. [7], U_0 and $\hbar\omega_0$ are nonlinear functions of N. Figure 28 shows that in the QD of Ashoori et al. [6] both the quantities U_0 and $\hbar\omega_0$ are approximately linear functions of N. The N-dependence of the nanodevice parameters results from the influence of the charge induced on the leads and in the n-doped layers by the QD confined electrons. This effect
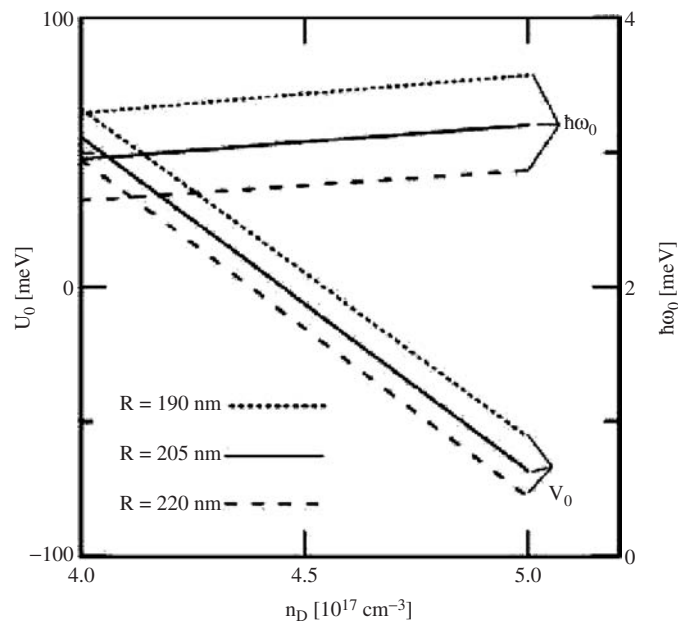
Figure 27. U_0 (left scale) and $\hbar\omega_0$ (right scale) as functions of concentration n_D of the ionized donors and cap radius R for the two-terminal nanodevice [6]. Symbols have the same meaning as in Fig. 26. From Ref. [88].
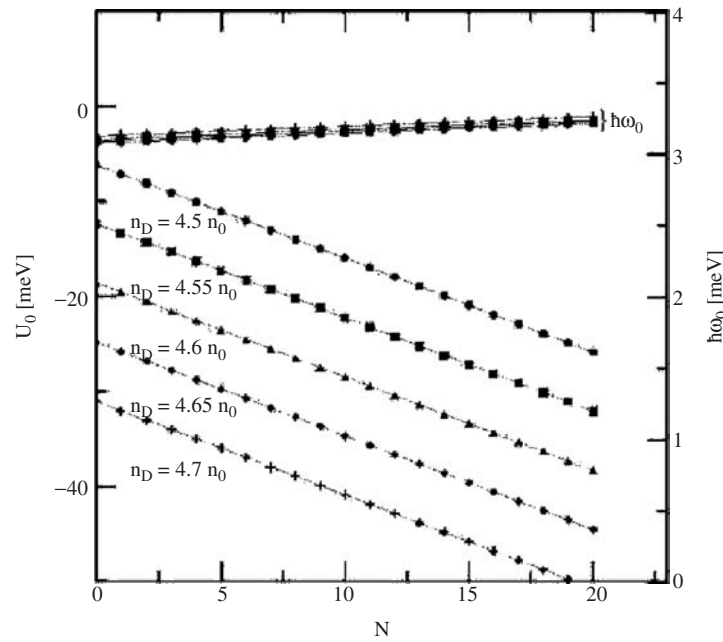
Figure 28. U_0 (left scale) and $\hbar\omega_0$ (right scale) as functions of number N of QD confined electrons for several donor concentrations n_D, where $n_0 = 10^{17}$ cm^{-3}, for the two-terminal nanodevice [6]. Symbols have the same meaning as in Fig. 26. From Ref. [88].

considerably modifies the electronic properties of the QD. In the electrostatic QDs, the number of the QD-confined electrons is controlled by the gate voltage. Therefore, the differences in the properties of both the types of QDs are translated into the different dependencies of the nanodevice parameters on the gate voltage.

The cap radius dependence of the confinement potential parameters is very interesting (Fig. 29). Figure 29 shows that the dependencies of both the lateral excitation energy and vertical potential energy minimum on cap radius R are highly nonlinear. The minimum value
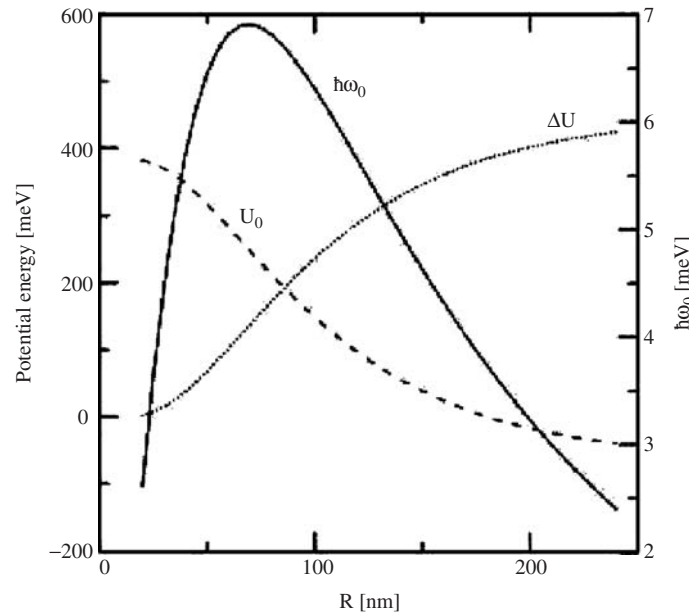
Figure 29. Confinement potential energy minimum U_0 (measured in the vertical direction), lateral confinement potential well depth $\Delta U = U_{0l}$ (left scale), and lateral excitation energy $\hbar\omega_0$ (right scale) as functions of cap radius R for $n_D = 4.62 \times 10^{17}$ cm^{-3} and $V_g = -0.375$ mV for the two-terminal nanodevice [6]. From Ref. [88].

U_0 of the vertical confinement potential energy quickly decreases with increasing R. Energy $\hbar\omega_0$ of the lateral excitation is a nonmonotonic function of R and takes on the maximal value $\hbar\omega_0 \simeq 7$ meV at $R = 65$ nm, which corresponds to the nearly ideal Gaussian shape of the lateral confinement potential [cf. Fig. 25(c)]. Figure 29 also displays quantity $\Delta U = U_{0l}$ [cf. Eq. (25)] (i.e., the depth of the confinement potential measured in the lateral directions), which is responsible for the lateral confinement of electrons.

In general, the dependence of the confinement potential on the nanodevice parameters is complex. When determining this dependence by computational methods, one has to repeat the calculations for each nanostructure. An important property of the confinement potential can be found by a simple scaling without performing the numerical calculations [110]. For this purpose, we consider the radial Poisson equation (17). If we multiply all the coordinates by factor k and simultaneously divide the charge density by k^2, we obtain the electrostatic potential as a function of the coordinates, expressed in the unit of length multiplied by k, which is the same function of the coordinates as that for $k = 1$. We note that the multiplication of the coordinates by k is equivalent to multiplying by k all the geometric sizes of the nanodevice. This scaling property applied to the parabolic QD means that we can obtain the k times larger confinement energy if we build the nanodevice with k-fold-decreased linear sizes and k^2 times stronger doping of the barrier layer [110].

7. EFFECT OF EXTERNAL MAGNETIC FIELD

The application of an external magnetic field essentially modifies the electronic states in the QDs [6, 23, 24]. In the increasing magnetic field, the ground state of the QD-confined electron system undergoes the symmetry transformations, which are accompanied by the abrupt changes of the ground-state energy. Therefore, these transformations can be treated as phase transitions in the N-electron system. Especially interesting phases are created at very high magnetic fields, at which the island-like charge-density distributions (i.e., Wigner molecules) are formed. At the extremely high magnetic field, the spatial structure of the Wigner molecule becomes the same as that of the classical point charge system [111].

The single-electron transport [23] and capacitance [6] spectroscopy measurements in the external magnetic field yield a rich information about the symmetry of the confined electron states, the localization of the electrons, and the relative strength of the electron–electron interaction. In particular, the joint effect of the external magnetic field and the electric field between the source and drain is one of the most interesting characteristics of the nanodevice [23, 24]. This joint magnetic- and electric-field effect on the single-electron transport was studied experimentally by Kouwenhoven et al. [23] and theoretically by us [98].

In the presence of the external magnetic field, the one-electron Hamiltonian (19) acquires the additional terms, that is, takes on the form

$$h(\mathbf{r}) = -\frac{\hbar^2}{2m_e}\nabla^2 + U_{\text{conf}}(\mathbf{r}) + \frac{m_e\omega_c^2}{8}(x^2 + y^2) + \frac{\hbar\omega_c}{2}l_z + \frac{1}{2}g^*\mu_B B\sigma_z, \qquad (29)$$

where $\omega_c = eB/m_e$ is the cyclotron frequency for magnetic field $\mathbf{B} = (0, 0, B)$, l_z is the operator of z component of angular momentum, g^* is the effective Lande factor, μ_B is the Bohr magneton, and σ_z is the Pauli spin z matrix. The last term in Eq. (29) leads to the spin Zeeman splitting. For GaAs at the magnetic field, not exceeding few tesla this term yields the energy contribution, which is much smaller than that of the other terms and is usually neglected. However, at higher magnetic fields, the spin Zeeman energy has to be included.

To determine the conditions of the single-electron tunneling [cf. conditions (4) and (5)], we apply the same self-consistent procedure as that presented in Section 4, with the N-electron Hamiltonian modified according to Eq. (29). In Ref. [98], the UHF method with the one-electron wave function expanded in the Gaussians [cf. Eqs. (20) and (21)] was implemented for the three-terminal nanodevice [7].

Let us comment on the electric field dependence of the problem [98]. One-electron Hamiltonian (29) does not include the electric field. However, the effect of this field was taken into account in an indirect way via the boundary conditions put on the electrostatic

potential on the source, drain, and gate when solving the Poisson equation. The direct effect of the bias voltage (i.e., the potential energy drop between the source and drain), was shown in Ref. [98] to be reduced to the corresponding change of energy within the thin central region of the nanostructure and was estimated [98] to be smaller than ~1 meV. Such a drop of the potential across the width of the QD is too small to deform the wave function of the vertical size-quantized motion. Therefore, the direct influence of the bias voltage was neglected in Ref. [98].

The magnetic-field effect on the first two capacitance peaks is shown in Fig. 30 for the two-electrode QD [6]. These peaks correspond to the QDs with one and two confined electrons for which the Schrödinger equation was solved with an arbitrary accuracy by the imaginary-time method [112, 113]. Therefore, the results of Fig. 30 are not affected by the electron correlation and can be treated as "exact" [88]. The agreement of the results of calculations [88] with the experiment [6] is good, although some deviations at high magnetic fields are visible. These deviations can result from some additional effects, neglected in Ref. [88] (e.g., a dependence of the Schottky barrier on the magnetic field [88]).

For the QDs subject to the external magnetic field, the plots obtained by both the single-electron capacitance spectroscopy (Fig. 7) and transport spectroscopy (Fig. 9) led to a discovery [6, 23] of the phase transitions in the QD confined electron system. The plots in Figs. 7 and 9 in fact show the chemical potentials of N-electron artificial atoms as functions of the magnetic field. The chemical potential is calculated as the difference between the corresponding ground-state energies [see Eq. (3)]. Therefore, we find the magnetic-field-induced phase transition if the ground-state energy exhibits a jump, which results in a kink of the chemical potential. For example, in Fig. 30, the kink for $N = 2$ at $B \simeq 2$ T corresponds to the singlet-triplet phase transition. It is seen that the calculated [88] and measured [6] positions of this kink very well agree (i.e., the calculations [88] reproduce this phase transition).

The influence of the magnetic field on the chemical potential of the three-electrode QD is depicted in Fig. 31. For $V_{ds} = 0$, the electrons occupy the QD energy levels up to the common electrochemical potential of the source and drain (i.e., up to the Fermi level), which corresponds to zero on the energy scale (Fig. 31). The chemical potential of the QD-confined electron system changes stepwise when changing the number of the confined electrons by one (see steps in Fig. 31). The cusps on the steps in Fig. 31 correspond to the magnetic-field-induced phase transitions. The results of Fig. 31 can be translated into the positions of the single-electron current peaks on the $V_g - B$ plane (Fig. 32) by using the conversion factor [Eq. (22)]. Figure 32 shows the magnetic-field dependence of the gate voltage, which corresponds to the boundaries of the transport windows for small bias ($V_{ds} = 0.1$ mV).
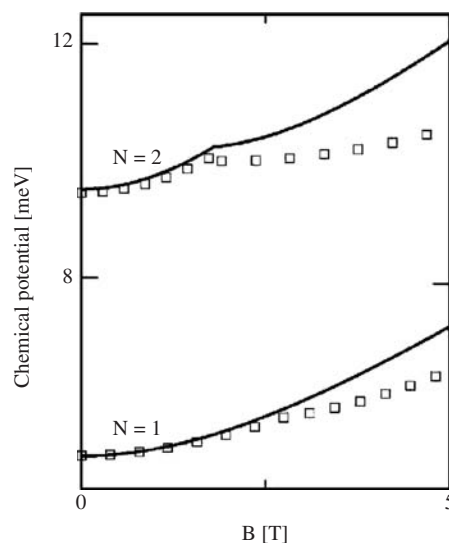
Figure 30. Chemical potential calculated for $N = 1$ and $N = 2$ electrons confined in the two-electrode QD as a function of magnetic field B. The squares mark the experimental data [6]. From Ref. [88].
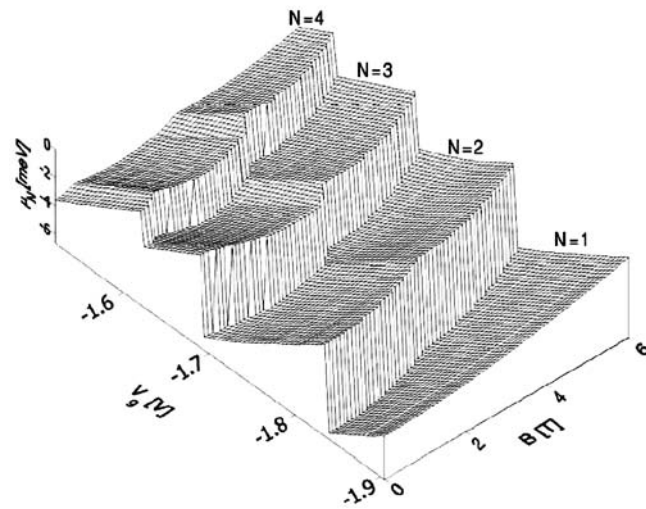
Figure 31. Chemical potential μ_N of N electrons confined in the QD as a function of magnetic field B and gate voltage V_g for drain-source voltage $V_{ds} = 0$. Zero on the energy scale corresponds to the Fermi energy. From Ref. [116].

At this bias, the single-electron transport conditions [Eq. (5)] are satisfied only within the very narrow stripes (i.e., inside the solid lines in Fig. 32). In the other areas of the $V_g - B$ plane, the Coulomb blockade occurs. The kinks in Fig. 32 correspond to the phase transitions that appear between the different N-electron ground states. The occupied one-electron
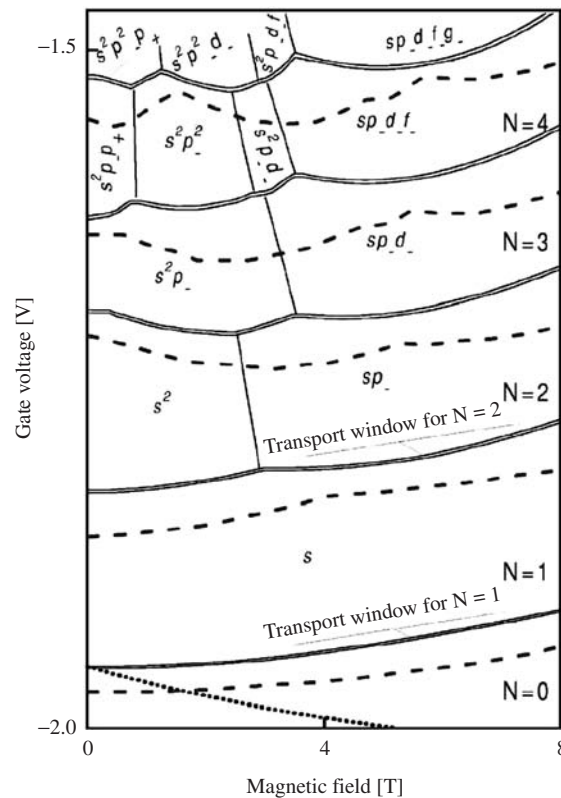
Figure 32. Transport windows as functions of gate voltage and magnetic field for $V_{ds} = 0.1$ mV. The solid (dashed) curves show the calculated [98] (measured [23]) gate voltage at which the single electrons tunnel through the QD. Number N of QD confined electrons is fixed in the Coulomb blockade regions and oscillates between $N - 1$ and N in the transport windows. The ground-state orbitals are denoted by the appropriate symbols (see the description in the text). The thin solid lines separate the regions corresponding to the different N-electron ground states. From Ref. [98].

orbitals are denoted by symbols s, p, d, f, and g, which correspond to the z component angular-momentum quantum numbers $m = 0, 1, 2, 3$, and 4, respectively. The "$\pm$" signs in the subscripts are the signs of the angular-momentum z-component. In each N-electron ground state, the total spin z component, S_z, takes on the maximal value, which is allowed for the given orbital. The last phase transition (i.e., at the highest magnetic field), leads to the fully spin-polarized state, that is, $S_z = \hbar$ for $N = 2$, $S_z = (3/2)\hbar$ for $N = 3$, and so on. Single-electron transport condition (5) contains the chemical potential, which, in this section, is the difference of the N- and $(N - 1)$-electron ground-state energies. Therefore, the N-electron ground-state energy E_N enters twice into the transport conditions for $(N - 1)$- and N-electron QDs. Therefore, each ground-state transformation is observed two times on the plots in Fig. 32. The points, which correspond to the same phase transition, are connected by the thin straight lines in Fig. 32. The results of calculations [98] fairly well agree with experimental data [23]. We note that calculations [98] were performed under assumption that the single-electron tunneling occurs via the weakly localized donor states in the n-GaAs layers.

The results shown in Fig. 32 illustrate the situation when the transport windows are only slightly open. The application of the larger bias entails the wider opening up of the transport windows. The results of calculations [98] for $V_{ds} = 1$ mV and $V_{ds} = 3$ mV are displayed in Fig. 33(a) and 33(b), respectively. In these figures, the solid and dotted curves correspond to the processes described by transport conditions (5) with equality signs for which the QD chemical potential is aligned with the electrochemical potential of the drain and source, respectively. In the Coulomb blockade regions (gray areas), the number of electrons confined in the QD is fixed (i.e., $N = $ const), while in the transport windows (white areas), the number of bound electrons oscillates between $N - 1$ and N. The results of Fig. 33(a) and 33(b) exhibit a very good qualitative and reasonable quantitative agreement with experiment [23]. Figures 32 and 33 show that the transport windows open up (the Coulomb-blockade regions shrink) with the increasing drain-source voltage.
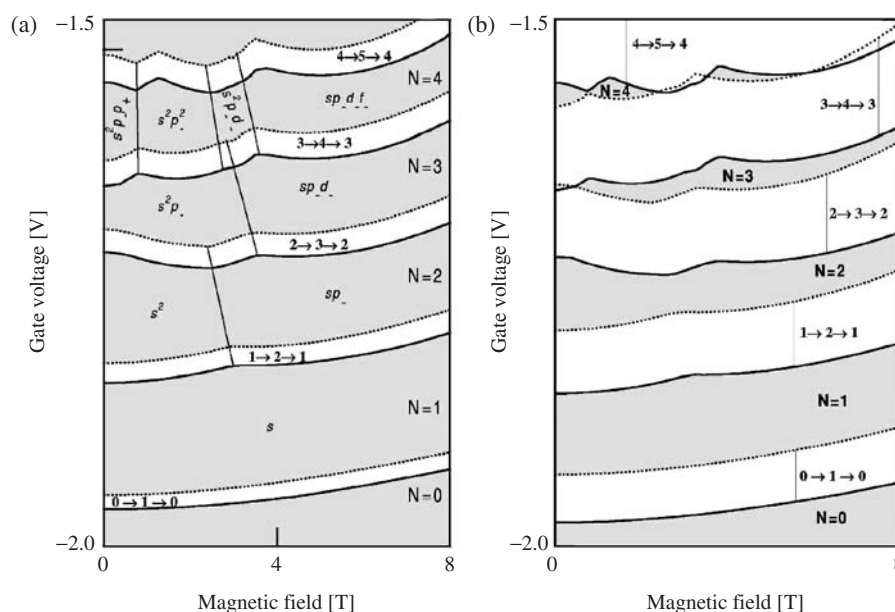
Figure 33. Transport windows (white areas) and Coulomb blockade regions (gray areas) as functions of gate voltage and magnetic field for drain-source voltage. (a) $V_{ds} = 1$ mV and (b) $V_{ds} = 3$ mV. The solid (dashed) curves show the calculated [98] gate voltage, for which the chemical potential of the N-electron QD is aligned with the electrochemical potential of the drain (source). In (a) the ground-state orbitals are denoted by the symbols, defined in the text, and the thin solid lines connect the points corresponding to the same ground-state transformation. In (b) the thin vertical lines connect the boundaries of the subsequent transport windows. Number N of QD confined electrons is fixed in the Coulomb blockade regions. The symbols in the transport windows show how N oscillates during the single-electron tunneling. From Ref. [98].

8. CORRELATION EFFECTS

When studying the correlation effects [114, 115], the results of the restricted Hartree-Fock (RHF) method are treated as reference data, since the electron–electron correlation is completely neglected in the RHF method. However, the unrestricted UHF method takes into account a part of the correlation [114, 115]. The calculations [86, 98] for the three-electrode QD were performed with the help of the UHF approach. In this section, we ask, how the incorporation of the correlation into the calculations will change the results obtained in Refs. [86, 98]? Theoretical studies of the correlation effects have been performed (e.g., in Ref. [116] for the single QD and in Refs. [114, 117] for the coupled QDs). For the systematic study of the correlation effects in few-electron system, the configuration interaction (CI) method can be applied [116, 117].

For the cylindrical QD, the one-electron wave functions for quantum state ν can be expanded [116] in the Gaussian basis [cf. Eqs. (20) and (21)]:

$$\psi_\nu(\mathbf{r}) = \sum_{k_x, k_y=0}^{k_x+k_y \leq K} c_{k_x k_y}^\nu x^{k_x} y^{k_y} \exp[-\alpha(x^2 + y^2) - \beta z^2], \tag{30}$$

where α and β are the nonlinear variational parameters and K determines number M of basis elements as follows: $M = (K + 1)(K + 2)/2$. The Slater determinants, constructed from one-electron wave functions (30), form the basis for the diagonalization of the N-electron Hamiltonian by the CI method. In the cylindrical QD, in the presence as well as in the absence of the external magnetic field, the N-electron eigenstate possesses the definite z components of both the total angular momentum and total spin, which will be labeled by the corresponding quantum numbers (L, S). Basis (30) with M elements allows for a construction of the following number of Slater determinants with definite L and S:

$$N_S = \binom{(K + 1)(K + 2)}{N}. \tag{31}$$

The calculations [116] were performed for $N = 2, 3$, and 4 electrons and angular-momentum quantum numbers $L = 0, \ldots, 6$. At zero magnetic field, the systems with $N = 2, 3$, and 4 electrons are in the ground states with the corresponding quantum numbers $(L, S) = (0, 0), (1, 1/2)$, and $(0,1)$. The total numbers of Slater determinants, used in calculations [116], were $N_S = 70, 377$, and 2174 for $N = 2, 3$, and 4, respectively. For these numbers of the Slater determinants [116], basis (30) with $M = 21$ elements ensures the accuracy $\sim$0.01 meV. Because of this high accuracy, the CI results can be treated as "exact."

The CI method was applied [116] to both idealized and real QDs. The idealized QD is described by the parabolic lateral confinement potential

$$\widetilde{U}(x, y) = \frac{m_e \omega_0^2}{2}(x^2 + y^2), \tag{32}$$

where ω_0 is the confinement frequency. The lateral confinement potential in the three-electrode QD of Tarucha et al. [7] can be approximated by the parabolic form with $\hbar\omega_0 \simeq 6$ meV for $N \leq 4$.

In the single-electron transport spectroscopy, the quantity of crucial interest is the chemical potential of the electrons confined in the QD. Figure 34(a)–34(c) display the few-electron chemical potentials calculated by the CI and HF methods [116]. In Ref. [116], the spin-unrestricted spatial-restricted HF method was applied, that is, the wave functions used in the calculations were the eigenfunctions of the z angular momentum, but it was not required that the orbital wave functions be the same for the opposite spins. The plots are drawn for the weak ($\hbar\omega_0 = 2$ meV), intermediate ($\hbar\omega_0 = 6$ meV), and strong ($\hbar\omega_0 = 10$ meV) confinement. For the weak confinement [see Fig. 34(a)], the HF results are unreliable both quantitatively and qualitatively. The HF approach predicts the incorrect symmetry of the ground state, for example, the low-spin state $(2, 0)$, which is the true ground state of the four-electron system over a wide range of the magnetic field, was erroneously predicted to
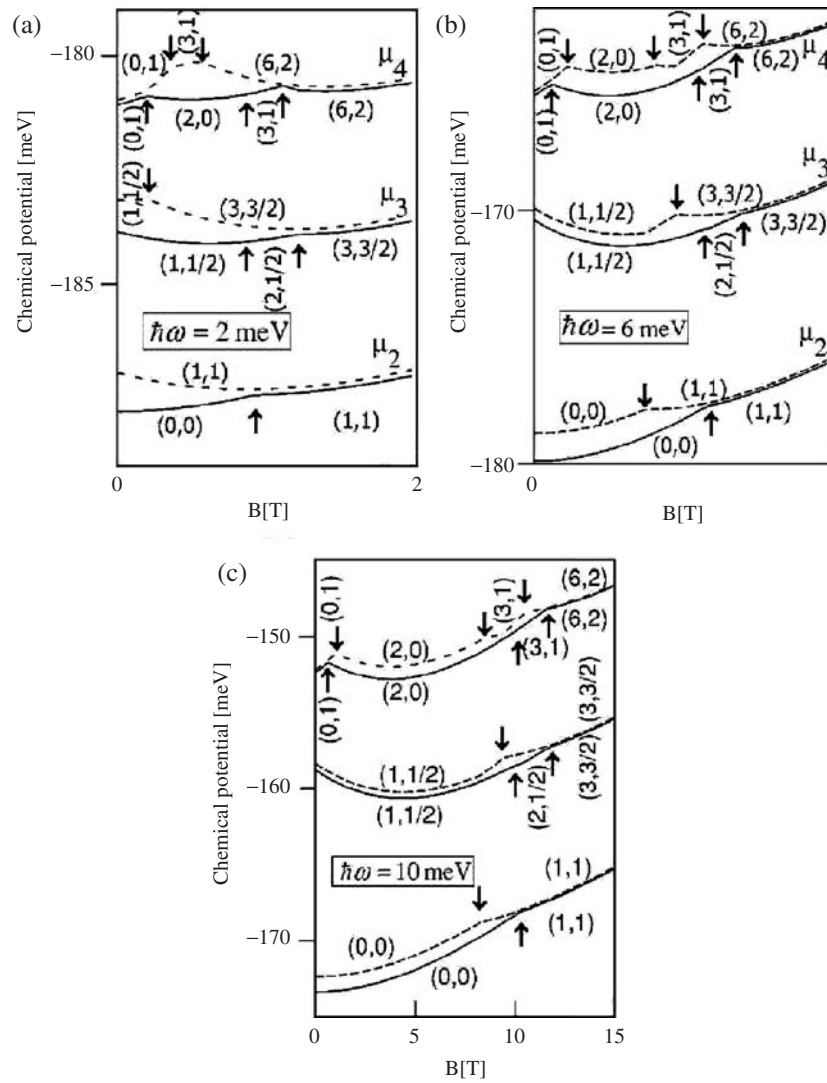
Figure 34. Chemical potential μ_N calculated with the confinement energy (a) $\hbar\omega_0 = 2$ meV, (b) $\hbar\omega_0 = 6$ meV, and (c) $\hbar\omega_0 = 10$ meV, as a function of number N of QD-confined electrons and magnetic field B. The solid (dashed) curves show the results obtained by the CI (HF) method. Quantum numbers (L, S) correspond to the ground state. The arrows up (down) show the magnetic-field-induced transformations obtained with the CI (HF) method. From Ref. [116].

be the excited state in the HF method. The HF method usually prefers the high-spin state to be the ground state of the system because it works better for the spin-polarized systems.

The results for the intermediate confinement are displayed in Fig. 34(b). This confinement corresponds to the three-electrode QD of Tarucha et al. [7]. The agreement between the HF and exact results is much better than in Fig. 34(a). Because of the higher accuracy of the HF method for the high-spin states, the critical magnetic fields for the phase transitions into these states are underestimated. However, in the intermediate-confinement regime, the HF results are in a qualitative agreement with the exact results [116].

For the strong confinement (Fig. 34[c]), a fairly good quantitative agreement of the HF and exact results was obtained [116]. The reliability of the HF method for the strongly confined electron systems results from the smallness of the correlation in the high-density electron systems. The strong confinement occurs in the self-assembled QDs [5].

In the high-magnetic field regime, the HF results are very close to the exact results [cf. Fig. 34(a)–34(c)]. At the sufficiently high magnetic field, the electron system becomes fully spin polarized, that is, it goes over into the MDD phase. It appears that the HF method yields the accurate results for the MDD phase.

The effect of the correlation on the single-electron transport through the real QDs was also studied in Ref. [116]. For this purpose, the CI method was introduced into the self-consistent procedure [86] for solving the Poisson-Schrödinger problem for the vertical three-electrode QD [7]. The charge density of the electrons confined in the QD was still determined by the UHF method, which is justified because the charges outside the QD region perceive the electrostatic field, which stems from the mean charge density of the QD confined electrons. The CI method was applied [116] to the calculation of the ground-state energy of the N-electron system confined in the QD. This approach leads to the increase of the accuracy of the ground-state energy calculations. The improved results [116] are shown in Fig. 35 (for the single-electron transport in the magnetic field) and Fig. 36 (for the stability diagram). Figure 35 shows the magnetic-field dependence of the gate voltage at which the single-electron tunneling occurs. The cusps on the curves in Fig. 35 correspond to the magnetic-field-induced ground-state transformations in the QD-confined N-electron system. The CI results much better reproduce the experimental data [23]. The HF method underestimates the critical magnetic fields for the ground-state transformations. Therefore, in the external magnetic field, the electron–electron correlation considerably affects the single-electron transport because the critical magnetic fields are directly determined by the N-electron ground-state energy, which includes the correlation correction. However, the single-electron transport conditions [Eq. (5)] are determined by the N-electron chemical potential, which is calculated as the difference of the ground-state energies. If these energies are calculated with a comparable accuracy, the errors cancel out and the chemical potential is determined with the sufficient precision. This effect is visible on the stability diagram (Fig. 36). The boundaries of the Coulomb diamonds, calculated by the CI and HF methods, differ only slightly. This explains the very good agreement with experiments obtained in Ref. [86] by the HF method [see Fig. (17)].

We conclude that the electron–electron correlation has a diverse influence on the electronic properties of the electrostatic QDs: it considerably affects the energy spectra and the critical magnetic fields for the ground-state transformations in the external magnetic
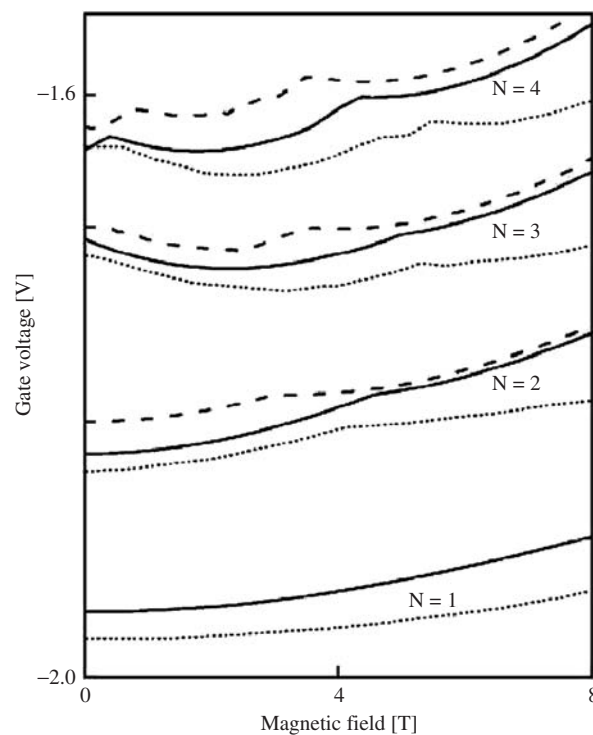
Figure 35. Gate voltage corresponding to the current peaks at very small source-drain voltage as a function of the magnetic field for different numbers N of QD-confined electrons. The solid, dashed, and dotted curves show the CI results, HF results, and experimental data [23], respectively. From Ref. [116].
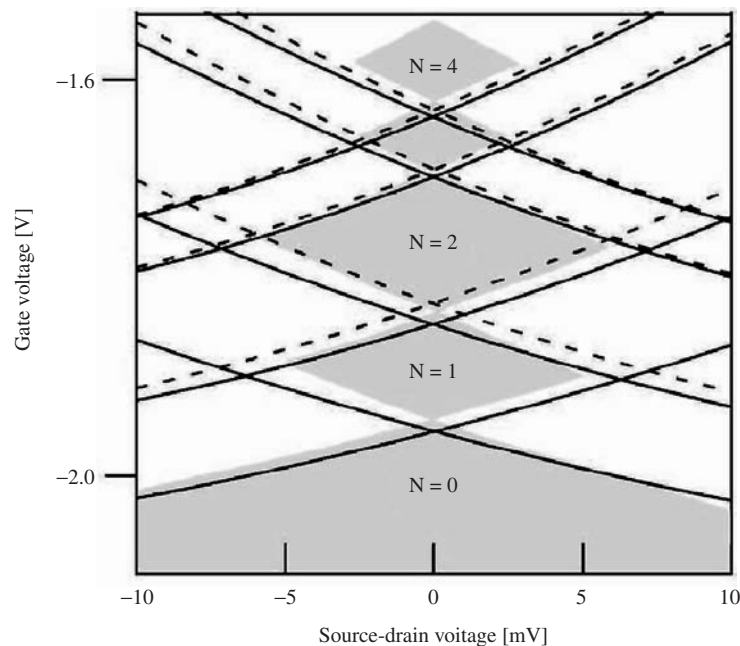
Figure 36. Stability diagram with Coulomb diamonds. Solid (dashed) curves show the boundaries of the Coulomb diamonds calculated by the CI (HF) method. The white and shaded areas correspond to the experimental data [23]. From Ref. [116].

field but only slightly modifies the single-electron transport observed in a function of the source-drain voltage.

9. WIGNER MOLECULES

9.1. Wigner Localization

For sufficiently low density, the electrons can form *Wigner phases* with spatially ordered structures. The Wigner phases comprise the *Wigner crystals* (in many-electron systems) and *Wigner molecules* (in few-electron systems). A formation of the crystalline phase from the low-density electron liquid was theoretically predicted by Wigner [118]. In the 2D space (e.g., on the surface of liquid helium [119]), the Wigner crystal with a triangular (hexagonal) lattice is created. The Wigner molecules can be created in the low-density electron system confined in the QD [104, 120, 121]. The Wigner molecule, also called the *electronic molecule* [8], is a strongly correlated phase of the QD-confined electron system in which the electrons are localized at separate centers forming an island-like, spatially ordered structure. It is interesting that the quantum electron system in the Wigner phase exhibits the quasi-classical properties. In particular, the spatial ordering of the electrons correspond to that in the classical systems of point [111] or spread-out [122] charges. An application of an external magnetic field yields more favorable circumstances for the creation of the Wigner molecules [8, 121, 123–125].

The magnetic field applied to the QD induces several ground-state transformations [98, 124] connected with the rapid changes of the spin-orbital configurations and the symmetry of the electron-density distribution. If the magnetic field is sufficiently strong, the electron system becomes fully spin polarized. In the cylindrical QD, the electrons occupy the subsequent angular-momentum one-particle orbitals forming the MDD [103, 124, 126, 127]. In the MDD phase, the electron-density distribution possesses the cylindrical symmetry (i.e., the same symmetry as the confinement potential). If the magnetic field increases further, the MDD phase decays into the Wigner molecule. In the Wigner-molecule phase, the electron-density distribution, determined as a function of relative electron–electron coordinates, exhibits the island-like structure with the electrons localized around separate spatial sites. Therefore, in the relative coordinates, the confinement-potential symmetry of the

MDD breaks down with the subsequent formation of the Wigner molecule. In the very high magnetic-field regime, that is, at the magnetic field exceeding that corresponding to the MDD decay, phase transitions were predicted [124] between different phases (isomers) of the Wigner molecule. The high-field experimental results [23] clearly demonstrate the MDD decay and indicate on the possibility of the phase transitions in the Wigner-molecule regime. We present a theory of Wigner molecules based on Refs. [124, 128–130].

9.2. Circular Quantum Dots

We consider N electrons confined in a 2D parabolic QD subject to the magnetic field $\mathbf{B} = (0, 0, B)$. If the spin polarization of the N-electron system is complete, the N-electron Hamiltonian has the form

$$H = \sum_{i=1}^{N} \left(h(\mathbf{r}_i) + \sum_{j>i}^{N} \frac{\kappa}{\varepsilon_s r_{ij}} \right) - \frac{N}{2} g^* \mu_B B, \tag{33}$$

where the one-electron Hamiltonian is given by

$$h(\mathbf{r}) = \frac{1}{2m_e} (-i\hbar \nabla + e\mathbf{A})^2 + U_{\mathrm{conf}}(\mathbf{r}). \tag{34}$$

In Eq. (33), $\mathbf{r} = (x, y)$, and the last term is the Zeeman energy of N spin-polarized electrons. The confinement potential is assumed in the parabolic form, given by Eq. (32). The calculations [124, 128–130] were performed in the Landau gauge, that is, for $\mathbf{A} = (-By, 0, 0)$, with the GaAs material parameters.

It is convenient to apply the multicenter Gaussian basis [124, 129, 131, 132] to a description of the Wigner molecules. The multicenter basis can be applied when using both the HF [124, 128, 129] and CI [130] methods. In this basis, the one-electron wave function for state ν is expanded as follows [124, 128–130]:

$$\Psi_\nu(\mathbf{r}) = \sum_{i=1}^{M} c_i^\nu \psi_{\mathbf{R}_i}(\mathbf{r}), \tag{35}$$

where one-electron wave function

$$\psi_{\mathbf{R}}(\mathbf{r}) = \left(\frac{\alpha}{2\pi} \right)^{1/2} \exp\left[-\frac{\alpha}{4}(\mathbf{r} - \mathbf{R})^2 + \frac{i\beta}{2}(x - X)(y + Y) \right] \tag{36}$$

corresponds to the Gaussian electron-density distribution centered at point $\mathbf{R} = (X, Y)$. In Eq. (35), M is the number of centers, taken as $M = N$ in the HF method [124, 128, 129] and $M > N$ in the CI method [130]. In the HF method applied in Refs. [124, 128, 129], it was not required that the wave functions reproduce the symmetry of the external potential. In Eq. (36), α and β are the nonlinear variational parameters. For

$$\alpha = \beta = \frac{m_e \omega_c}{\hbar}, \tag{37}$$

function (36) is the eigenfunction of the lowest Landau level with energy

$$E_0^L = \frac{1}{2} \hbar \omega_c, \tag{38}$$

where $\omega_c = eB/m_e$ is the cyclotron frequency. However, if we substitute

$$\alpha = \frac{2m_e \Omega}{\hbar}, \tag{39}$$

where

$$\Omega = \sqrt{\omega_0^2 + \frac{\omega_c^2}{4}}, \tag{40}$$

and β given by Eq. (37), function (36) is the eigenfunction of the Fock-Darwin ground state, which is the lowest-energy eigenstate of the electron in the magnetic field and the parabolic confinement potential centered at point **R**. The energy of this state is given by

$$E_0^{\text{FD}} = \hbar\Omega. \tag{41}$$

In calculations [124, 128–130], position vectors $\mathbf{R}_i$ in Eq. (35) were treated as variational parameters and the total energy of the N-electron system was optimized with respect to $\mathbf{R}_i$. In the HF method [124, 128], for which $M = N$, position vectors $\mathbf{R}_i$ were taken on as scaled positions of the classical Wigner molecule, that is, the system of classical point charges in the parabolic confinement potential with confinement frequency Ω. In this case,

$$\mathbf{R}_i = \sigma \mathbf{R}_i^{\text{class}}, \tag{42}$$

where $\mathbf{R}_i^{\text{class}}$ are the equilibrium positions of the classical point charges and scaling parameter σ is the third nonlinear variational parameter. The calculations in Ref. [130] were performed by the CI method with $M = 3N$ and $4N$. In this approach [130], more flexibility was allowed on the choice of position vectors $\mathbf{R}_i^{\text{class}}$.

In the study of the qualitative properties of the Wigner molecules, the HF approach with $M = N$ and $\alpha = \beta$ provides reliable results [124, 128]. A certain improvement of the results was obtained with $\alpha \neq \beta$ [129]. To distinguish different spatial configurations (isomers) of the Wigner molecules, it appears to be useful to apply the classical notation [111]. This notation [111] determines the spatial configuration of the classical point charge system, which corresponds to either the global or local minimum of the potential energy. Accordingly, we denote the different isomers of the Wigner molecule by $N_1 - N_2 - N_3$ i.e., where N_1, N_2, and N_3 are the numbers of electrons, which occupy the inner, middle, and outer shells, respectively, whereby $N_1 + N_2 + N_3 = N$. If only two shells are occupied, we label the corresponding isomer by $N_1 - N_2$ and omit zero for the unoccupied outermost shell.

Figure 37 shows the ground-state energy and the electron-density distribution for the six-electron Wigner molecule. It is seen that the MDD phase is stable for the magnetic fields $B < 5$ T, at $B \simeq 5$ T the MDD decays, and the Wigner molecule is formed in the form of isomer
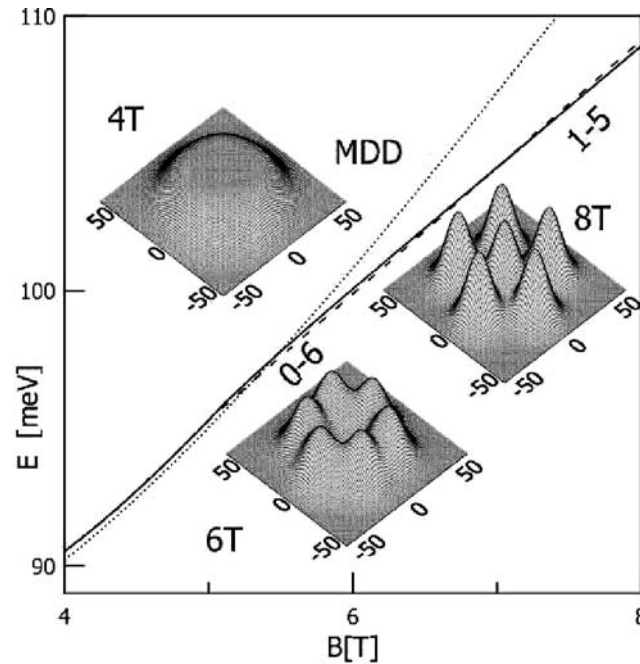
Figure 37. Ground-state energy E of the six-electron MDD (dotted curve) and Wigner-molecule isomers 0–6 (solid curve) and 1–5 (dashed curve) as functions of magnetic field B. Insets: Electron density on the x–y plane for these phases (length in nm). From Ref. [128].
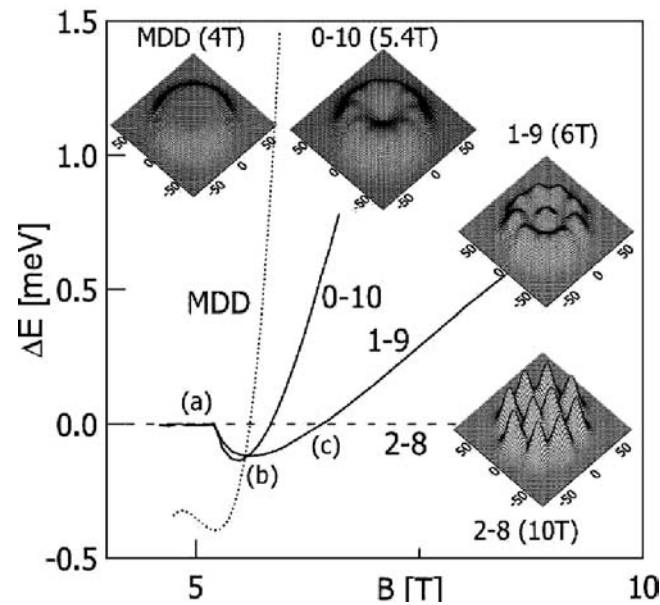
Figure 38. Energy difference ΔE between the ground-state energies of the different 10-electron phases and the ground-state energy of high-field Wigner-molecule phase 2–8 (dashed horizontal line) as a function of magnetic field B. The dotted curve depicts the results for the MDD. Insets: Electron density distribution on the x–y plane (length in nm). From Ref. [128].

0–6. At $B \simeq 7$ T, the Wigner molecule undergoes the phase transition, after which isomer 1–5 becomes most stable. The results for the 10-electron system are depicted in Fig. 38. The decay of the 10-electron MDD leads to the formation of the 0–10 Wigner-molecule isomer. In the increasing magnetic field, this isomer transforms into the 1–9 isomer, which, in turn, goes over into high-field isomer 2–8.

Figure 39 shows the phase diagram for the Wigner molecules with $N = 2, \ldots, 20$ electrons obtained with basis wave functions (36) with $\alpha \neq \beta$. According to the phase diagram (Fig. 39),
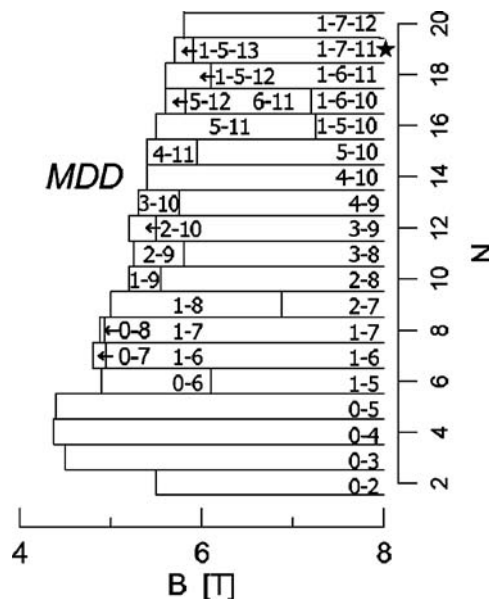
Figure 39. Phase diagram for N-electron Wigner molecules. The lowest-energy isomers are shown as a function of magnetic field B and number N of QD confined electrons. The MDD stability region is located at the left part of the plot. The star indicates that for $N = 19$ the 1–6–12 isomer is created at $B = 15.8$ T. The results plotted have been obtained with variational parameters $\alpha \neq \beta$ in wave function (36), which resulted in some modification of the phase diagram obtained with $\alpha = \beta$ (see Fig. 5 in Ref. [124]).
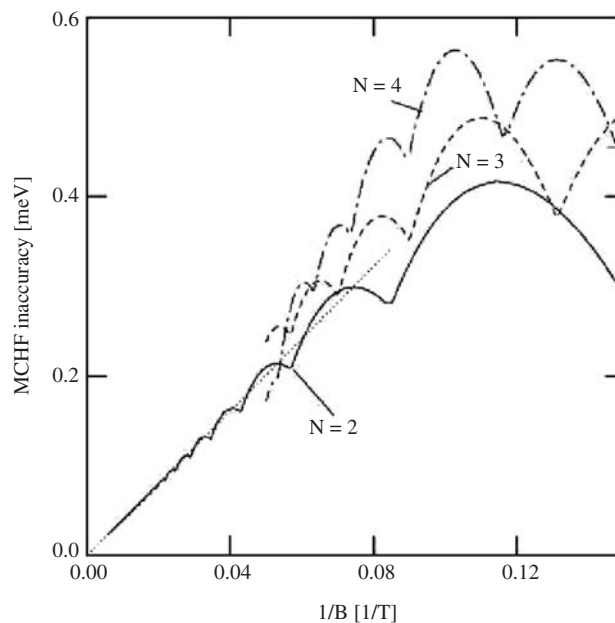
Figure 40. Inaccuracy of the Hartree-Fock method for the ground-state energy of the systems with $N = 2$ (solid curve), 3 (dashed curve), and 4 (dash-dotted curve) electrons as a function of $1/B$, where B is the magnetic field. The dotted line shows the high-field asymptote for $N = 2$, parameterized as $4.028/B$ [meV/T]. Reprinted with permission from [129], B. Szafran et al., *Eur. Phys. J. D* 28, 373 (2004). © 2004, EDP Sciences.

the Wigner molecule with $N \geq 6$ electrons can exist in more than one phase. The phase transitions [124, 128] exhibit a certain regularity. In the first isomer formed after the decay of the MDD, the electrons prefer to occupy the outer shells. In the next isomers created at higher magnetic fields, the increasing number of electrons starts to occupy the middle and inner shells. The spatial configuration of the N-electron Wigner-molecule isomer, formed at the extremely high magnetic field, is the same as the equilibrium configuration of N equally charged classical particles. At the finite magnetic field, the average interelectron separations are different in the quantum and classical systems [128]. However, in the limit of the infinite magnetic field, the average electron–electron separations in the quantum Wigner molecule become equal to those in the classical point-charge system [128]. Therefore, when applying the external magnetic field to the electron system confined in the QD, we can observe a continuous transition from the quantum to classical behavior. In the same limit (i.e., $B \rightarrow \infty$), the HF method becomes exact. The HF inaccuracy is plotted in Fig. 40 versus $1/B$ for $N = 2$, 3, and 4. We see that the HF inaccuracy for $N = 2$ is proportional to $1/B$, and the results for $N = 3$ and 4 exhibit a similar tendency.

In the literature, two different mechanisms of the MDD decay were proposed [126, 127, 133]. According to Reimann et al. [126, 127], the MDD starts to decay at the edge of the droplet. In this process, called the *edge reconstruction*, a ring of electrons separates out from a flat density maximum [126, 127]. However, Yang and MacDonald [133] argued that the MDD breaks down when a hole appears in the electron- density at the center of the QD. Both these mechanisms are visualized in Figs. 38 and 41. Inset of Fig. 38 clearly shows the hole in the electron-density distribution of the isomer 0–10 formed after the MDD breakdown. The results of Fig. 41 for $B = 6$ T correspond to the edge reconstruction. These results [128] lead to a conclusion that both the mechanisms can be effective if the MDD breaks down. We suggested [128] that for the electron systems with $N \leq 12$ the central-hole formation mechanism is preferred, while for $N > 12$, the MDD begins to decay from the edge.

The physics behind the MDD decay and the creation of the Wigner molecule can be well illustrated by considering the electron–electron interaction as a function of the magnetic field. Figure 42 displays the expectation value of the interaction energy among all the electrons in the six-electron system. In Fig. 42, the sharp, pronounced peak of the interelectron interaction energy as a function of external magnetic field corresponds to the MDD-Wigner
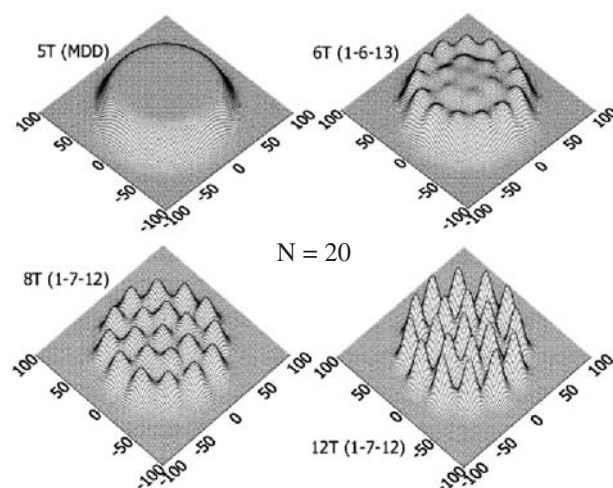
Figure 41. Electron-density distribution on the x–y plane for $N = 20$ electrons for several magnetic fields. Length is measured in nanometers. From Ref. [128].

molecule phase transition. In the MDD magnetic-field regime, that is, at the magnetic fields below the peak position, the electron–electron interaction rapidly increases with the increasing magnetic field, which results from the quickly decreasing interelectron distances due to the squeezing of the electron system by the high magnetic field. At a certain magnetic field, the electron–electron repulsion becomes so strong that the MDD breaks down. Then, the MDD charge distribution, which is almost uniform over a wide spatial range, goes over into the island-like molecular-type distribution, which minimizes the total energy. In the molecular phase, the electron-electron interaction energy rapidly falls down for the magnetic fields
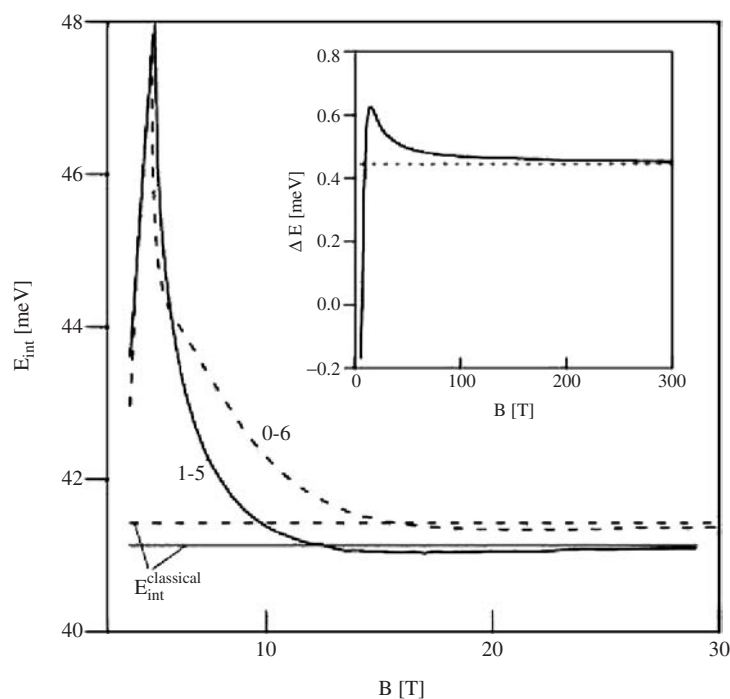
Figure 42. Expectation value E_{int} of the electron-electron interaction energy in the six-electron system confined in the 2D parabolic QD as a function of magnetic field B. Solid (dashed) curve displays the results obtained with wave function (35) corresponding to configuration 1–5 (0–6). The corresponding classical electron–electron interaction energy $E_{int}^{classical}$ is represented by the horizontal lines. Inset: Energy difference ΔE between the ground-state energies of isomers 0–6 and 1–5. The horizontal dashed line displays this energy difference for the classical Wigner molecule. From Ref. [128].

just above the MDD decay and quickly becomes a slowly varying function of B, which asymptotically reaches the high-field value. The position of the peak of the interaction energy (Fig. 42) can be used to determine the critical magnetic field for the decay of the MDD [128]. In the high-field limit, the quantum mechanical expectation value of the interelectron interaction energy tends to the corresponding classical interaction energy (see Fig. 42).

The classical behavior of the Wigner molecules at the extremely high magnetic fields is also demonstrated in the inset of Fig. 42, which displays the difference ΔE of the energies of the 1–5 and 0–6 isomers. It is seen that ΔE asymptotically reaches the corresponding classical value marked by the horizontal dashed line.

The MDD decay and the formation of different isomers of the Wigner molecule result from the competition between the electron–electron repulsion, the exchange interaction, and the magnetic-field influence. The estimation of the first two effects is shown in Fig. 43 [128]. The expectation value of the electron–electron interaction energy is equal to Hartree energy $\langle V_C \rangle$ of the interaction between the two Gaussian electron charge densities. In contrast to the Coulomb repulsion, the Hartree energy is nonsingular at zero interelectron distance. At intermediate interelectron distances the Hartree repulsion is stronger than the Coulomb repulsion and approaches the Coulomb interaction between the two classical point charges when $R \rightarrow \infty$. The exchange interaction rapidly falls down to zero and vanishes for large R. Therefore, at large distances, the two electrons interact as the classical point charges. For higher magnetic fields, the effective electron–electron interaction becomes classical for smaller interelectron separations [128]. This confirms the quasi-classical behavior of the Wigner molecules at extremely high magnetic fields [128].

Let us discuss the problem of symmetry breaking in Wigner molecules. The electron system confined in the circular QD should possess the rotational symmetry because it is subject to the confinement potential and magnetic field, both of which possess the same circular symmetry. Therefore, the ground state of the Wigner molecule is infinitely-fold degenerate with respect to the rotations around the z-axis. By rotating the molecular charge density distribution by an arbitrary angle in the x–y plane, we obtain the equivalent configuration with the same energy. Therefore, the ground state of the Wigner molecule should be associated with the rotationally invariant charge density distribution, which can be constructed from the superposition of the rotated broken-symmetry states. This means that the plots of the spatial charge density distributions, depicted in Figs. 37, 38, and 41 should be understood as the pictures drawn in a function of the relative electron–electron coordinates.
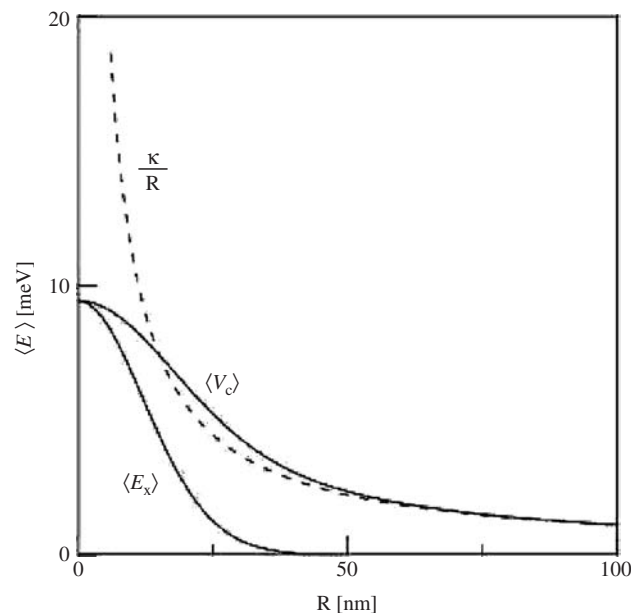
Figure 43. Expectation values of the Hartree energy $\langle V_C \rangle$ and exchange energy $\langle E_X \rangle$ as functions of interelectron distance R. The dashed curve shows the Coulomb potential energy. From Ref. [128].

9.3. Anisotropic Quantum Dots

The real QDs rarely possess the perfect cylindrical symmetry. In most nanostructures, some anisotropy is inevitable. The small anisotropy of the confinement potential can result from the presence of impurities in the neighborhood of the QD region. The fabrication process of the nanostructure can also lead to the anisotropy. Moreover, the anisotropic QDs are intentionally created [54]. In the theory of QDs, the influence of the small anisotropy can be taken into account as a small perturbation of the confinement potential [84]. The anisotropy should stabilize the broken-symmetry Wigner-molecule configurations under the fixed spatial orientation [124].

An extensive and detailed study of the Wigner molecules in the anisotropic QDs was performed in Ref. [130]. For this purpose, multicenter Gaussian basis (35) was applied. The calculations [130] were performed with the use of the multicenter CI method, which provides exact results for few-electron systems. Here, we discuss the results for the elliptical QDs with the confinement potential

$$U_{\text{conf}}(x, y) = \frac{m_e}{2}(\omega_x^2 x^2 + \omega_y^2 y^2), \tag{43}$$

where ω_x and ω_y are the confining frequencies in the x and y directions, respectively, and $\omega_y > \omega_x$. The charge densities calculated in Ref. [130] are shown in Fig. 44 for the two-, three-, and four-electron systems. In the lowest panel, the equilibrium configurations of the classical point charge systems are depicted. For $N = 3$, the two equivalent classical configurations exhibit the classical degeneracy. Figure 44 demonstrates the formation of the Wigner molecules for $N = 2$ and 4 at the sufficiently large magnetic field. If the magnetic field increases, the spatial distribution of the electrons tends to the corresponding classical configuration. The classical degeneracy of the three-particle system is closely related with the more complex charge density distribution of the three-electron system [130]. This distribution is displayed more clearly in Fig. 45. The results of Figs. 44 and 45 [130] show that at the high magnetic field the charge density distribution for the three-electron system approaches the linear combination of the charge distributions of the two degenerate classical configurations.

In the strongly anisotropic QDs, the formation of the zigzag and linear Wigner molecules was predicted [130] (see Fig. 46). The superposition of the two equivalent spatial configurations for $\hbar\omega_y = 5.5$ meV is connected with the classical degeneracy, which is depicted in the right panel. In this case, the separation of the electrons is not complete, and we deal with a partial Wigner crystallization [130].

9.4. Exact Broken-Symmetry Solutions

For certain thoroughly chosen magnetic fields, a single classical configuration can be realized even in the three-particle system [130]. This configuration can be obtained from the exact solutions, which possess the rotational symmetry, by constructing the following broken-symmetry wave function:

$$\psi_{\text{BS}} = \frac{1}{\sqrt{2}}(\chi_1 + e^{i\theta}\chi_2), \tag{44}$$

where χ_1 and χ_2 are the degenerate few-electron states with the definite symmetry, which are associated with the lowest-energy levels, and θ is a real number representing a relative phase. Although the electron charge densities associated with solutions χ_1 and χ_2 possess the rotational symmetry of the external potential, the charge density obtained with wave function (44) with the properly chosen relative phase does not reproduce this symmetry. As a result, the exact state with the broken symmetry was obtained [130]. The charge density for this exact broken-symmetry state is plotted in Fig. 47. For the chosen phase θ and for the strictly defined values of the magnetic field, the exact three-electron charge density possesses the three distinct maxima, which coincide with the positions of the classical point charges in one of the degenerate classical configurations (see the bottom panel in Fig. 44). If the magnetic field increases, the broken-symmetry charge density distribution converges toward one of the degenerate configurations of the classical point charges.
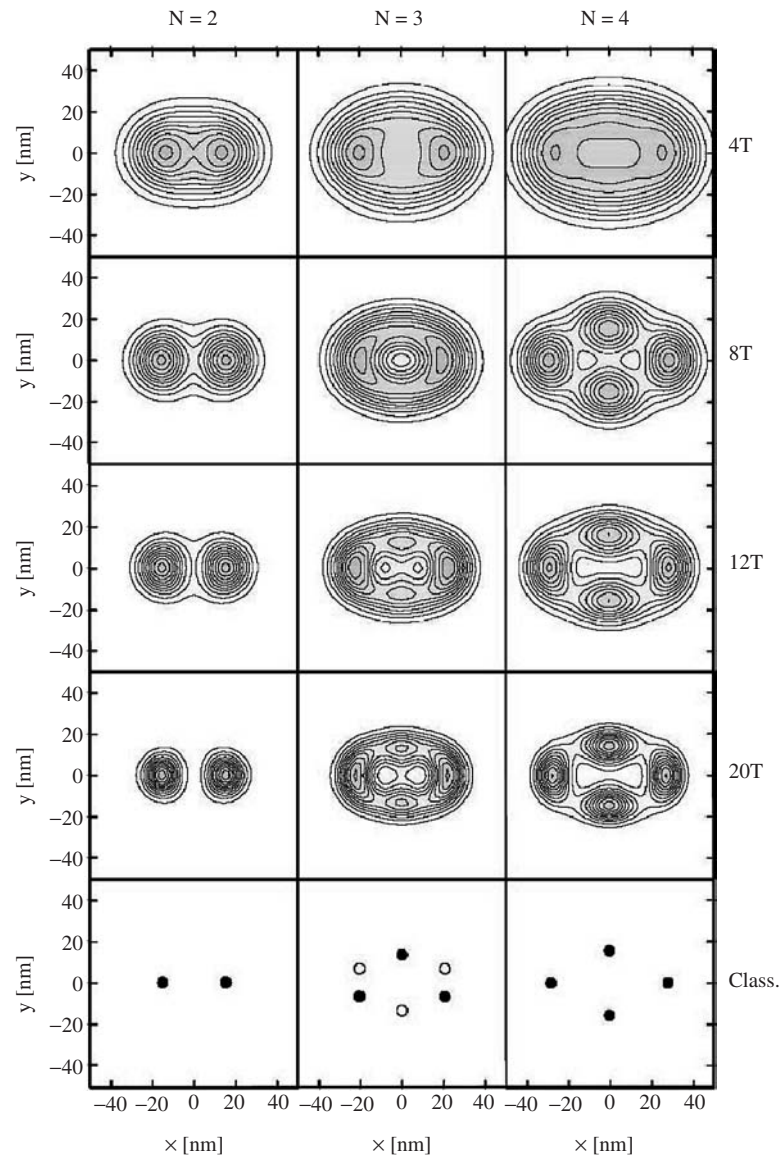
Figure 44. Charge density of two-, three-, and four-electron systems confined in the anisotropic parabolic potential with $\hbar\omega_x = 3$ meV and $\hbar\omega_y = 4$ meV for different magnetic fields. The lowest panel shows the equilibrium configurations of the corresponding classical point charge systems. For $N = 3$ the two degenerate configurations are marked with full and open dots. From Ref. [130].
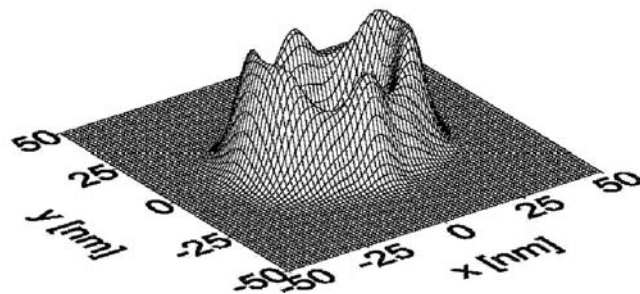
Figure 45. Charge density of three-electron system confined in the anisotropic parabolic potential with $\hbar\omega_x = 3$ meV and $\hbar\omega_y = 4$ meV at $B = 30$ T. From Ref. [130].
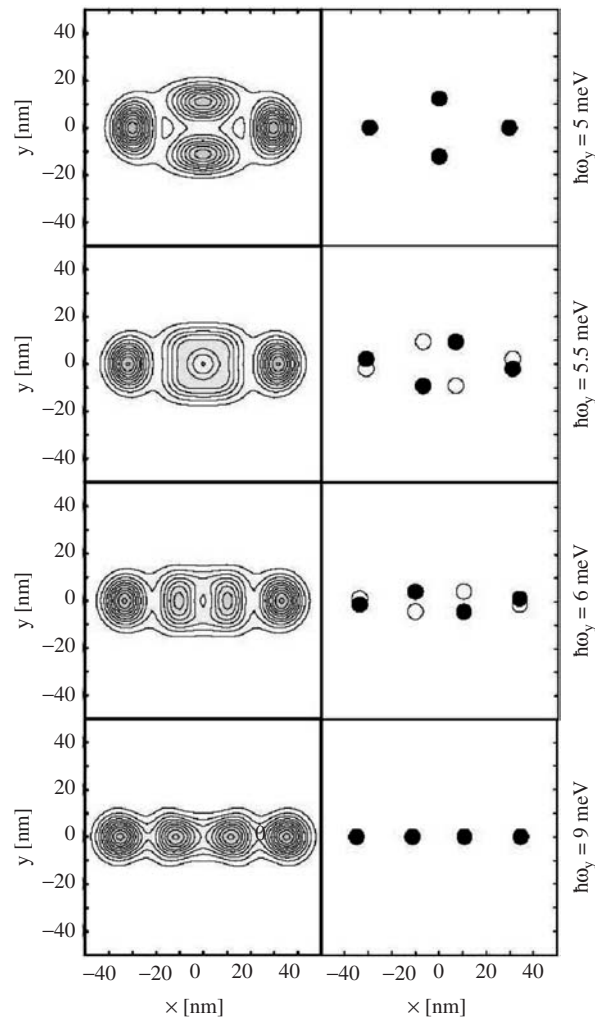
Figure 46. Left panel: Charge density of four-electron system confined in the anisotropic parabolic potential for $\hbar\omega_x = 3$ meV and different values of $\hbar\omega_y$ at $B = 20$ T. Right panel: Lowest-energy configurations of the corresponding classical point-charge system. For $\hbar\omega_y = 5.5$ meV and 6 meV the two degenerate configurations are marked with full and open dots. From Ref. [130].

Having at our disposal the exact broken-symmetry wave functions (44), we went back to the isotropic (circular) QDs and performed the calculations with great care [130]. The solutions [130] with the broken symmetry provide the lowest energy for the magnetic fields that induce the ground-state angular momentum transitions. The results for the broken-symmetry charge density are presented in Fig. 48 for three electrons and Fig. 49 for four electrons.

The symmetry breakdown, obtained in the exact calculations [130], can be observed in the laboratory frame, that is, this effect should be accessible by the high-finesse experimental techniques [134]. The external perturbation (e.g., in the form of the Coulomb potential of the charged impurity center), indicates that instead of the single-valued magnetic fields at which the breakdown of the symmetry occurs we deal with the finite intervals of the magnetic field in which the broken-symmetry charge density distributions are predicted [135].

The spatial density distributions of electrons obtained in Ref. [130] for the anisotropic QDs is interpreted in terms of the laboratory-frame coordinates. Therefore, the calculated island-like electron distributions directly correspond to the real-space distributions of the electrons, which can be observed (e.g., in the wave function imaging experiments [134]).
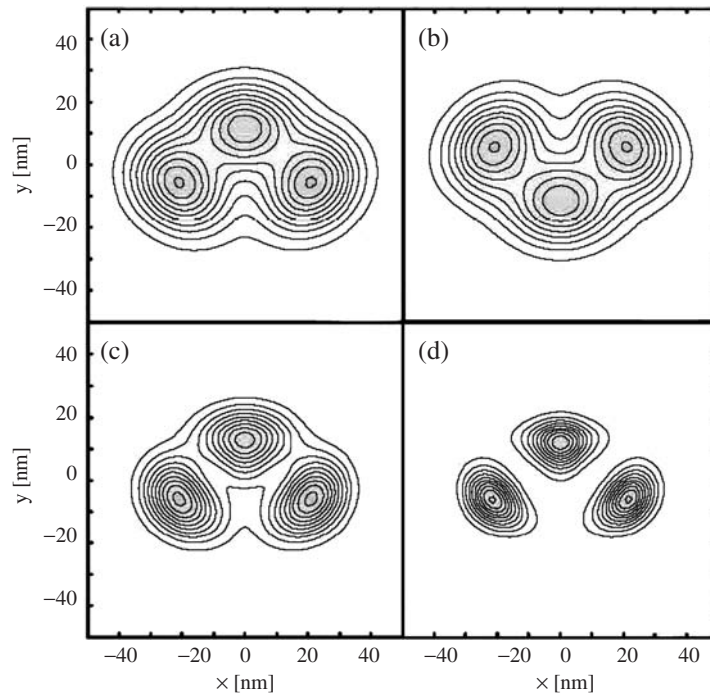
Figure 47. Charge density of the exact broken-symmetry three-electron states in the anisotropic parabolic potential with $\hbar\omega_x = 3$ meV and $\hbar\omega_y = 4$ meV for $B = 6.3$ T (a, b), 14.125 T (c), and 25 T (d). From Ref. [130].

10. ARTIFICIAL MOLECULES

The three-terminal nanodevice fabricated from the triple-barrier structure [17] contains the two vertically coupled QDs separated by a barrier layer. The electrons confined in the coupled QDs can form molecular-like states, called the *artificial molecules*. These molecular
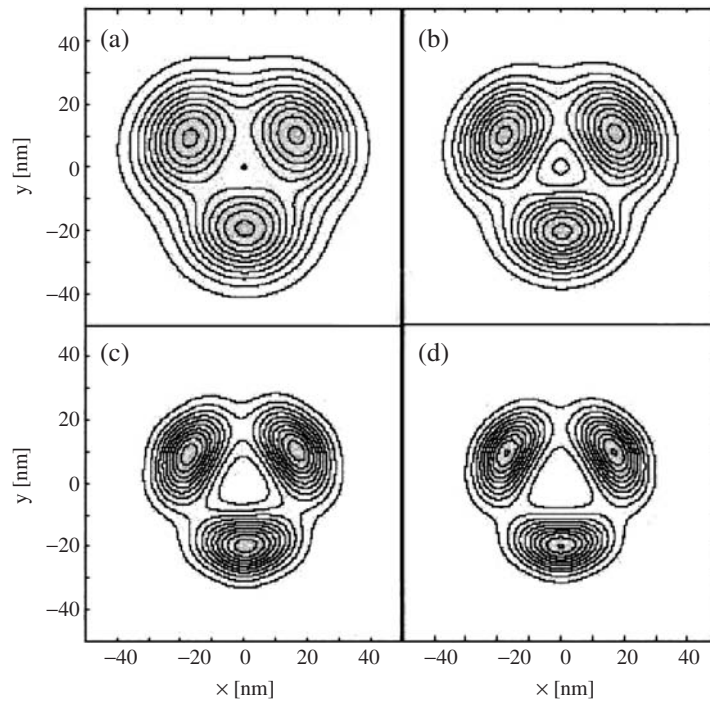
Figure 48. Charge density of the exact broken-symmetry three-electron states in the isotropic parabolic potential with $\hbar\omega = 3$ meV. Plots (a–d) are drawn for $B = 4.9$, 7.5, 15, and 18.4 T, respectively. From Ref. [130].
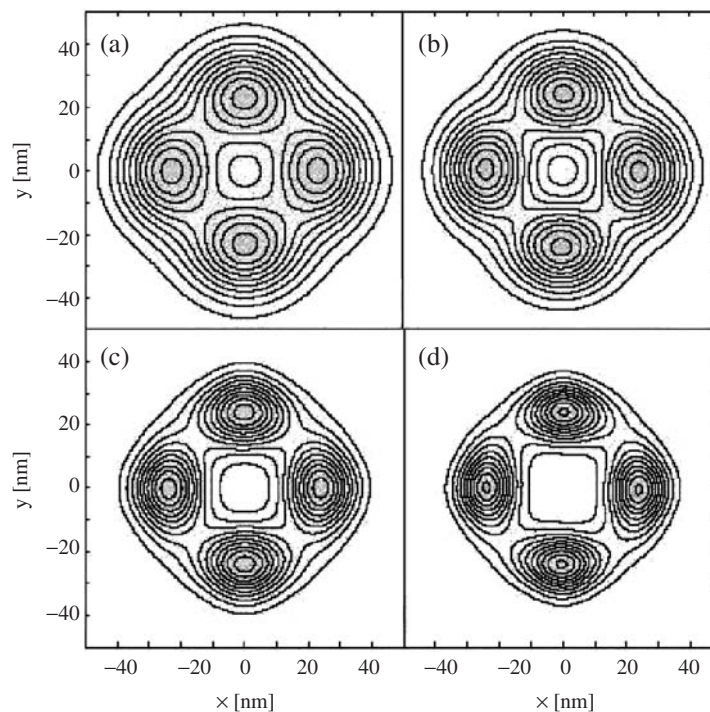
Figure 49. Charge density of the exact broken-symmetry four-electron states in the isotropic parabolic potential with $\hbar\omega = 3$ meV. Plots (a–d) are drawn for $B = 4.75, 6.5, 11.5,$ and 16 T, respectively. From Ref. [130].

states were studied by the transport spectroscopy [17]. For the thin barrier separating the QDs [17], the stability diagram with the Coulomb diamonds, observed for the single QD [7], is only slightly deformed. However, for the sufficiently thick barrier, the Coulomb diamonds were deformed and a pairing of conductance peaks was found [17]. Also the magnetic-field evolution of the conductance peaks is strongly modified [117]. These effects were interpreted in terms of the formation of the artificial molecules [117, 136].

A theory of artificial molecules deals with few-particle problems for which exact solutions are hardly accessible even for simple parabolic confinement potentials [117]. This hard task was undertaken by the group of Elisa Molinari and Massimo Rontani from the University of Modena (Italy), who calculated excitation spectra of vertically coupled QDs by the CI method [117]. We proposed the approach [114], which reduces the original 3D problem to the effective, exactly solvable one-dimensional (1D) model. This model works quite well for both the vertically coupled QDs and the quasi-1D nanostructures (e.g., quantum wires). Here, we present a brief outline of the theoretical model [114, 137] and the main results obtained for the coupled QDs.

In the cylindrical QD, the confinement potential U_{conf} can be expressed as a sum of lateral $U_\perp$ and vertical $U_\parallel$ confinement potentials, that is,

$$U_{\text{conf}}(x, y, z) = U_\perp(x, y) + U_\parallel(z). \tag{45}$$

The lateral confinement potential is assumed to be in the parabolic form, that is,

$$U_\perp(x, y) = \frac{m_e \omega_\perp^2}{2}(x^2 + y^2), \tag{46}$$

where $\omega_\perp$ is the lateral confinement frequency. For the separable potential given by Eq. (45) the one-particle wave function has the product form

$$\psi(x, y, z) = \psi_\perp(x, y)\psi_\parallel(z). \tag{47}$$

The ground-state wave function, which describes the lateral motion, has the form

$$\psi_\perp(x, y) = (\pi^{1/2}l)^{-1}\exp[-(x^2 + y^2)/(2l^2)], \tag{48}$$

where $l = (\hbar/m_e\omega_\perp)^{1/2}$.

The problem of two electrons confined in potential (45) and interacting via the Coulomb field cannot be strictly separated in the lateral and vertical coordinates like in Eq. (47). This difficulty results from the intrinsic inseparability of the two-particle Coulomb interaction potential. If, however, the lateral-motion ground-state wave function dominates in the expansion of the two-electron wave function into the one-electron wave function, that is, the excited lateral-motion one-electron states can be neglected, the two-electron ground-state wave function can be taken on in the following separated form:

$$\Psi(\mathbf{r}_1, \mathbf{r}_2) = \psi_\perp(x_1, y_1)\psi_\perp(x_2, y_2)\Phi(z_1, z_2). \tag{49}$$

The approximate separation [Eq. (49)] is valid if the lateral excitation energy $\hbar\omega_\perp$ is much greater than the electron–electron interaction energy. Moreover, independently of the confinement strength, separation (49) is possible for the electrons in the two coupled QDs if both the QD confinement potentials possess the comparable range and potential-well depth. In this case, the lowest-energy levels associated with the electron states localized in each QD are nearly equal to each other, that is, their energy difference is much smaller than the lateral excitation energy $\hbar\omega_\perp$. Therefore, the condition of separability (49) is satisfied. Separated form (49) of the two-electron wave function allows us to derive the 1D effective electron–electron interaction, given by [114, 137]:

$$V_{\text{eff}}(z) = \frac{\pi^{1/2}\kappa e^2}{\varepsilon a}\exp(\zeta^2)\text{erfc}(\zeta), \tag{50}$$

where $a = 2^{1/2}l = (2\hbar/m_e\omega_\perp)^{1/2}$, ε is the relative electric permittivity, $\zeta = |z|/a$, and $\text{erfc}(\zeta)$ is the complementary error function.

Effective interaction (50) can be applied to the following physical systems: (1) quasi-1D QDs, which are formed in a section of a quantum wire [138], (2) vertically coupled double QDs with the comparable sizes and potential-well depths [17], (3) weakly coupled QDs with arbitrary confinement potentials.

Potential energy (50) of the effective electron–electron interaction is plotted in Fig. 50 and compared with the Coulomb interaction potential and model potentials [139, 140]. Effective interaction (50) is weaker than the Coulomb interaction for all interelectron distances z. For $z = 0$ the effective interaction potential is finite and possesses a cusp, and for $z \to \infty$ exhibits the Coulomb asymptotics. The effective interaction depends on the confinement potential as follows: for weaker confinement the effective interaction becomes softer at small interelectron distances. Figure 50 also shows that there are the qualitative differences between the effective interaction (50) and model interaction potentials used in the literature [139, 140].

The application of effective interaction (50) considerably simplifies the few-electron problems. For example, in the two-electron problem, the number of independent coordinates is reduced to two. Accordingly, the two-electron Hamiltonian has the form

$$H_{12} = -\frac{\hbar^2}{2m_e}\left(\frac{\partial^2}{\partial z_1^2} + \frac{\partial^2}{\partial z_2^2}\right) + U_\parallel(z_1) + U_\parallel(z_2) + V_{\text{eff}}(|z_1 - z_2|). \tag{51}$$

The eigenproblem for Hamiltonian (51) can be solved by the imaginary-time method [112, 113] with the arbitrary required precision. Therefore, we can treat these numerical solutions as exact. These exact solutions fully take into account the electron–electron correlation. Comparing the exact solutions with the results of the HF methods, we can discuss the effect of correlation in the two-electron systems.

In Ref. [114], we studied the artificial-molecule states that are formed in the two vertically coupled QDs separated by the barrier layer with thickness b. The two lowest energy levels of the two-electron artificial molecule, calculated in Ref. [114] by the exact, RHF and
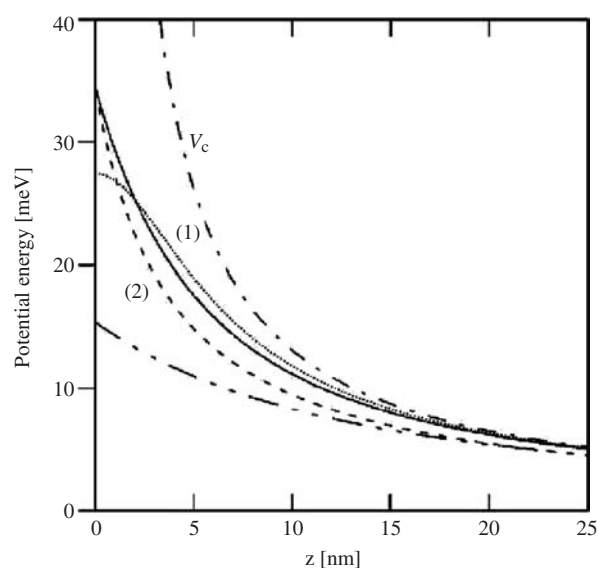
Figure 50. Potential energy of the effective electron-electron interaction for lateral confinement energy $\hbar\omega_\perp = 50$ meV (solid curve) and 10 meV (dash-double-dotted curve) as a function of interelectron vertical distance z. The dashed (dotted) curve corresponds to the model interaction from Ref. [140] ([139]) and dash-dotted curve shows the Coulomb interaction energy $V_C = \kappa/z$. From Ref. [137].

UHF methods are displayed in Fig. 51. When varying b, we change the coupling between the QDs. For small b (i.e., for the strongly coupled QDs), the singlet and triplet states are nondegenerate and the singlet state is the ground state of the artificial molecule. For large b, that is, for the weakly coupled QDs, the singlet and triplet states become degenerate. Figure 51 shows that the exact results are quite well reproduced by the UHF method, while the RHF method considerably underestimates the singlet energy, which leads to the
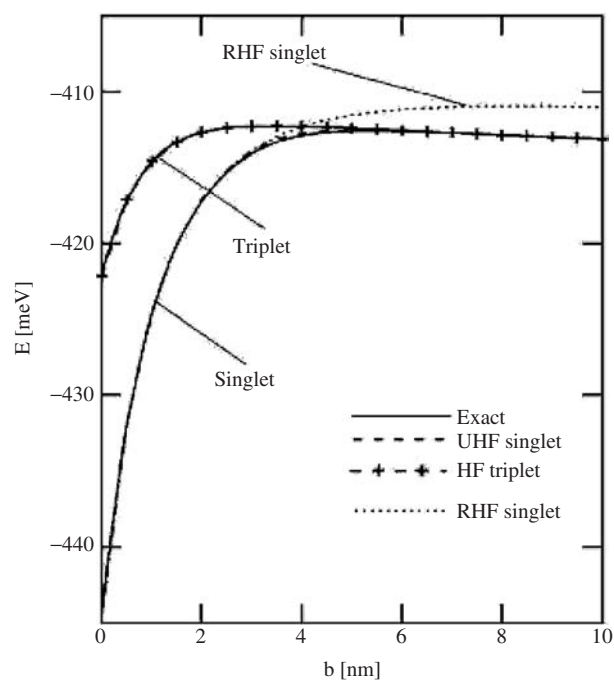
Figure 51. Lowest singlet and triplet energy levels (solid curves) obtained by the exact calculation for the two-electron system confined in the double QD as functions of barrier thickness b. The dashed (dotted) curve shows the UHF (RHF) results for the singlet state. The dashed curve with crosses displays the results of both the UHF and RHF methods for the triplet. From Ref. [114].

qualitatively incorrect energy ordering for large b. For the triplet state, both the UHF and RHF methods yield the results, which are almost indistinguishable from the exact results. Comparing the UHF and RHF energy estimates with the exact results, we obtain a quantitative estimate of the electron–electron correlation in artificial molecules (Fig. 52). The results depicted in Figs. 51 and 52 show that the correlation is negligible for the triplet states, while it becomes important for the singlet states in the weakly coupled QDs. The inaccuracy of the UHF method (see Fig. 52) increases with barrier thickness b for small b, takes on the maximum for $b = 3$ nm, and next decreases for larger b. For $b > 6$ nm, the UHF results are indistinguishable from the exact ones. On the contrary, the RHF inaccuracy monotonically increases with increasing b and becomes larger than 1 meV for $b > 5$ nm.

The results of Figs. 51 and 52 can be summarized as follows: the UHF method partially takes into account the electron–electron correlation, while in the RHF method, the correlation is completely ignored. Therefore, the RHF energy estimates provide suitable reference data for studying the correlation. In the coupled QDs, the correlation increases with the increasing thickness of the barrier, that is, the increasing electron–electron distance.

The contours of two-electron probability density distribution

$$\varrho(z_1, z_2) = |\Phi(z_1, z_2)|^2, \tag{52}$$

plotted in Fig. 53, allow us to get a more deep insight into the physics of artificial molecules. For $b = 0$, we deal with the two-electron artificial atom in which both the electrons occupy the single QD. Introducing the barrier layer with the increasing thickness, we decrease the interdot coupling, that is, increase the electron–electron correlation, which increases the probability of finding the electrons in the different QDs. If the barrier is sufficiently thick, the probability of finding both the electrons in the same QD vanishes, which corresponds to the strong electron–electron correlation. Figure 53 shows that the UHF method quite well reproduces the exact two-electron wave function for the singlet state and that both the UHF and RHF methods work very well for the triplet state.

It is interesting to compare the properties of the artificial molecules with those of the Wigner molecules [114]. The separation of electrons in the double QDs occurs if the repulsive potential of the barrier layer is sufficiently strong and possesses a large enough range. It is possible to induce the separation of the electrons in the single QD only by increasing its size [114]. If the electron system is confined in the single QD of the sufficiently large size,
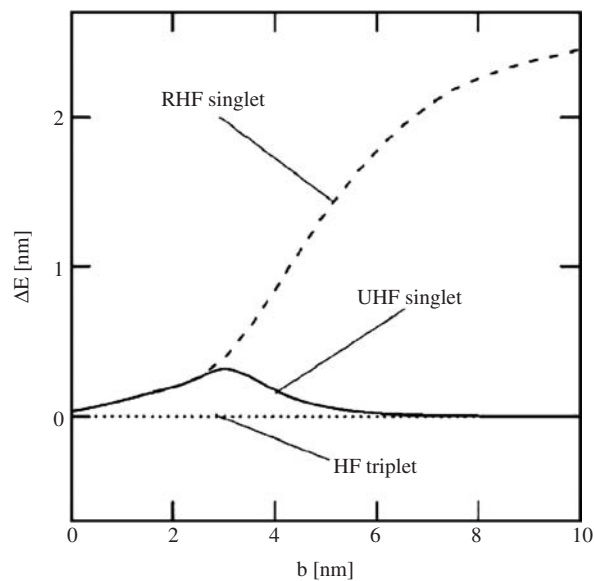
Figure 52. Estimated inaccuracy $\Delta E = |E_{\text{exact}} - E_{\text{UHF(RHF)}}|$ of the UHF (RHF) method plotted by the solid (dashed) curve for the singlet state of two electrons confined in the coupled QDs with barrier thickness b. The inaccuracies for the triplet state of both the HF methods are shown by the dotted curve. From Ref. [114].
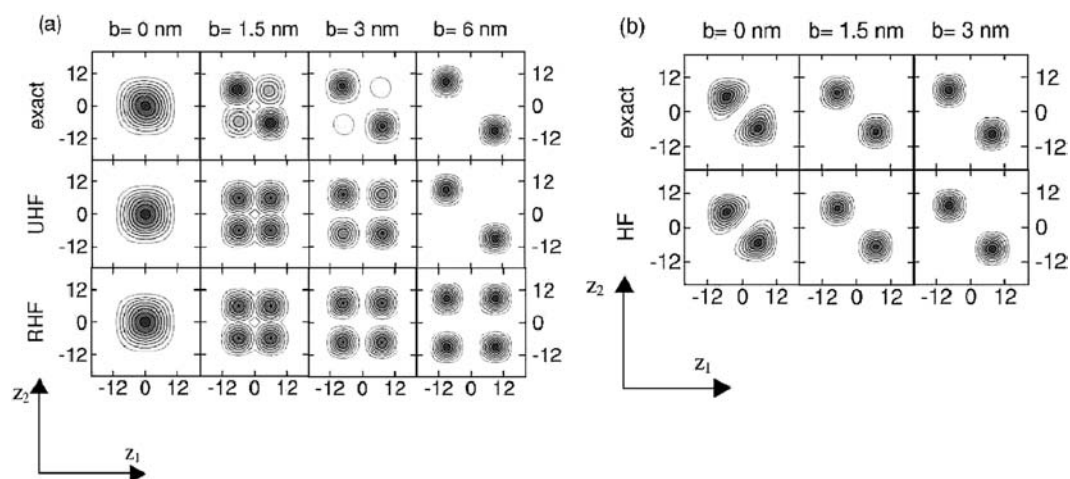
Figure 53. Contours of the two-electron probability density in the coupled QDs as functions of z_1 and z_2 (in nm) for (a) singlet and (b) triplet states for several values of barrier thickness b. The darker the shade of gray, the larger the electron density. The white areas correspond to zero electron density. From Ref. [114].

the Wigner-molecule states can be formed as a result of the size effect [114]. The energy of the two-electron system confined in the QD is depicted in Fig. 54 as a function of the linear size of the QD. Similarly, as in the double QD, the singlet state is the ground state of system and the singlet and triplet energy levels become degenerate if the size of the QD increases. The error of the RHF method is a measure of the correlation energy [114]. We note that the electron–electron correlation increases if the size of the QD increases. This increasing correlation entails the distinct localization of electrons, which is clearly seen for $Z \simeq 100$ nm (Fig. 55). We interpret the results of Fig. 55 in terms of the formation of the Wigner molecule. The Wigner molecules are created in both the singlet and triplet states. Contrary to the magnetic-field-induced creation of the Wigner molecules [124, 128–130], no
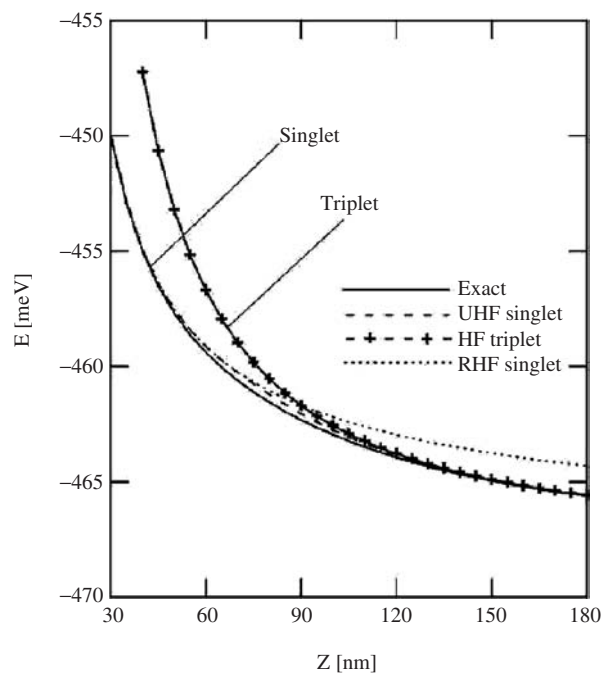
Figure 54. Lowest singlet and triplet energy (solid curves) obtained by the exact calculation for the two-electron system confined in the single QD as a function of linear QD size Z. The dashed (dotted) curve shows the UHF (RHF) results for the singlet state. The dashed curve with crosses displays the results of both the UHF and RHF methods for the triplet. From Ref. [114].
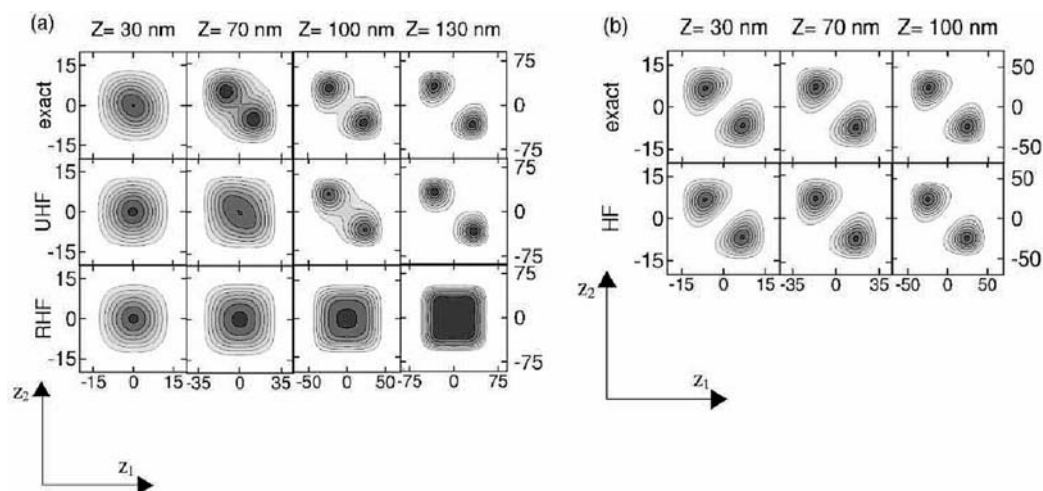
Figure 55. Contours of the two-electron probability density in the single QD as functions of z_1 and z_2 (in nm) for (a) singlet and (b) triplet states for several values of QD size Z. Note the different length scales for different Z. The gray scale as in Fig. 53. From Ref. [114].

external field is necessary to create the Wigner molecules of this type. These species can be called the *size-induced Wigner molecules* [114]. The formation of the size-induced Wigner molecules [114] is caused by the strong electron–electron correlation, which appears in the electron system confined in the QD with the sufficiently large size. Similarly, as in the coupled QDs, the UHF method quite well reproduces the exact results, but the RHF approach does not yield the reliable results. Comparing Fig. 53 with Fig. 55 we observe the remarkable similarity between the electron-density distribution in the artificial molecules, formed in the coupled QDs, and in the Wigner molecules, formed in the single QD. In both cases, we obtain the similar localization of electrons at distinct spatial sites, which results from the strong electron–electron correlation. Therefore, we can regard both the systems as two kinds of the artificial-molecule states with the similar electron localization.

In the coupled QDs, the electron–electron correlation increases with the increasing thickness of the barrier layer separating the two QDs. Therefore, the correlation can be artificially tuned by changing the barrier layer thickness, which is a technologically realizable process. This entails the possibility of changing intentionally the electron–electron correlation from weak (for the thin barrier layer) to strong (for the thick barrier layer). The correlation can also be tuned in the single QD by changing its size. These technological processes offer a new type of quantum engineering, namely, the artificial modification of the electron–electron correlation.

11. DISCUSSION

In a theoretical study of electronic properties of electrostatic QDs, we are faced with a complicated many-body problem. The many-body system we deal with consists of many atomic nuclei, core electrons, and valence electrons. The theory of the QDs is based on the approximations, taken from the theory of bulk solids, which allows us to reduce this many-body problem to the effective many-electron problem in which only the excess electrons confined within the QD play a role. Typically, number N of QD-confined electrons satisfies $N \leq \sim 100$. We can further reduce this number because the most interesting physics and the most promising applications occur for $1 \leq N \leq \sim 20$. Finally, we are dealing with the *few-electron system*. A question of the applicability of these approximations arises. Let us discuss the most important of them.

One problem is connected with the applicability of the band theory, developed for the bulk crystals, to the nanostructures with finite size. Can we use the band theory for the electrons confined in the QD whose spatial extension in each direction is of the order of 10–100 nm? For the electrostatically gated QDs, we can give the positive answer to this question because

the physical QD region of nanometer extension is embedded in a quite large structure with the size of the order of micrometers. The micrometer-sized crystal structure can be described in the framework of the theory for bulk crystal. The electrons are localized within the electrostatically gated vertical QDs by the electrostatic field of the leads and ionized donors and by the band offsets. A lattice mismatch, which is quite large in self-assembled QDs, is small in the electrostatic QDs. Also, the compositional modulation, which is important in InGaAs alloys formed in the self-assembled QDs [141], is negligibly small in the electrostatic QDs. Therefore, in the electrostatic QDs, the strain and alloying effects play a secondary role. The QDs, studied by Ashoori et al. [6] and Tarucha et al. [7], are based on the gallium arsenide. Therefore, we can use the band-structure parameters of GaAs in a modeling of these QDs. The influence of GaAs/AlGaAs interfaces is taken into account by introducing the appropriate band offsets into the confinement potential in the vertical direction.

In the framework of the band theory, we are using the envelope function approximation (effective mass approximation) to describe the conduction band electrons in the QD. This approximation can be derived for the electrons confined in the QD in the same manner as for the shallow-level donor states. In both cases, we are dealing with the weakly localized electrons with small binding energies. In the semiconductor heterostructure, the effective electron conduction band mass changes abruptly across the heterojunction. For the GaAs-based nanodevices [6, 7], these changes are small and have been neglected in Refs. [86, 88].

Another important problem is related with the screening of the electron–electron Coulomb interaction. The main sources of this screening are valence electrons, atomic cores, phonons, and charges induced on the leads. The screening via the valence electrons and atomic cores is usually included with the help of the static screening of the Coulomb interaction by the high-frequency relative electric permittivity ε_∞. The discontinuity of ε_∞ (dielectric mismatch) across the interface leads to an electric polarization of the interface, which, in turn, entails a modification of the electron–electron Coulomb interaction [142]. An analytic expression for the polarization potential was obtained for the spherical QD [143]. For the QDs with lower symmetry, the Poisson equation has to be solved numerically to find the polarization potential [144].

The electron-phonon coupling is the another important source of screening of the interelectron interaction. In the nanostructures composed of the semiconductor compounds, which are always more or less ionic, the coupling with longitudinal optical (LO) phonons plays the major role in this type of screening. Usually, this effect is taken into account by substituting the high-frequency electric permittivity ε_∞ by the static electric permittivity ε_s. This substitution overestimates the screening that results in an underestimation of the interelectron repulsion. The theory of the electron–LO–phonon interaction, applied to the two-electron system bound to a positive donor center (D^- problem) [105, 106], leads to the approximate description of the LO-phonon-induced screening with the help of effective dielectric function $\widetilde{\varepsilon}(r_{12})$, which modifies the electron–electron Coulomb interaction as follows:

$$\widetilde{V}(r_{12}) = \frac{1}{\widetilde{\varepsilon}(r_{12})} \frac{\kappa e^2}{r_{12}}, \tag{53}$$

where r_{12} is the electron–electron distance. The theory [105, 106] yields the following asymptotic dependence of the effective dielectric function on the interelectron distance:

$$\widetilde{\varepsilon}(r_{12}) \to \varepsilon_\infty, \quad \text{if } r_{12} \to 0, \tag{54}$$

and

$$\widetilde{\varepsilon}(r_{12}) \to \varepsilon_s, \quad \text{if } r_{12} \to \infty. \tag{55}$$

At the intermediate distances, $\widetilde{\varepsilon}(r_{12})$ takes on the values between ε_∞ and ε_s. In the theoretical description [86] of the three-terminal QD of Tarucha et al. [7], this space dependence of the LO-phonon-induced screening was partly taken into account as follows [86]: the Coulomb interaction between the electrons confined within the QD was screened by ε_∞, while the

Coulomb field created by the QD-confined electrons in the more distant n-GaAs layers was screened by ε_s. This approach [86] includes the major features of the interelectron Coulomb repulsion that result from the electron-LO-phonon coupling.

In the electrostatically gated QDs, the electron–electron interaction is also screened by the charges induced on the surfaces of metallic electrodes. This type of screening can be taken into account either by an appropriate modification of the interelectron repulsion [83] or by imposing the proper boundary conditions on the total electrostatic potential in the nanodevice [86, 88]. The first method of screening was proposed by Bruce and Maksym [83]. However, the applicability of the approach presented in Ref. [83] is limited to a simple parallel-plate geometry of the nanodevice. The method used in Refs. [86, 88] is based on the numerical solution of the Poisson equation. Therefore, this approach [86, 88] is applicable to an arbitrary geometry of the nanodevice. The effect of this type screening on the lateral confinement potential in the cylindrical three-electrode QD is shown in Fig. 23.

Another important issue is related to the problem of a charge relaxation in the nanodevice during the transmission of a single electron through the QD. If the transmitted electron is in the quantum state in which the probability of its sojourn within the QD is much smaller than the probability of finding the electron outside the QD, we deal with a *slow relaxation*. It appears that the calculation results [86] obtained for the three-terminal nanodevice under assumption of the slow relaxation very well agree with the experimental data [7, 23]. Therefore, in the calculation [86] of N- and $(N + 1)$-electron energies used in single-electron transport condition (5), the confinement potentials were the same. The confinement potential, used to describe the process of the tunneling of the $(N + 1)$th electron through the QD, was calculated as that stemming from the presence of N electrons in the QD.

To determine the electronic properties of the electrostatically gated QDs, we have to know the confinement potential that is created by the external voltages applied to the electrodes and the band offsets. The confinement potential is also sensitive to the other parameters of the nanodevice, in particular, its geometry and doping. The knowledge of the realistic profile of the confinement potential is important for a nanodevice design with the required electronic properties and for a theoretical description of the QD-confined electron states. It is impossible to determine the confinement potential by experimental techniques. Therefore, the confinement potential has to be either calculated from the first principles of electrostatics [83–88] or assumed in an analytical form. In the majority of theoretical papers (e.g., Refs. [62–64, 68, 69, 72–77, 82, 109, 107]), the confinement potential was assumed in some model form. The most commonly used are the rectangular and parabolic confinement potentials [62–64, 68, 69, 72–77, 82]. The more general and realistic profiles of the confinement potential can be modeled with the use of the Gaussian [109] and power-exponential [107] functions. The model potentials usually neglect the important dependencies of the confinement potential on the voltages applied to the electrodes, the concentration of ionized impurities, the charge of the electrons confined within the QDs, and the charge induced on the leads. These quantities essentially modify the electrostatic field in the nanodevice and thus change the confinement potential. All these effects were taken into account in Refs. [86, 88], in which the self-consistent procedure was applied to solve the Poisson-Schrödinger problem for two-terminal [88] and three-terminal [86] nanodevices. The very good agreement of the calculation results [86, 88] with the single-electron capacitance spectroscopy data for the two-electrode QDs [6] and the single-electron transport spectroscopy data for the three-electrode QDs [7] proves the reliability of the method elaborated in Refs. [86, 88]. Similar calculations, can be found in Refs. [83, 85, 87].

The realistic profile of the confinement potential was calculated in Refs. [86, 88]. Let us summarize the results [86, 88] for only the spatial dependence of the confinement potential. The vertical component of this potential results from the band offsets and can be quite well approximated by a sequence of rectangular potential barriers and potential wells. The lateral confinement potential possesses a more complex form as a function of the radial coordinate. It can be quite well approximated by the parabolic potential but only near the center of the QD with a small radius. The nonparabolic corrections play a role already inside the QD region. At the QD boundary, the confinement potential has to be finite. It was shown [88] that the power-exponential function [107] can be very well fitted to the numerical solutions

of the Poisson equation. Moreover, the model confinement potential [107] assures that the asymptotic boundary values are reached in a continuous manner. For the two-terminal QD [6] with the radius of the order of 1 μm, the confinement potential is flat in the center of the QD. The flatness of the confinement potential entails important physical consequences, namely, that the fluctuating electric field, created by the ionized impurities, essentially affects the energy spectra of the QD confined electrons.

The confinement potential in the electrostatic QDs is determined by the charges in the nanodevice. The charges in the leads are maintained by external sources (external voltages) and are taken into account in the theoretical treatment [86, 88] by putting the proper boundary conditions on the total electrostatic potential. Inside the nanodevice, there is also the space charge associated with ionized donors in n-doped layers. Additionally, we have to take into account the charge of the electrons confined in the QD. At low temperature, the donor impurity becomes ionized if the potential energy of the electrostatic field at the donor site exceeds the binding energy of the electron to the donor center. The electrostatic field is strongly affected by the QD-confined electrons. However, the wave functions of the electrons confined in the QD depend on the potential confining the electrons in the QD. As a result, we deal with the complex self-consistent problem, which has to be solved by the iterative procedure for the Poisson and Schrödinger equations. Additionally, the charge of the ionized donors has to be also determined in the self-consistent manner [86]. This is especially important for the three-electrode QDs [7] in which the presence of the gate electrode leads to a nonuniform distribution of the ionized donors. In the other papers (e.g., Ref. [85]), the ionized donor distribution was assumed to be uniform. This assumption is justified for the two-electrode QDs [6] but only for the ionized donors located in the AlGaAs barrier layers.

It is interesting to consider the role of the gate electrode in the two-terminal [6] and three-terminal [7] QDs. In both types of vertical QDs, the gate electrode is placed at different positions: it is the position on the top of the cylinder in the two-terminal QD [6] and the position at the side of the pillar in the three-terminal QD [7]. Despite the different gate placements, the effect of this electrode is, to some extent, similar in both nanodevices. Namely, the gate electrode allows us to control the electrostatic field, confining the electrons in the QD. In particular, the lateral confinement of the electrons in the two-terminal nanodevice [6] results from the inhomogeneity of the electric field created between the gate and bottom electrode. In spite of the same mechanism of creation of the confinement potential, there are essential differences between the two types of the electrostatic QDs. These differences are observed in the dependence of the chemical potential on the gate voltage (cf. Figs. 15 and 16). In the two-electrode QD of Ashoori et al. [6], this dependence is almost linear, that is, the gate voltage–to–energy conversion factor is nearly constant (Fig. 16). In the three-electrode QD of Tarucha et al. [7], the dependence of the QD chemical potential on the gate voltage is nonlinear, that is, the conversion factor strongly depends on the gate voltage (cf. Fig. 15). This nonlinearity can be explained as follows. The varying gate voltage changes the range of donor ionization in the n-type layers that adhere the source and drain in the three-terminal nanodevice (see Fig. 4) or are located in the substrate in the two-terminal nanodevice (see Fig. 2). The change of the ionization range determines the corresponding change in the effective position of the electrode. In the two-terminal nanodevice [6], the electrons are confined within the QD at approximately half the distance between the gate and the substrate (i.e., faraway from both the electrodes). In this case, the gate-induced change of size of the donor ionization region leads to a negligibly small nonlinearity of the chemical potential of the QD as a function of the gate voltage. In the three-terminal nanodevice [7], the QD is located much closely to the first n-doped layer, which contains the ionized donors, than to the gate. In this case, the change of size of the ionized-donor domain leads to the clear nonlinearity of the chemical potential as a function of the gate voltage.

In the two-terminal nanodevice [6], the lateral confinement energy is a nonlinear and nonmonotonic function of the cap radius (see Fig. 29). Also the other characteristics of the two-terminal nanodevice are very sensitive to the cap radius (see Fig. 29). As a result, the shape of the lateral confinement potential is very sensitive to the geometry of the nanodevice, in particular to the cap radius [88]. By changing the cap radius we can obtain different

shapes of the confinement potential: from almost linear through Gaussian (parabolic near the axis) to almost rectangular. In this way, by changing the radius of the top electrode, we can model the electronic properties of the QD, which are determined by the confinement potential.

In this section, we have discussed the effects that most strongly affect the electronic properties of the gate-controlled QDs. In the calculations (e.g., Refs. [86, 88]), some of these effects were fully or partly taken into account and some of them were neglected. For the three-terminal QD [7], we can give a quantitative estimate of the neglected effects by comparing the measured and calculated positions of the first peak on the current versus gate voltage plot for the zero bias (Fig. 15). In Ref. [86], the single fitting parameter (the radius of the cylindrical pillar) was adjusted to reproduce the positions of the next 11 peaks. Therefore, the discrepancy obtained for the first peak between the measured [7] and calculated [86] position can be treated as a quantitative measure of all the corrections that stem from the neglected effects. The inaccuracy (cf. Fig. 15) of the theoretical method [86], estimated in such a way, is very small.

12. APPLICATIONS

In this section, we discuss the most important present and future applications of the electrostatically gated QDs. Nowadays, the QD based single-electron transistors are constructed. The gated QDs are expected to be applied in future quantum computers.

12.1. Single-Electron Transistor

The three-terminal QD nanodevice [7] is a prototype of the single-electron transistor (SET). Contrary to the conventional transistor, the SET can be turned on and off at different gate voltage values (Fig. 6). Each on/off switching of the SET corresponds to the flow of the single electron through the nanodevice. Figure 6 shows that the sharp current peaks arise from the plateaus of zero current at several, well-defined gate voltages. Each peak of the current results from many sequential tunneling events of the single electrons via the QD. We note that for the two-state transistor operation we have to limit the applied gate-voltage regime to that corresponding to two chosen peaks only. The SET possesses an advantage of small power consumption and short switching time but a disadvantage of low operating temperature.

After the first demonstration of the SET by Fulton and Dolan [145], many experimental efforts were mainly focused on raising the operating temperature of this nanodevice. The operating temperature that was initially in the sub-Kelvin range has been raised to room temperature [47, 146, 147]. The SETs are used as sensitive electrometers [146, 147] that detect the change of electrostatic potential due to the injection of single electrons. This in turn leads to the application of SETs as detectors in single-electron memory cells [146, 148].

The vertical SET was used to a manipulation of the lateral confinement geometry of the QD [17]. Moreover, the single-electron capacitance spectroscopy measurements were performed on the QDs with the help of the SET [18]. The application of the SET permitted measurement of a few thousand individual electron additions in a single vertical QD, starting from the first one, with a great charge sensitivity [18]. The single-electron tunneling through the coupled QDs was detected with a radio-frequency SET [149]. In these experiments [149], accurate current measurements were performed by counting the single-electron tunneling events. The SET is treated as one of the best candidates for future logic large-scale-integrated circuits because of its ultralow power consumption and high tunability [30].

12.2. Quantum Computation

Quantum computation directly employs the laws of quantum mechanics to perform calculations [150]. Nowadays, the theory of quantum computation has become a mature theory [150]. Moreover, many experimental realizations of quantum computers have been proposed [150]. In several papers (e.g., Refs. [31–33, 35–39, 42–44, 151], the implementation of QDs was proposed to realize future quantum computers.

The quantum computation makes use of *qubits*, which are the units of quantum information [150], and *quantum logic gates*, which are used to transform the qubits. A *quantum algorithm* consists of a sequence of logic operations, which are performed on the qubits. For the physical realization of the qubit, we can use any two-level quantum system. For example, the electron spin is a very good candidate to represent the qubit. Most proposals [34, 44, 151] that apply the QDs to the quantum computation rely on the use of the electron-spin states as the qubits. The application of QD-confined excitons and biexcitons as qubits was also considered [34]. Moreover, the qubits can be realized in QDs directly on the electron states by detecting either the presence or absence of the single-electron charge in the QD [45]. Several investigations [36, 40, 42, 43] are devoted to the optically driven quantum computer based on the coupled QDs.

The physical realization of quantum computations is possible provided that certain conditions are satisfied [151]. DiVincenzo [151] formulated the following requirements for the implementation of the quantum computation:

(1) The qubits have to be realizable in a scalable physical system.
(2) The initial qubit state has to be prepared with high precision.
(3) The unitary time evolution of the qubits has to be fully controllable.
(4) The decoherence time has to be much longer than the gate operation time.
(5) The final state of the qubit has to be measurable with high enough precision.

These requirements put certain limitations on the quantum computing technology. The main problems are connected with a scalability of the system of qubits (condition 1) and a fragility of the qubits (condition 4). We have to maintain the controlled unitary evolution of the qubits until the calculations are completed. It is possible to perform the controlled time evolution of the quantum system provided the quantum system is completely isolated from an environment. Nevertheless, the complete isolation of the quantum system disables performing the readout operations. Therefore, a weak coupling with the environment is necessary. Unfortunately, this coupling leads to the decay and decoherence of qubits, which reduce the performance of the quantum computer. When using the electron-spin states to realize the qubits, we exploit the fact that the lifetime of these states is reasonably long [58]. The lifetime of the electron-spin Zeeman states was estimated to be $\geq 50\ \mu$s in the lateral gated QDs. On the basis of the results of experiments [58], we can neglect the decay of spin qubits during the gate operation time. However, the decoherence time of the QD qubits is rather short because the QD confined electrons, as all the particles in a solid medium, interact with other electrons and atomic nuclei. Even at very low temperature, these interactions are nonnegligible. One can quantitatively estimate the effect of decoherence [152] introducing a ratio of the decoherence time to the single-operation time. For the recently studied QDs, this ratio has been estimated to be of the order of 10^3 [152]. The decoherence–to–operation time ratio for the QDs appears to be much smaller than that estimated for other physical systems designed for application in quantum computation (e.g., for ion traps the corresponding ratio was estimated to be $\sim 10^{13}$ [152]). At the recent stage of research, it seems that many problems have to be solved to reduce the effect of decoherence in QDs.

Many efforts were undertaken toward a physical realization of quantum computation on the QDs. Here, we mention only few of them. A realization of a quantum register was studied [36] in the vertical gated QDs. Sanders et al. [36] considered the coupled asymmetric QDs with dipole–dipole interaction between the electrons confined in the adjacent dots and discussed a possibility of constructing the three-qubit register. The possible implementation of the QDs as spin filters and single-spin memory was studied in Ref. [37]. The spin filter, which produces the spin-polarized current, is very desirable for the readout operations of spin qubits. The mapping of spin states onto the orbital states and vice versa was proposed to realize high-finesse optical quantum gates [44]. Optically driven qubits were studied [42] in the coupled QDs. In Ref. [40], a generation of quantum entanglement and information processing with excitons confined in the QDs was proposed.

An experimental study of the electron spin as a candidate for a scalable qubit was performed [58] in InAs/GaAs lateral QDs. The authors [58] measured the spin relaxation time and found a lower bound to it. Moreover, the spin Zeeman splitting was directly observed

by the single-electron transport spectroscopy [58]. The coherent manipulation of spin qubits was performed [59] by applying the high-speed voltage pulses to the laterally coupled QDs. These achievements [58, 59] demonstrate that the implementation of electron spin qubits is within the reach of modern advanced technology.

13. CONCLUSIONS

The results from Refs. [86, 88] show that by taking into account all the relevant parameters of the nanodevice it is possible to obtain the correct quantitative description of the electrostatically gated vertical QDs [6, 7, 23]. The very good agreement with experiment obtained in Refs. [86, 88] provides an argument against the skepticism [13] related with a possibility of a quantitative comparison of the theory of QDs with experiment. Of course, the unavoidable inaccuracies in the nanodevice fabrication can randomly disturb the perfect cylindrical symmetry of the QDs [13], but they can be treated as small perturbations, which do not change the main characteristics of the nanodevice. The theory, elaborated in Refs. [86, 88], yields the quantitatively correct interpretation of the electronic properties of the vertical QDs with both two [6] and three [7] electrodes attached and incorporates all the relevant nanodevice parameters, which allows us to describe the major characteristics of the QDs. For the electrostatically gated QDs, a set of the physically relevant parameters includes a geometry, a composition, a doping, external voltages, ohmic contacts, and Schottky barriers. Moreover, the effect of screening of the electron–electron interaction is also important.

The electronic properties of the electrostatically gated QDs are determined by the confinement potential. In the electrostatically gated vertical QDs [6, 7], the vertical confinement of the electrons results from the band offsets and the lateral confinement is of the electrostatic origin. The band offsets are determined by the composition of the adjacent layers. The change of thickness of the subsequent layers modifies the profile of the vertical confinement potential. The laterally directed electrostatic field is created by the charges gathered on the gate and the ionized donors and is modified by the charge of the electrons confined within the QD.

The QDs are often called *artificial atoms*. Similarly, as in a natural atom, the electrons confined in a QD form localized bound states with discrete energy levels. In the natural atoms, the electrons are bound to the nucleus by the Coulomb potential, which is divergent at the nucleus position. On the contrary, the confinement potential that binds electrons in the QD is smooth at the dot center and can be well approximated by the power-exponential function [Eq. (25)]. The power-exponential potential [107] is very similar to the Woods-Saxon potential [153], which was introduced in nuclear physics to describe a proton-nucleus scattering. Also other potentials used in the theory of the atomic nucleus are similar to those applied to the QDs (e.g., a truncated parabolic potential is commonly used to model the atomic nucleus). Because of the similarity of the QD-confinement potential to the model potentials used in the theory of atomic nucleus we can treat the QD as a solid-state analog of the atomic nucleus (i.e., it might be called *artificial nucleus*). Because of the similar shapes of the binding potentials, the quantum states of electrons confined in the QD more strongly resemble those of nucleons in atomic nuclei than the electron states of natural atoms [13].

In summary, the electrostatically gated QDs yield a unique opportunity of tailoring the electronic characteristics of nanodevices. By changing the parameters of the nanodevice, in particular, the external voltages, we can obtain the quantum states of few-electron systems confined within the QD with the designed properties. This opens the way for quantum engineering with electrons. The electrostatically gated QDs have been already applied as single-electron transistors and are expected to play an important role in a future quantum-computer technology.

GLOSSARY

Artificial atom   A synonym of the quantum dot (QD). However, the artificial atom can denote the QD that contains the confined electrons bound in the atomic-like states with discrete energy levels.

Artificial molecule   Two or more coupled QDs separated by potential barrier layers.

Electrostatically gated QD (electrostatically defined QD, electrostatic QD, gate-controlled QD, gated QD)   The QD in which the lateral confinement of the charge carriers results from the inhomogeneous electrostatic field created by the electrodes attached to the QD and the ionized donors.

Maximum-density droplet (MDD)   A phase of the QD-confined electron system in which all the electrons are spin polarized by the external magnetic field and—in the cylindrical QDs—occupy the one-particle orbitals with the subsequent angular momenta. At the sufficiently high magnetic field, the MDD decays into the Wigner molecule. The spatial electron density distribution in the MDD has a form of a flat maximum and abruptly falls down to zero at the edge.

Quantum bit (qubit)   A unit of quantum information. A qubit can be realized by any two-state quantum system.

Quantum computation   Performing the quantum logic operations on the qubits with a direct exploitation of the laws of quantum mechanics.

Quantum dot (QD)   A nanostructure in which the charge carriers (electrons and holes) are confined in all the three dimensions within the region of nanometer size. The QD is usually made of semiconducting materials.

Quantum logic operation (quantum logic gate)   Performing the unitary transformation on the qubit. There are one- and two-qubit quantum gates depending on the initial qubit state.

Single-electron transistor (SET)   A QD-based nanodevice in which the current flows as a result of sequential single-electron tunneling events. The SET can be switched on and off at different, well-defined values of the gate voltage.

Vertical QD   The QD which consists of sequence of layers made of different semiconductors. The layers are grown on the substrate in the z (vertical) direction and form a pillar, which usually has the cylindrical symmetry. The confinement of the charge carriers in the z direction results from band offsets and the confinement in the lateral (x, y) directions is due to the external inhomogeneous electrostatic field and the presence of surfaces of the pillar.

Wigner molecule   A phase of the QD confined few-electron system in which the electrons are localized at different spatial sites, which form the ordered island-like structure. The Wigner molecule is created by the sufficiently high magnetic field or the size effect in the QD.

ACKNOWLEDGMENTS

REFERENCES

1. L. Jacak, P. Hawrylak, and A. Wójs, "Quantum Dots." Springer, Berlin, 1998.

2. P. A. Maksym and T. Chakraborty, *Phys. Rev. Lett.* 65, 108 (1990).

3. M. A. Kastner, *Phys. Today* 16, 24 (1993).

4. D. Leonard, M. Krishnamurthy, C. M. Reaves, S. P. DenBaars, and P. M. Petroff, *Appl. Phys. Lett.* 63, 3203 (1993).

5. B. T. Miller, W. Hansen, S. Manus, R. J. Luyken, A. Lorke, J. P. Kotthaus, S. Huant, G. Medeiros-Ribeiro, and P. M. Petroff, *Phys. Rev. B* 56, 6764 (1997).

6. R. C. Ashoori, H. L. Stormer, J. S. Weiner, L. N. Pfeiffer, K. W. Baldwin, and K. W. West, *Phys. Rev. Lett.* 71, 613 (1993).

7. S. Tarucha, T. Honda, R. J. van der Hage, and L. P. Kouwenhoven, *Phys. Rev. Lett.* 77, 3613 (1996).

8. P. A. Maksym, H. Imamura, G. P. Mallon, and H. Aoki, *J. Phys.: Condens. Matter* 12, R299 (2000).

9. A. D. Yoffe, *Adv. Phys.* 42, 173 (1993).

10. N. F. Johnson, *J. Phys.: Condens. Matter* 7, 965 (1995).

11. P. A. Maksym, L. D. Hallam, and J. Weiss, *Physica B* 212, 213 (1995).

12. L. P. Kouwenhoven, D. G. Austing, and S. Tarucha, *Rep. Prog. Phys.* 64, 701 (2001).

13. S. M. Reimann and M. Manninen, *Rev. Mod. Phys.* 24, 1283 (2002).

14. M. A. Kastner, *Rev. Mod. Phys.* 64, 849 (1992).

15. Y. Wang and S. Y. Chou, *IEEE Trans. Electron Devices* 40, 2136 (1993).

16. D. G. Austing, T. Honda, Y. Tokura, and S. Tarucha, *Jpn. J. Appl. Phys.* 34, 1320 (1995).

17. D. G. Austing, T. Honda, and S. Tarucha, *Physica E* 2, 583 (1998).

18. M. Koltonyuk, D. Berman, N. B. Zhitenev, R. C. Ashoori, L. N. Pfeiffer, and K. W. West, *Appl. Phys. Lett.* 74, 555 (1999).

19. P. Hawrylak, *Phys. Rev. Lett.* 71, 3347 (1993).

20. S.-R. Eric Yang, A. H. MacDonald, and M. D. Johnson, *Phys. Rev. Lett.* 71, 3194 (1993).

21. O. Klein, C. Chamon, D. Tang, D. M. Abusch-Magder, U. Meirav, X.-G. Wen, M. A. Kastner, and S. J. Wind, *Phys. Rev. Lett.* 74, 785 (1995).

22. R. C. Ashoori, *Nature* 379, 413 (1996).

23. L. P. Kouwenhoven, T. H. Oosterkamp, M. W. S. Danoesastro, M. Eto, D. G. Austing, T. Honda, and S. Tarucha, *Science* 278, 1788 (1997).

24. T. H. Oosterkamp, J. W. Janssen, L. P. Kouwenhoven, D. G. Austing, T. Honda, and S. Tarucha, *Phys. Rev. Lett.* 82, 2931 (1999).

25. P. C. Main, A. S. G. Thornton, R. J. A. Hill, S. T. Stoddart, T. Ihn, L. Eaves, K. A. Benedict, and M. Henini, *Phys. Rev. Lett.* 84, 729 (2000).

26. L. P. Rokhinson, L. J. Guo, S. Y. Chou, and D. C. Tsui, *Phys. Rev. Lett.* 87, 166802 (2001).

27. Y. Takahashi, M. Nagase, H. Namatsu, K. Kurihara, K. Iwdate, Y. Nakajima, K. Murase, and M. Tabe, *Electron. Lett.* 31, 136 (1994).

28. D. L. Klein, R. Roth, A. K. L. Lim, A. P. Alivisatos, and P. L. McEuen, *Nature* 389, 699 (1997).

29. L. P. Rokhinson, L. J. Guo, S. Y. Chou, and D. C. Tsui, *Appl. Phys. Lett.* 76, 1591 (2000).

30. Y. Takahashi, A. Fujiwara, K. Yamazaki, H. Namatsu, K. Kurihara, and K. Murase, *Appl. Phys. Lett.* 76, 637 (2000).

31. A. Barenco, D. Deutsch, A. Ekert, and R Jozsa, *Phys. Rev. Lett.* 74, 4083 (1995).

32. D. Loss and D. P. DiVincenzo, *Phys. Rev. A* 57, 120 (1998).

33. G. Burkard, D. Loss, and D. P. DiVincenzo, *Phys. Rev. B* 59, 2070 (1999).

34. G. Burkard and D. Loss, "Semiconductor Spintronics and Quantum Computation" (D. D. Awschalom, D. Loss, and N. Samarth, Eds.), p. 229. Springer, Berlin, 2002.

35. T. Tanamoto, *Phys. Rev. A* 61, 022305 (2000).

36. G. D. Sanders, K. W. Kim, and W. C. Holton, *Phys. Rev. B* 61, 7526 (2000).

37. P. Recher, E. V. Sukhorukov, and D. Loss, *Phys. Rev. Lett.* 85, 1962 (2000).

38. H. Sasakura, S. Muto, and T. Ohshima, *Physica E* 10, 458 (2001).

39. J. H. Jefferson, M. Fearn, D. L. J. Tipton, and T. P. Spiller, *Phys. Rev. A* 66, 042328 (2002).

40. J. H. Reina, L. Quiroga, and N. F. Johnson, *Phys. Rev. A* 62, 012305 (2000).

41. F. Troiani, U. Hohenester, and E. Molinari, *Phys. Rev. B* 62, R2263 (2000).

42. J. H. Oh, D. Ahn, and S. W. Hwang, *Phys. Rev. A* 62, 052306 (2000).

43. S. Cortez, O. Krebs, S. Laurent, M. Senes, X. Marie, P. Voisin, R. Ferreira, G. Bastard, J.-M. Gerard, and T. Amand, *Phys. Rev. Lett.* 89, 207401 (2002).

44. F. Troiani, E. Molinari, and U. Hohenester, *Phys. Rev. Lett.* 90, 206802 (2003).

45. T. M. Buehler, D. J. Reilly, R. Brenner, A. R. Hamilton, A. S. Dzurak, and R. G. Clark, *Appl. Phys. Lett.* 82, 577 (2003).

46. D. G. Austing, T. Honda, and S. Tarucha, *Semicond. Sci. Technol.* 12, 631 (1997).

47. Y. Takahashi, M. Nagase, H. Namatsu, K. Kurihara, K. Iwfate, Y. Nakajima, S. Horiguchi, K. Murase, and M. Tabe, *Electron. Lett.* 31, 136 (1995).

48. L. P. Kouwenhoven and P. L. McEuen, "Nanotechnology" (G. Timp, Ed.), p. 471. Springer, New York, 1999.

49. D. G. Austing, T. Honda, and S. Tarucha, *Semicond. Sci. Technol.* 11, 388 (1996).

50. S. Tarucha, D. G. Austing, Y. Tokura, W. G. van der Wiel, and L. P. Kouwenhoven, *Phys. Rev. Lett.* 84, 2485 (2000).

51. S. Tarucha, D. G. Austing, T. Honda, and R. van der Hage, *Jpn. J. Appl. Phys.* 36, 3917 (1997).

52. R. C. Ashoori, N. B. Zhitenev, L. N. Pfeiffer, and K. W. West, *Physica E* 3, 15 (1998).

53. N. B. Zhitenev, M. Brodsky, R. C. Ashoori, L. N. Pfeiffer, and K. W. West, *Science* 285, 715 (1999).

54. D. G. Austing, S. Sasaki, S. Tarucha, S. M. Reimann, M. Koskinen, and M. Manninen, *Phys. Rev. B* 60, 11514 (1999).

55. R. C. Ashoori, H. L. Stormer, J. S. Weiner, L. N. Pfeiffer, S. J. Pearton, K. W. Baldwin, amd K. W. West, *Phys. Rev. Lett.* 68, 3088 (1992).

56. H. Drexler, D. Leonard, W. Hansen, J. P. Kotthaus, and P. M. Petroff, *Phys. Rev. Lett.* 73, 2252 (1994).

57. T. Fujisawa, D. G. Austing, Y. Tokura, Y. Hirayama, and S. Tarucha, *Phys. Rev. Lett.* 88, 236802 (2002).

58. R. Hanson, B. Witkamp, L. M. K. Vandersypen, L. H. Wilems van Beveren, J. M. Elzerman, and L. P. Kouwenhoven, *Phys. Rev. Lett.* 91, 196802 (2003).

59. T. Hayashi, T. Fujisawa, H. D. Cheong, Y. H. Jeong, and Y. Hirayima, *Phys. Rev. Lett.* 91, 226804 (2003).

60. N. F. Johnson and M. C. Payne, *Phys. Rev. B* 45, 3819 (1992).

61. U. Merkt, J. Huser, and M. Wagner, *Phys. Rev. B* 43, 7320 (1991).

62. M. Wagner, U. Merkt, and A. V. Chaplik, *Phys. Rev. B* 45, 1951 (1992).

63. M. Macucci, K. Hess, and G. J. Iafrate, *Phys. Rev. B* 48, 17354 (1993).

64. D. Pfannkuche, V. Gudmundsson, and P. A. Maksym, *Phys. Rev. B* 47, 2244 (1993).

65. D. Jovanovic and J.-P. Leburton, *Phys. Rev. B* 49, 7474 (1994).

66. L. Wang, J. K. Zhang, and A. R. Bishop, *Phys. Rev. Lett.* 73, 585 (1994).

67. F. M. Peeters and V. A. Schweigert, *Phys. Rev. B* 53, 1468 (1996).

68. V. Halonen, P. Hyvönen, P. Pietiläinen, and T. Chakraborty, *Phys. Rev. B* 53, 6971 (1996).

69. Y. Tanaka and H. Akera, *Phys. Rev. B* 53, 3901 (1996).

70. J. König, J. Schmid, H. Schoeller, and G. Schön, *Phys. Rev. B* 54, 16820 (1996).

71. Y. Alhassid and H. Attias, *Phys. Rev. B* 54, 2696 (1996).

72. M. Eto, *Jpn. J. Appl. Phys.* 36, 3924 (1997).

73. T. Ezaki, N. Mori, and C. Hamaguchi, *Phys. Rev.* 56, 6428 (1997).

74. O. Steffens, U. Rössler, and M. Surhrke, *Europhys. Lett.* 42, 529 (1998).

75. O. Steffens, M. Suhrke, and U. Rössler, *Physica B* 256–258, 147 (1998).

76. P. A. Maksym, *Physica B* 249–251, 233 (1998).

77. I.-H. Lee, V. Rao, R. M. Martin, and J.-P. Leburton, *Phys. Rev. B* 57, 9035 (1998).

78. L. R. C. Fonseca, J. L. Jimenez, J. P. Leburton, and R. M. Martin, *Phys. Rev. B* 57, 4017 (1998).

79. M. Rontani, F. Rossi, F. Manghi, and E. Molinari, *Appl. Phys. Lett.* 72, 957 (1998).

80. H. Tamura, *Physica B* 249–251, 210 (1998).

81. Y. Alhassid, *Phys. Rev. B* 58, R13383 (1998).

82. M. Rontani, F. Rossi, F. Manghi, and E. Molinari, *Phys. Rev. B* 59, 10165 (1999).

83. N. A. Bruce and P. A. Maksym, *Phys. Rev. B* 61, 4718 (2000).

84. S. Bednarek, B. Szafran, and J. Adamowski, *Phys. Rev. B* 61, 4461 (2000).

85. P. Matagne, J.-P. Leburton, J. Destine, and G. Cantraine, *J. Comput. Mode. Eng. Sci.* 1, 1 (2000).

86. S. Bednarek, B. Szafran, and J. Adamowski, *Phys. Rev. B* 64, 195303 (2001).

87. P. Matagne and J. P. Leburton, *Phys. Rev. B* 65, 235323 (2002).

88. S. Bednarek, B. Szafran, K. Lis, and J. Adamowski, *Phys. Rev. B* 68, 155333 (2003).

89. L. P. Kouwenhoven, N. C. van der Vaart, A. T. Johnson, W. Kool, C. J. P. M. Harmans, J. G. Williamson, A. A. M. Staring, and C. D. Foxon, *Z. Phys. B* 85, 367 (1991).

90. T. Schmidt, M. Tewordt, R. H. Blick, R. J. Haug, D. Pfannkuche, K. von Klitzing, A. Förster, and H. Lüth, *Phys. Rev. B* 51, 5570 (1995).

91. N. B. Zhitenev, R. C. Ashoori, L. N. Pfeiffer, and K. W. West, *Phys. Rev. Lett.* 79, 2308 (1997).

92. S. M. Cronenwett, T. H. Oosterkamp, and L. P. Kouwenhoven, *Science* 281, 540 (1998).

93. D. Goldhaber-Gordon, H. Shtrikman, D. Mahalu, D. Abisch-Magder, U. Meirav, and M. A. Kastner, *Nature* 391, 156 (1998).

94. L. P. Rokhinson, L. J. Guo, S. Y. Chou, and D. C. Tsui, *Phys. Rev. B* 60, R16319 (1999).

95. S. Sasaki, S. De Franceschi, J. M. Elzerman, W. G. van der Wiel, M. Eto, S. Tarucha, and L. P. Kouwenhoven, *Nature* 405, 764 (2000).

96. J. Schmid, J. Weis, K. Eberl, and K. v. Klitzing, *Phys. Rev. Lett.* 84, 5824 (2000).

97. S. De Franceschi, S. Sasaki, J. M. Elzerman, W. G. van der Wiel, S. Tarucha, and L. P. Kouwenhoven, *Phys. Rev Lett.* 86, 878 (2001).

98. B. Szafran, S. Bednarek, and J. Adamowski, *Phys. Rev. B* 65, 035316 (2002).

99. D. Heitmann, K. Bollweg, V. Gudmundsson, T. Kurth, and S. P. Riege, *Physica E* 1, 204 (1997).

100. K. Hinzer, P. Hawrylak, S. Fafard, M. Bayer, O. Stern, A. Gorbunov, and A. Forchel, *Phys. Rev. B* 63, 075313 (2001).

101. J. Adamowski, S. Bednarek, and B. Szafran, *Acta Phys. Pol. A* 100, 145 (2001).

102. S. Bednarek, B. Szafran, and J. Adamowski, *Microelectron. Eng.* 51–52, 99 (2000).

103. A. H. MacDonald, E. S. R. Yang, and M. D. Johnson, *Aust. J. Phys.* 46, 345 (1993).

104. K. Jauregui, W. Häusler, and B. Kramer, *Europhys. Lett.* 24, 581 (1993).

105. J. Adamowski, *Phys. Rev. B* 39, 13061 (1989).

106. S. Bednarek and J. Adamowski, *Phys. Rev. B* 57, 14729 (1998).

107. M. Ciurla, J. Adamowski, B. Szafran, and S. Bednarek, *Physica E* 15, 261 (2002).

108. V. Ranjan, R. K. Pandey, M. K. Harbola, and V. A. Singh, *Phys. Rev. B* 65, 045311 (2002).

109. J. Adamowski, M. Sobkowicz, B. Szafran, and S. Bednarek, *Phys. Rev. B* 62, 4234 (2000).

110. K. Lis, S. Bednarek, B. Szafran, and J. Adamowski, *Physica E* 17, 494 (2003).

111. V. M. Bedanov and F. M. Peeters, *Phys. Rev. B* 49, 2667 (1994).

112. K. T. R. Davies, H. Focard, S. Krieger, and M. S. Weiss, *Nucl. Phys. A* 342, 111 (1980).

113. R. Kossloff and H. Tal-Ezer, *Chem. Phys. Lett.* 127, 223 (1986).

114. S. Bednarek, T. Chwiej, J. Adamowski, and B. Szafran, *Phys. Rev. B* 67, 115323 (2003).

115. P. Knowles, M. Schültz, and H.-J. Werner, in "Modern Methods and Algorithms of Quantum Chemistry" (J. Grotendorst, Ed.), Vol. 3, p. 97. NIC Series, John von Neumann Institute of Computing, Jűlich, 2000.

116. B. Szafran, S. Bednarek, and J. Adamowski, *Phys. Rev. B* 67, 115323 (2003).

117. M. Rontani, S. Amaha, K. Muraki, F. Manghi, E. Molinari, S. Tarucha, and D. G. Austing, *Phys. Rev. B* 69, 085327 (2004).

118. E. P. Wigner, *Phys. Rev.* 46, 1934 (1002).

119. C. C. Grimes and G. Adams, *Phys. Rev. Lett.* 42, 795 (1979).

120. W. Häusler and B. Kramer, *Phys. Rev. B* 47, 16353 (1993).

121. H. M. Műller and S. E. Koonin, *Phys. Rev.* 54, 14532 (1996).

122. T. Prus, B. Szafran, J. Adamowski, and S. Bednarek, *J. Phys.: Condens. Matter* 16, 1425 (2004).

123. C. Yannouleas and U. Landman, *Phys. Rev. Lett.* 82, 5325 (1999).
124. B. Szafran, S. Bednarek, and J. Adamowski, *Phys. Rev. B* 67, 045311 (2003) [erratum 159902(E)].
125. S. M. Reimann and M. Manninen, *Rev. Mod. Phys.* 74, 1283 (2002).
126. S. M. Reimann, M. Koskinen, M. Manninen, and B. R. Mottelson, *Phys. Rev. Lett.* 83, 3270 (1999).
127. S. M. Reimann, M. Koskinen, and M. Manninen, *Phys. Rev. B* 62, 8108 (2000).
128. B. Szafran, S. Bednarek, and J. Adamowski, *J. Phys.: Condens. Matter* 15, 4189 (2003).
129. B. Szafran, S. Bednarek, J. Adamowski, M. B. Tavernier, E. Anisimovas, and F. M. Peeters, *Eur. Phys. J. D* 28, 373 (2004).
130. B. Szafran, F. M. Peeters, S. Bednarek, and J. Adamowski, *Phys. Rev. B* 69, 125344 (2004).
131. C. Yannouleas and U. Landman, *Phys. Rev. B* 66, 115315 (2002).
132. J. Kainz, S. A. Mikhailov, A. Wensauer, and U. Rőssler, *Phys. Rev. B* 65, 115305 (2002).
133. E. S. R. Yang and A. H. MacDonald, *Phys. Rev. B* 66, 041304 (2002).
134. E. E. Vdovin, A. Levin, A. Patane, L. Eaves, P. C. Main, N. Y. Khanin, Y. V. Dubovskii, and G. Hill, *Science* 290, 122 (2000).
135. B. Szafran and F. M. Peeters, *Europhys. Lett.* 66, 701 (2004).
136. M. Pi, A. Emperador, M. Barranco, F. Garcias, K. Muraki, S. Tarucha, and D. G. Austing, *Phys. Rev. Lett.* 87, 066801 (2001).
137. S. Bednarek, B. Szafran, T. Chwiej, and J. Adamowski, *Phys. Rev. B* 68, 045328 (2003).
138. M. T. Bjőrk, B. J. Ohlsson, T. Sass, A. I. Persson, C. Thelander, M. H. Magnusson, K. Deppert, and L. Samuelson, *Appl. Phys. Lett.* 80, 158 (2002).
139. F. C. Zhang and S. Das Sarma, *Phys. Rev. B* 33, 2903 (1986).
140. C. Fuchs and R. von Baltz, *Phys. Rev. B* 63, 085318 (2001).
141. P. D. Siverns, S. Malik, G. McPherson, D. Childs, C. Roberts, R. Murray, B. A. Joyce, and H. Davock, *Phys. Rev. B* 58, R10127 (1998).
142. A. Orlandi, M. Rontani, G. Goldoni, F. Mahghi, and E. Molinari, *Phys. Rev. B* 63, 045310 (2001).
143. L. E. Brus, *J. Chem. Phys.* 80, 4403 (1984).
144. G. Goldoni, F. Rossi, and E. Molinari, *Phys. Rev. Lett.* 80, 4995 (1998).
145. T. A. Fulton and G. J. Dolan, *Phys. Rev. Lett.* 59, 109 (1987).
146. K. Matsumoto, Y. Gotoh, T. Maeda, J. A. Dagata, and J. S. Harris, *Appl. Phys. Lett.* 76, 239 (2000).
147. Y. A. Pashkin, Y. Nakamura, and J. S. Tsai, *Appl. Phys. Lett.* 76, 2256 (2000).
148. Z. A. K. Durrani, A. C. Irvine, H. Ahmed, and K. Nakazato, *Appl. Phys. Lett.* 74, 1293 (1999).
149. T. Fujisawa, T. Hayashi, Y. Hirayama, H. D. Cheong, and Y. H. Jeong, *Appl. Phys. Lett.* 84, 2343 (2004).
150. M. A. Nielsen and I. L. Chuang, "Quantum Computation and Quantum Information." Cambridge University Press, Cambridge, UK, 2000.
151. D. P. DiVincenzo, "Semiconductor Spintronics and Quantum Computation" (D. D. Awschalom, D. Loss, and N. Samarth, Eds.), p. 221. Springer, Berlin, 2002.
152. A. Barenco, *Contemp. Phys.* 37, 375 (1996).
153. R. D. Woods and D. S. Saxon, *Phys. Rev.* 95, 577 (1954).